

Analysis of resting-state neurovascular coupling and
locomotion-associated neural dynamics using wide-field optical
mapping

Ying Ma

Submitted in partial fulfillment of the
requirements for the degree of
Doctor of Philosophy
in the Graduate School of Arts and Sciences

COLUMBIA UNIVERSITY

2018

©2018

Ying Ma

All rights reserved

ABSTRACT

Analysis of resting-state neurovascular coupling and locomotion-associated neural dynamics

using wide-field optical mapping

Ying Ma

Understanding the relationship between neural activity and cortical hemodynamics, or neurovascular coupling is the foundation to interpret neuroimaging signals such as functional magnetic resonance imaging (fMRI) which measure local changes in hemodynamics as a proxy for underlying neural activity. Even though the stereotypical stimulus-evoked hemodynamic response pattern with increased concentration of oxy- and total-hemoglobin and decrease in concentration of deoxy-hemoglobin has been well-recognized, the linearity of neurovascular coupling and its variances depending on brain state and tasks haven't been thoroughly evaluated.

To directly assess the cortical neurovascular coupling, simultaneous recordings of neural and hemodynamic activity were imaged by wide-field optical mapping (WFOM) over the bilateral dorsal surface of the mouse brain through a bilateral thinned-skull cranial window. Neural imaging is achieved through wide-field fluorescence imaging in animals expressing genetically encoded calcium sensor (Thy1-GCaMP). Hemodynamics are recorded via simultaneous imaging of multi-spectral reflectance. Significant hemodynamic crosstalk was found in the detected fluorescence signal and the physical model of the contamination, methods of correction as well as electrophysiological verification are presented.

A linear model between neural and hemodynamic signals was used to fit spatiotemporal hemodynamics can be predicted by convolving local fluorescence changes with hemodynamic

response functions derived through both deconvolution and gamma-variate fitting. Beyond confirming that the resting-state hemodynamics in the awake and anesthetized brain are coupled to underlying neural activity, the patterns of bilaterally symmetric spontaneous neural activity observed by WFOM emulate the functionally connected networks detected by fMRI. This result provides reassurance that resting-state functional connectivity has neural origins. With the access to cortical neural activity at mesoscopic level, we further explore the cortical neural representations preceding and during spontaneous locomotion.

Table of Contents

List of Figures	vi
List of Tables	ix
Acknowledgements	x
Chapter 1 Introduction	1
1.1 Functional connectivity derived from resting-state fMRI.....	3
1.1.1 Resting-state fMRI.....	3
1.1.2 Correlation-based functional connectivity	5
1.1.3 Default mode network and functionally connected networks.....	6
1.2 The neural basis of functional connectivity	8
1.2.1 Functional connectivity vs. anatomical connectivity	8
1.2.2 Influence of brain state.....	10
1.3 Neurovascular coupling and functional connectivity	12
1.3.1 Resting-state neurovascular coupling evaluated by fMRI and electrophysiology..	13
1.3.2 Resting-state neurovascular coupling evaluated by optical imaging and electrophysiology.....	15
1.4 Challenges of studying resting-state neurovascular coupling	17
Chapter 2 In vivo Methods for Observing Brain Functions	19

2.1	Electrophysiology.....	19
2.1.1.	Intracellular recordings	21
2.1.2	Extracellular recordings	22
2.1.3	Electroencephalography (EEG) and Electrocorticography (ECoG)	24
2.2	Non-invasive neuroimaging techniques	24
2.2.1	Radioactive neuroimaging	25
2.2.2	Magnetic resonance imaging	26
2.2.3	Functional MRI.....	28
2.2.4	Magnetoencephalography	30
2.3	Optical Imaging.....	30
2.3.1	Two-photon Microscopy.....	31
2.3.2	Laser Speckle Contrast Imaging	34
2.4	Summary	36
Chapter 3 Wide-field optical mapping (WFOM) of cerebral neural and hemodynamic activity		37
3.1	Introduction	37
3.2	Methods and Materials	38
3.2.1	Genetically-encoded calcium indicators (GECIs)	38
3.2.2	Animal preparation	40
3.2.3	Imaging Instrumentation.....	44

3.3	Quantification of hemodynamic changes from reflectance WFOM	46
3.4	Wide-field optical mapping of fluorescence contrast	50
3.4.1	The origin of hemodynamic contamination of wide-field fluorescence data	51
3.4.2	Methods of correcting for hemodynamic cross-talk in fluorescence WFOM	54
3.5	Verification of fluorescence WFOM with electrophysiology	59
Chapter 4	Assessing neurovascular coupling at resting state	62
4.1	Introduction	62
4.2	Materials and Methods	64
4.2.1	Animal preparation	64
4.2.2	Electrophysiology acquisition and analysis	65
4.2.3	Optical hemodynamic and GCaMP fluorescence imaging	66
4.2.4	Imaging data pre-conditioning and statistics	68
4.2.5	GCaMP fluorescence correction for hemodynamic cross-talk	68
4.2.6	Optimizing gamma-variate functions in fits of GCaMP response and HRF	69
4.2.7	Estimating HRF by least-square deconvolution	70
4.2.8	Spike-triggered averaging	71
4.2.9	Frequency-dependent cross-correlation analysis	72
4.2.10	Statistical analysis	72
4.3	Bilaterally symmetric patterns observed in resting-state neural and hemodynamic activity	

4.4	Analysis of spatiotemporal neurovascular coupling in awake animal	75
4.4.1	Model-based analysis of awake, resting-state data	77
4.4.2	Frequency-dependence of neurovascular correlations	80
4.5	Model-based analysis of anesthetized resting-state data.....	82
4.5.1	Spatial properties of <0.04 Hz slow trends	84
4.5.2	Slow trends in awake v/s anesthetized animals	85
4.6	Comparison of resting-state coupling in awake and anesthetized states.....	87
4.7	Discussion	90
4.7.1	Comparison to prior studies of resting-state neurovascular coupling.....	90
4.7.2	What do observed patterns of spontaneous neural activity represent?	92
4.7.3	Effects of anesthesia and slow hemodynamic trends.....	95
4.7.4	Implications for resting-state fMRI	96
4.8	Supplemental Figures	98
Chapter 5	Locomotion-associated neural dynamics	111
5.1	Introduction	112
5.2	Materials and Methods	113
5.3	Neural pattern revealed by running-triggered average.....	115
5.4	Regression analysis	119
5.4.1	Dimensionality reduction with K-means	119

5.4.2	Prediction of ongoing running	121
5.4.3	Prediction of future behavior	124
5.5	Discussion	128
Chapter 6 Discussion and Future Work		133
6.1	Identifying the cortical functional networks	133
6.2	Neural activity as a wave	136
6.3	State-dependent pattern	139
6.4	Frequency dependence of functional connectivity	141
References		144
Appendix: Publications and presentations related to this thesis		153

List of Figures

Figure 1. 1 The flowchart of calculating correlation-based functional connectivity from fMRI signal.	6
Figure 1. 2 Demonstration of resting-state functional connectivity.	7
Figure 1. 3 Comparison of functional connectivity and anatomical connectivity in mouse cerebral cortex.....	10
Figure 1. 4 The influence of brain state on neural activity pattern and functional connectivity in rat.	11
Figure 1. 5 Study of neurovascular coupling using fMRI and electrophysiology.	14
Figure 1. 6 Comparison of spontaneous and stimulus-induced neural and hemodynamic response.	16
Figure 2. 1 Schematic diagram of intracellular and extracellular recordings.	20
Figure 2. 2 Illustration of extracellular recordings in electrophysiology.....	23
Figure 2. 3 Schematic illustration of positron emission tomography.	25
Figure 2. 4 fMRI scanning and standard analysis for functional mapping.	29
Figure 2. 5 Illumination profile of one-photon and two-photon excitation.	32
Figure 2. 6 Demonstration of two-photon microscopy using for chronic awake mouse imaging.	33
Figure 2. 7 Studies cortical blood flow in rat's barrel cortex using laser speckle contrast imaging.	35

Figure 3. 1 Expression patterns of Thy1-GCaMP3 transgenic mice.	39
Figure 3. 2 Instrumentation for WFOM and examples of raw diffuse reflectance data.	45
Figure 3. 3 Schematic of light paths in WFOM travelling to and from a GCaMP fluorescence interaction.	51
Figure 3. 4 Hemodynamic correction of WFOM GCaMP data.....	57
Figure 3. 5 Validating wide-field GCaMP fluorescence with electrophysiology in presence and absence of stimulation.....	61
Figure 4. 1 Wide-field imaging of GCaMP fluorescence and hemodynamic activity in the awake mouse brain.....	74
Figure 4. 2 Spatiotemporal modeling of hemodynamics from wide-field Thy1-GCaMP6f recordings in the awake, resting brain.	80
Figure 4. 3 Frequency-dependence of neurovascular correlations.	81
Figure 4. 4 Spatiotemporal modeling of hemodynamics from wide-field GCaMP recordings in the resting-state urethane anesthetized brain.	83
Figure 4. 5 Analysis of urethane-anesthetized animals and the presence of slow hemodynamic trends.....	87
Figure 4. 6 Summary of HRFs derived from multiple analysis methods.	89
Figure 4. 7 Electrophysiology comparison in Thy1-GCaMP3 and Thy1-GCaMP6f mice.	98
Figure 4. 8 Control experiment comparing WFOM measurements in Thy1-YFP and Thy1-GCaMP3 mice.....	99

Figure 4. 9 Mean average and standard deviation Pearson's correlation for gamma-variate fitting in awake animals.	100
Figure 4. 10 Examples of model-based fitting of neural activity to resting state hemodynamics in awake Thy1-GCaMP6f mice: Same region, different trials.	101
Figure 4. 11 Examples of model-based fitting of neural activity to resting state hemodynamics in awake Thy1-GCaMP6f mice: Same trial, different regions, two imaging sessions.	102
Figure 4. 12 The correspondence between neural activity and hemodynamics at <0.4 Hz in awake mouse brain.	103
Figure 4. 13 Examples of model-based fitting of neural activity to resting state hemodynamics in urethane-anesthetized Thy1-GCaMP3 mice: Same region, different trials.	104
Figure 4. 14 Comparison of model-based fitting of neural activity to resting state hemodynamics during different neural states in a urethane-anesthetized Thy1-GCaMP3 mouse.	105
Figure 4. 15 Demonstration of the spatial representation of slow hemodynamic trends in multiple urethane anesthetized Thy1-GCaMP3 mice.	107
Figure 4. 16 Results of awake resting-state neurovascular coupling analysis including high-pass filtering at 0.04Hz to reduce slow trends.	110
Figure 5. 1 Spatial neural pattern during locomotion.	116
Figure 5. 2 Time courses of neural activity in S1, V1, M1 and S2 before and during locomotion.	117
Figure 5. 3 Longitudinal functional maps derived by k-means clustering with $k = 10$	120
Figure 5. 4 Linear regression model for ongoing behavior prediction.	122

Figure 5. 5 General Linear regression results and weights.	123
Figure 5. 6 Linear regression model setup for moving preparation.	125
Figure 5. 7 Spatiotemporal pattern of regional neural activity leading towards spontaneous locomotion.	127
Figure 6. 1 Phase-aligned spectral filtering (PASf) detected waves in GCaMP fluorescence activity acquired under Ketamine anesthesia.	137
Figure 6. 2 PASf applied to (a) neural and (b) hemodynamic data acquired from an awake animal.	138
Figure 6. 3 State-dependent neural activity and neurovascular coupling in urethane-anesthetized Thy1-GCaMP3 mice.	140
Figure 6. 4 Neural correlation analysis at different frequency band.	142

List of Tables

Table 1. Spatiotemporal resolution of the most commonly used neuroimaging modalities.	36
--	----

Acknowledgements

I would like to express my gratitude to everyone who has been providing support and guidance throughout my PhD. Special thanks to my thesis advisor, Dr. Elizabeth Hillman for giving me the opportunity of coming to Columbia University in the first place and patiently guiding and teaching me over the years. I'm constantly inspired by her genuine passion towards searching for the concealed truth and she sets an impeccable example of a scientist, engineer and mentor.

I would like to thank the members of my thesis committee, Dr. Paul Sajda, Dr. Joshua Jacobs, Dr. Tian Zheng and Dr. Rui Costa for providing valuable insights and advice towards my work. I sincerely appreciate their time and effort. Special thanks to Dr. Tian Zheng, who has provided guidance especially towards the end of my PhD and brought me a new perspective of my work and future.

I would like to thank all my colleagues and friends in the Laboratory of Functional Optical Imaging, who have made this journey much more enjoyable than I expected. I particularly would like to thank Sharon Kim, Mohammed Shaik, Teresa Zhao, Venkatakaushik Voleti and Wenzhe Li, who have navigated through this journey with me. I have learned tremendously from them and I will always cherish and be grateful of sharing this part of my life with them.

Finally, I would like to thank my family for their understanding and unconditional support of every decision I've made.

Chapter 1

Introduction

Clinical neuroimaging modalities such as fMRI monitor blood fluctuations in the brain to indirectly infer the underlying patterns of brain's activity. This inference is based on the assumption of a linear relationship between neural and hemodynamic activity, which has not been directly proven yet. To address this problem, our lab established an imaging modality that achieves simultaneous recording of both neural and hemodynamic signal across the entire dorsal surface of the mouse brain. Enabled by this technology, we are able to visualize the spatiotemporal dynamics over the bilateral cortex in awake and behaving animals. This thesis documents the progression of this study and is organized as follows:

Chapter 1 provides an introduction of the background and explains the motivation of studying resting-state neurovascular coupling in relation to the functional connectivity derived by fMRI, followed by a discussion of previous studies addressing this problem with various approaches, and finally a summary of the challenges of studying resting-state neurovascular coupling.

Chapter 2 reviews a series of techniques that have been used to study brain activity in vivo. Electrophysiological approaches, the gold standard of measuring neural activity, are introduced at the beginning followed by non-invasive neuroimaging techniques that have been commonly used

in clinical settings, and optical imaging methods that are popular in scientific studies. The characteristics of these neural monitoring methods are summarized and compared in terms of spatial, temporal resolution and the invasiveness of the procedure.

Chapter 3 introduces the hardware, experimental setup and pre-processing steps of wide-field optical mapping (WFOM) technology used for simultaneous recording of both neural and hemodynamic changes. Considerations for implementation, necessity and procedure for hemodynamic contamination correction and electrophysiological confirmation are included.

Chapter 4 presents a quantitative assessment of resting state neurovascular coupling in both awake and anesthetized mice. By mathematically deriving the hemodynamic response function, the spontaneous fluctuations in blood can be reliably predicted by local neural activity. In addition to quantitative evaluation of neurovascular coupling across the bilateral cortex, the rapidly evolving, symmetrical spontaneous neural activity patterns which resemble the functionally connected networks found in fMRI are observed and described.

Chapter 5 explores the neural activation pattern during and before spontaneous locomotion. Results from a descriptive approach, known as the running-triggered average were presented. In order to pinpoint the spatiotemporal dynamics of neural activation during and before locomotion, an analysis pipeline consisting of motion detection, dimensionality reduction and multi-variable linear regression is established.

In the final chapter, several directions of approaching and extracting the rich information within the spontaneous neural activation patterns are proposed and discussed. Results from some preliminary attempts are presented.

1.1 Functional connectivity derived from resting-state fMRI

Non-invasive neuroimaging technologies commonly utilize cortical blood flow as a proxy for underlying local neural activity. In the absence of stimuli, the blood oxygen level dependent (BOLD) signals measured by fMRI was found to be correlated to the signal measured from distant brain regions, suggesting that these regions may share or serve as similar functions. Various functionally connected networks have been found using this method, including the default mode network (Raichle et al., 2001; Fox and Raichle, 2007), sensorimotor network (Biswal et al., 1995), visual network (Beckmann et al., 2005; De Luca et al., 2006) and language network (Tomasi and Volkow, 2012). These functionally connected networks have been confirmed not only in human but also in various animal models.

The inference of neural activity from neuroimaging is based on the assumption that local hemodynamic activity is a direct reflection of local neural activity. Former researchers presumed that increased neural activity in a brain region increases local blood flow (Raichle, 1998). However, this relationship known as ‘neurovascular coupling’ is far more complex and requires better understanding and quantification. Recent studies have explored the cortical neurovascular coupling with external stimuli and their results challenged the assumption of linearity between neural and hemodynamic activity (Hewson-Stoate et al., 2005; Logothetis, 2008). As such, the spatiotemporal linearity of neurovascular coupling at resting-state still requires evaluation.

1.1.1 Resting-state fMRI

The development of fMRI in 1991 facilitated a non-invasive way of mapping brain functionality in combination with behavioral tasks and external stimulation. Soon after that, Biswal and colleagues found a pronounced oscillatory pattern in BOLD signal that is independent of stimulus

(Biswal et al., 1995). The observation that spontaneous fluctuations in the motor cortex are correlated with fluctuations in other regions of the motor system for the first time provides experimental evidence of mapping functional connectivity with resting-state fMRI (rs-fMRI). Compared to stimulus-induced mapping targeting specific functional regions, resting-state functional connectivity mapping can assess multiple brain networks with one scan. In addition, rs-fMRI scan can be performed on unconscious patients or on subjects that are unable to perform cognitive tasks because of the absence of task requirement.

What is ‘resting-state’?

The term ‘resting-state’ is generally used to describe the baseline condition in the absence of a stimulus or a task requirement. In animal experiments, the subjects are usually sedated or lightly sedated to reduce the subject’s motion in MRI scanner. However, anesthesia will introduce inevitable confounds in the fMRI results. Numerous studies have shown that the anesthesia not only affects the physiological conditions, but also alters neural activity patterns and general brain state (Grandjean et al., 2014). Furthermore, the cerebral vasculature and neurovascular coupling are also subject to the alteration of physiological condition, which makes the functional connectivity even more difficult to interpret. Hence, the type of anesthesia and the depth of anesthesia needs to be taken into consideration when comparing rs-fMRI results among diverse conditions.

On the other side, the human subjects are usually awake and asked to remain still during the rs-fMRI scan. It’s also a common practice to ask the patient to perform some low-level tasks, such as fixation, which will not change the mapping for functional connectivity. However, during the resting-state recording, thoughts emerging during the trial and shifting of attention is unavoidable. In fact, the awake and conscious brain is remarkably active even during resting-state, and the

presence of the restless spontaneous fluctuations is the foundation of identifying functionally connected networks.

1.1.2 Correlation-based functional connectivity

Functional connectivity refers to the observation that correlations of spontaneous blood fluctuations occur between brain regions sharing similar function or anatomical connections. This correlation is usually quantified by seed-based correlation analysis. This method entails selecting a region of interest (ROI) and then computing the correlation coefficient of the average BOLD time course within the ROI with all the other voxels in the brain (as demonstrated in Figure 1. 1). The ROI and the voxels that are significantly correlated with it are marked as the same functionally connected network. This process can be repeated by selecting ROIs from various location to form a comprehensive view of all the networks.

There are several other methods that researchers typically use to map functionally connected networks. One popular approach is independent component analysis (ICA), which maximize its non-Gaussian components' statistical independence. The networks identified by ICA are significantly similar to the results of seed-based correlation analysis (Rosazza et al., 2012). However, as a blind-source separation algorithm, the output might be noisy and uninterpretable and requires manual selection of meaningful components.

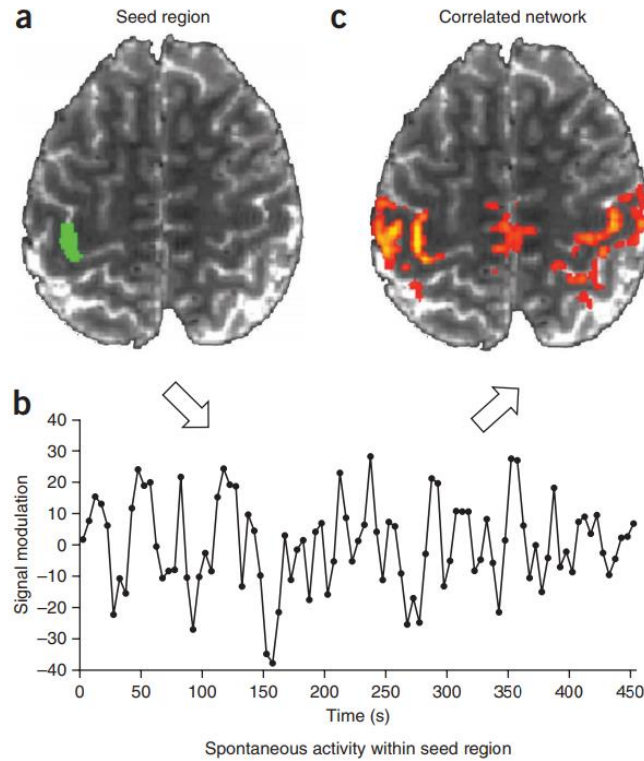


Figure 1. 1 The flowchart of calculating correlation-based functional connectivity from fMRI signal. (a) Choosing region of interest as seed (green) based on brain atlas. (b) The average time course of the spontaneous BOLD signal in the seed region over 7.5 min. (c) Brain areas of high correlation with the seed region were highlighted as functionally connected network. (Figure reproduced from Buckner et al. (2013))

1.1.3 Default mode network and functionally connected networks

A group led by Dr. Marcus Raichle at Washington University in St. Louis was one of the first to study regional correlations of hemodynamic fluctuations in resting state with PET (Raichle et al., 2001) and fMRI (Raichle et al., 2001; Fox et al., 2005). In their early studies, they found that certain brain regions displayed increases in activity during attention-demanding cognitive tasks, whereas some other regions had decreased in activity (Simpson et al., 2001). These regions were then further investigated with fMRI during resting-state. The analysis on the spontaneous BOLD signal revealed correlations within each network as well as anti-correlations between networks

(Figure 1. 2)(Fox et al., 2005). Because the task-negative network has a negative response to the tasks and attention and displays dominating activation during resting state, it was thereafter named default mode network (DMN).

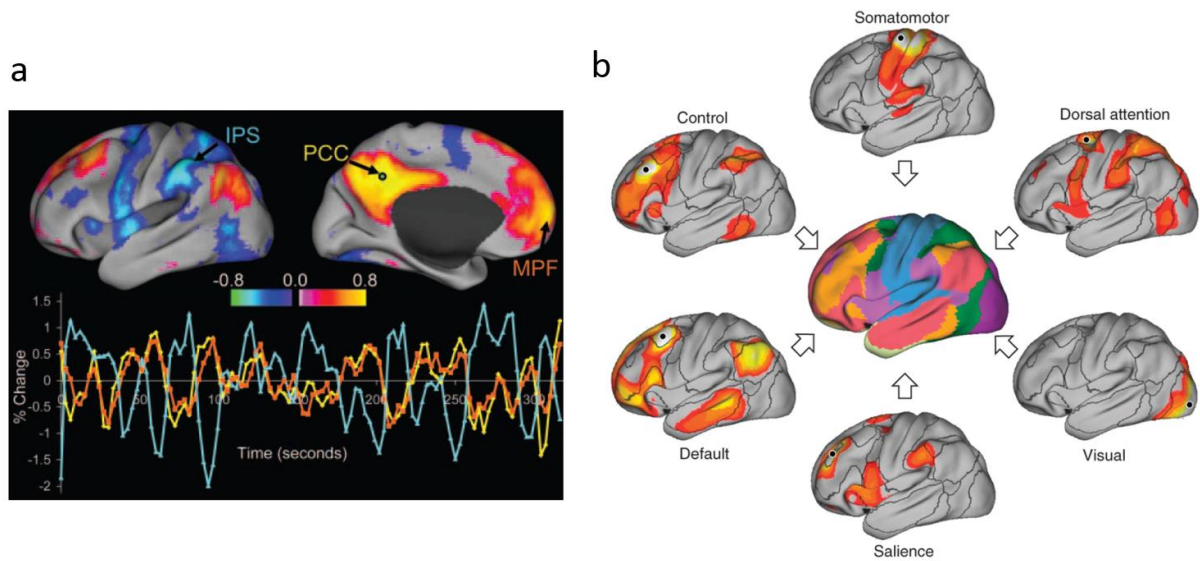


Figure 1. 2 Demonstration of resting-state functional connectivity. Intrinsically correlated and anticorrelated networks with a seed region in Posterior cingulate/precuneus (PCC), which was identified as part of the default mode network (Fox et al., 2005). (b) Studies using functional connectivity have consistently revealed that the human brain possesses several large-scale distributed networks (Figure adapted from Buckner et al., 2013).

Since then, a number of functionally connected networks have been identified in addition to the default mode network (Raichle et al., 2001; Fox et al., 2005), such as the sensorimotor network (Biswal et al., 1995), visual network (Beckmann et al., 2005; De Luca et al., 2006), and language network (Tomasi and Volkow, 2012) (Figure 1. 2b). Studies of default mode networks were extended to various animal models as well (Vincent et al., 2007; White et al., 2011; Kyathanahally et al., 2014). With the growing interest in functional connectivity research, the fundamental

question of how blood flow fluctuations are associated with the underlying neural network is drawing considerably more attention.

1.2 The neural basis of functional connectivity

As introduced previously, one of the major application of functional connectivity is the identification of brain regions according to functionality. In the process of interpreting functionally connected networks and its implication on various neurological disorders, it is essential to understand the neural origin of the spontaneous fluctuation detected by fMRI. Specifically, one of the major questions is what drives the synchronization of activity in the regions that are not physically adjacent. Another aspect of the influence of neural network on functional connectivity is the global synchronization of activity at some brain state. The shifting of brain state alters the appearance of region-wise correlation and complicates the interpretation of functional connectivity.

1.2.1 Functional connectivity vs. anatomical connectivity

Comparisons between functional connectivity and anatomical connectivity has been made by several groups in the mouse cortex (Figure 1. 3). The anatomical map was reconstructed from the Allen Brain Institute mouse brain connectivity atlas, of which the physical projection was visualized by viral tracing. As demonstrated in Figure 1. 3, the general location of the networks (such as the anterior to posterior arrangement of motor network, somatosensory network and visual network) is congruent between the two connectivity maps. Another prominent feature shared by both functional and anatomical networks is the bilateral symmetry. As the most consistent feature of functional connectivity, the physical foundation of this phenomenon is still undetermined. One

possible explanation for spontaneous fluctuations across hemispheres is the transcallosal projection which conveys information via interhemispheric inhibition. A recent study of vasomotion in mouse cortex abolished the transhemispheric correlations of arteriole diameter in acallosal mice (Mateo et al., 2017). Contradicting results were found in some cases of developmental callosal agenesis where the synchronization between bilateral regions were preserved (Tyszka et al., 2011). Common subcortical inputs, projections from thalamus for example, may also contribute to the homotopic synchrony in the absence of the corpus callosum. Characterizing the direct and indirect physical pathways leading to bilateral synchrony in the brain is not only beneficial for interpreting the functional connectivity in terms of neural basis, but it also promotes the examination of the purpose and necessity of the spontaneous and symmetrical activation in the resting brain.

Despite the agreement of general localization of the networks and the bilateral symmetry, the finer details of the functional regions diverges from the anatomical map. Specifically, in the process of performing correlation analysis, the boarder or the edge of the functional region is usually fuzzy and may overlap with other functional regions depending on the selection of the seed region. Therefore, functionally connected networks are not a direct reflection of anatomical projections or physical connections. Bridging the gap between functional and anatomical connectivity and characterizing the confound introduced in the process of neuroimaging is the dire need to interpret resting-state fMRI results.

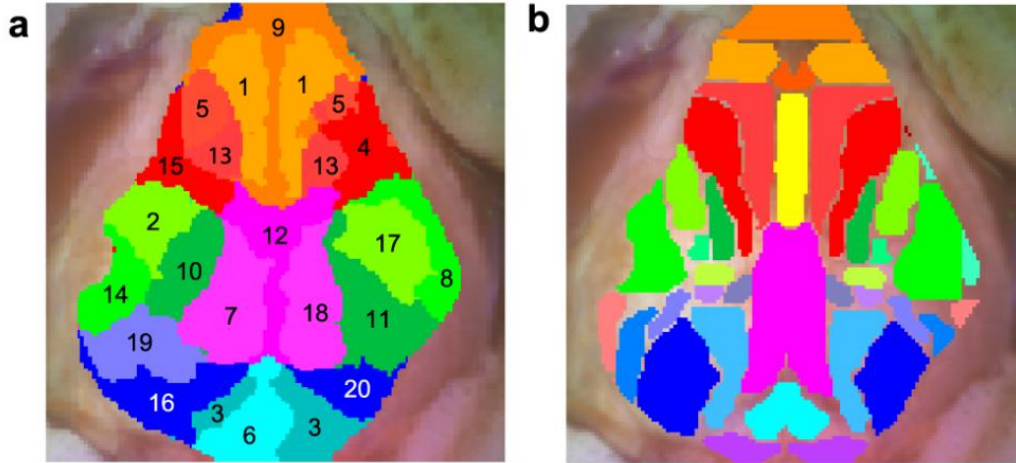


Figure 1.3 Comparison of functional connectivity and anatomical connectivity in mouse cerebral cortex. Cortex parcelation based on correlation from ketamine anesthetized resting-state mouse. The major networks demonstrated are frontal/olfactory network (orange), motor network (red), somatosensory network (green), visual network (blue), retroplenial region (magenta) and superior colliculus (cyan). (b) The anatomical atlas adapted from Allen Mouse Brain Atlas with the same color coded regime (figure adapted from White et al., 2011).

1.2.2 Influence of brain state

The functional connectivity indicates the regionally specified neural connections by examining the correlation at local regions. From a point of view of the entire system, the synchronization of the entire brain is equally vital to investigate because it indicates the current state of the brain. A recent study by Liu et al. demonstrated the influence of brain state on the functional connectivity by varying the concentration of anesthesia (Liu et al., 2013). As the depth of anesthesia increased, the brain transited into a globally synchronized burst-suppression state, or up-and-down state (Figure 1.4). This brain state is usually characterized by rhythmic alterations between synchronized brain-wide firing (up state) and cortical silence (down state). As illustrated with EEG recordings in Figure 1.4b, the up-and-down state was dominant in the deep anesthesia condition and the cortex-

wide occurrence of the neural activation overwhelmed the local specificity and synchronized the regions that are not functionally connected in the light anesthesia stage.

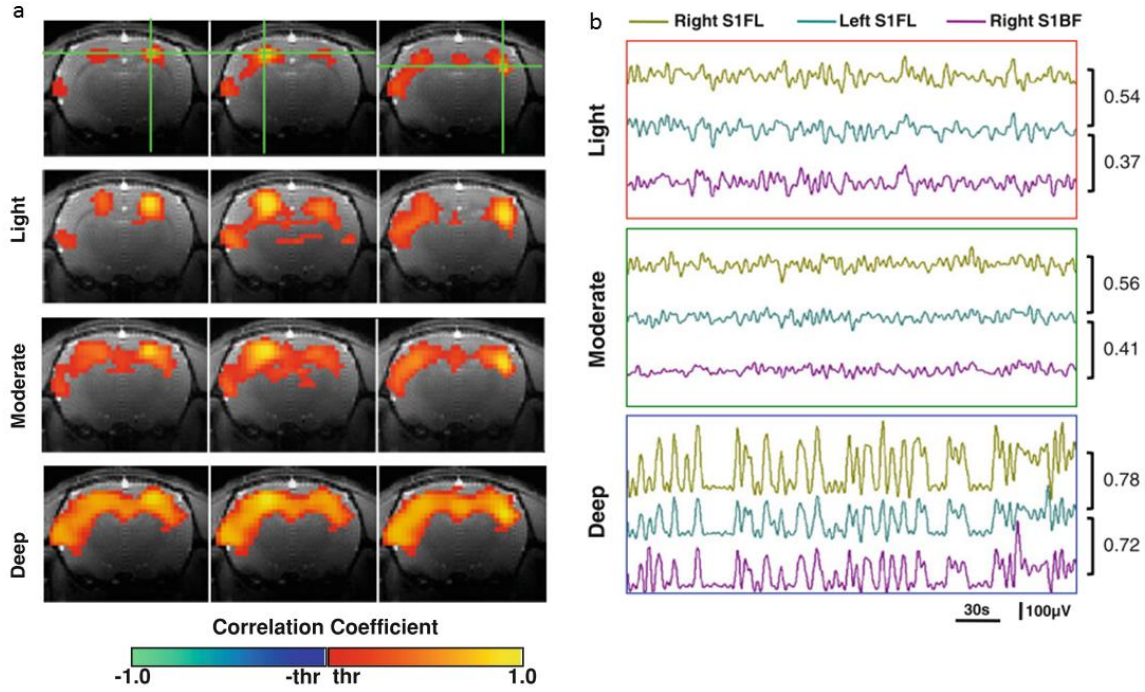


Figure 1. 4 The influence of brain state on neural activity pattern and functional connectivity in rat. (a) BOLD correlation maps from three seed regions under light (1% isoflurane), moderate (1.5% isoflurane) and deep anesthesia (1.8% isoflurane). (b) Spontaneous EEG signals from a separate experiment with the electrodes in the corresponding locaion in (a) (figure adapted from Liu et al., 2013).

The up-and-down state has been observed in various physiological conditions, including under anesthesia (such as isoflurane and ketamine), during rapid eye movements (REM) sleep and even in the awake and conscious brain (Brown et al., 2012; Liu et al., 2013; Pagliardini et al., 2013). Even though the up-and-down state has been discovered and described by electrophysiological studies, the profound influence of the brain state hasn't been characterized at a system level until resting-state fMRI studies. As shown in Figure 1. 4a, the cerebral cortex was widely coherent under

the up-and-down state and the boundary of locally connected network was extended far beyond the region found in the light anesthesia state. Further investigation also showed that the local correlation pattern can be recovered by removing the globally synchronized signal via global trend regression.

The discovery of this globally synchronized trend induced by up-and-down state alters the appearance of regional correlation and renders the interpretation of functional connectivity unreliable without knowledge of the current brain state. This study also demonstrated the complexity and necessity of the neural basis of functional connectivity because the up-and-down state is just one specific type of brain state and its appearance may vary in different animal models and at different or in transitory physiological states. To overcome this problem, a secondary measurement of underlying neural activity or a physiological marker for brain state should be taken in parallel with the resting-state fMRI.

1.3 Neurovascular coupling and functional connectivity

In early studies, the interpretation of functionally connected networks is built on the assumption that local hemodynamic activity is a linear representation of the local neural activity. However, this relationship, also referred to as ‘neurovascular coupling’, is far more complex and requires better understanding and quantification. Researchers have combined electrophysiological recordings with simultaneous measurements of cerebral blood dynamics to gain insights of this correspondence. In here, two representative studies on resting-state neurovascular coupling were reviewed and the challenges for this type of study is summarized at the end.

1.3.1 Resting-state neurovascular coupling evaluated by fMRI and electrophysiology

Even though fMRI is currently the most popular neuroimaging modality to study functional connectivity, it is not a direct measurement of neural activity. The fMRI BOLD signal is determined by local changes in deoxy-hemoglobin (HbR), but how the BOLD signal and neural activity are linked remains unknown. Neurovascular coupling induced by external stimuli has been studied (Hewson-Stoate et al., 2005; Logothetis, 2008) and the results regarding linearity are largely inconclusive. Therefore, fMRI researchers began to bridge this gap by combining resting-state BOLD fMRI with concurrent electrophysiological recordings.

Dr. Nikos K. Logothetis and his group have endeavored to investigate the correlation between BOLD signal and LFP and MUA for the past 10 years. Since LFP is a mass neural signal that combines a number of neural processes, Magri et al. separated LFP recordings in anesthetized monkeys into several bands according to their frequency (Magri et al., 2012). Information theory was then utilized to characterize the statistical dependency between BOLD and band-limited LFP power. Their results illustrated in Figure 1. 5 showed all three frequency bands (alpha: 8-12 Hz, beta: 18-30 Hz and gamma: 40-100 Hz), the total LFP power (8-100 Hz) and MUA significantly correlates with BOLD signal with a 3s delay. Among all the bands and MUA, the gamma power shared the largest amount of mutual information with BOLD signal.

This pilot work done by Magri et al. provided a great insight into how to study the neurovascular coupling with fMRI and electrophysiology, however their conclusions are not consistent with other literature. Some studies claim delta band (1-4 Hz) is the dominating band that governs fMRI response in α -chloralose-anesthetized rats (Fox and Raichle, 2007), while others claim that MUA is more closely related to BOLD signal than LFP in awake non-human primates (Lima et al., 2014). Moreover, even though significant correlations between BOLD and electrophysiological signals

have been claimed by many studies, the value of correlation coefficients remained low, typically around 0.3 (Shmuel and Leopold, 2008; Scholvinck et al., 2010; Magri et al., 2012). The limited correlation between neural and fMRI signal may attribute to several factors and needs to be confirmed with other modalities.

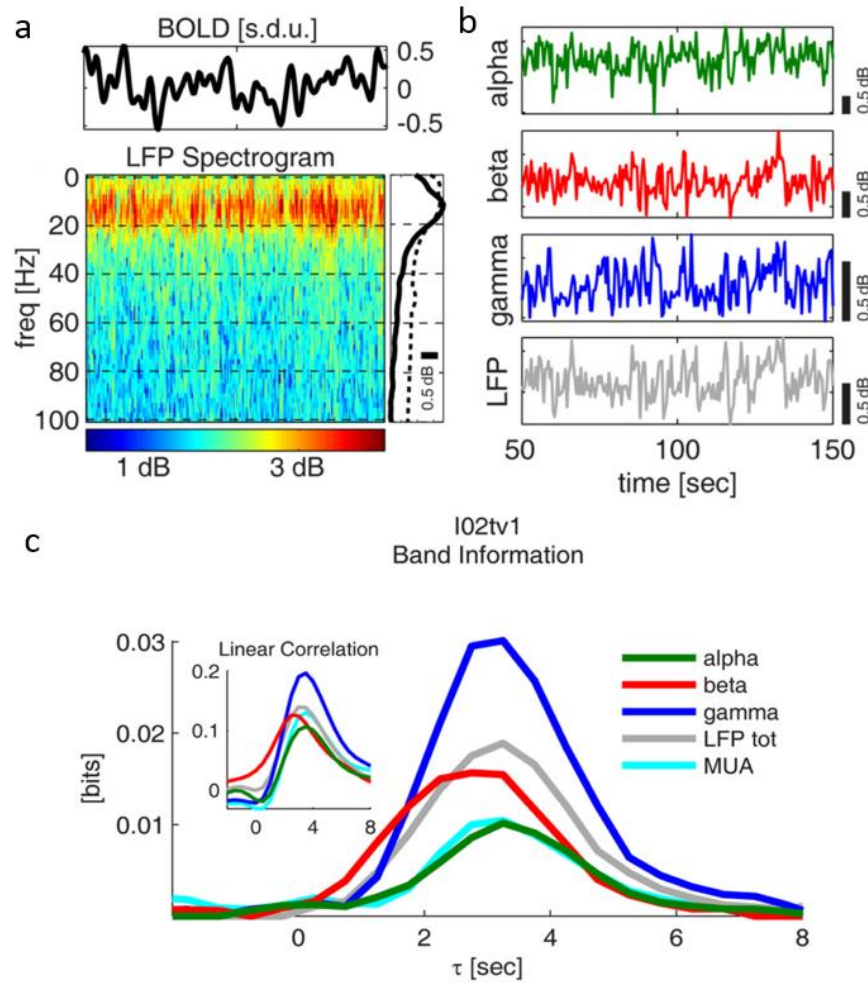


Figure 1. 5 Study of neurovascular coupling using fMRI and electrophysiology. (a) Illustration of BOLD signal time course, with spectrogram of the LFP recorded from the location of the BOLD signal above. (b) Time courses of spontaneous LFP power in the alpha, beta, and gamma band and total LFP power. (c) Mutual information between the BOLD signal and the LFP power or MUA. The inset shows the Pearson correlation between the BOLD signal and the power in the LFP bands or MUA (figure adapted from Magri et al., 2012).

1.3.2 Resting-state neurovascular coupling evaluated by optical imaging and electrophysiology

Besides fMRI, resting-state neurovascular coupling was studied by other neuroimaging modalities as well. A study by Bruyns-Haylett et al. attempted to access neurovascular coupling at resting-state by using optical intrinsic imaging (Bruyns-Haylett et al., 2013). Specifically, concurrent neural and hemodynamic activity was recorded in the urethane-anesthetized rat in the absence of stimuli. The hemodynamic activity was recorded with two-dimensional optical imaging spectroscopy (2D-OIS). Under the light of different wavelengths generated by a high speed filter wheel, a camera recorded images of the somatosensory cortex through the thinned skull. Spectral analysis was then applied to the data to generate maps for changes in cortical total hemoglobin (HbT) and oxy-hemoglobin (HbO) and deoxy-hemoglobin (HbT). The time courses of hemodynamic activity were smoothed and low-pass filtered below 0.25 Hz. Local field potentials (LFPs) were chosen as a metric of neural activity. Multi-laminar recordings of LFPs were made with a 16-channel electrode probe with 100 μ m inter-site distance. The LFPs were subjected to current source density (CSD) analysis to disambiguate LFP data into spatially distinct current sinks and sources. CSD analysis essentially takes the second spatial derivative of the LFP. A current above zero reflects sources while current below zero represents sinks. Since current sinks indicate neural activation, the channel with the biggest current sink amplitude (\sim 500 μ m below the surface of the brain) was chosen to use in the neurovascular coupling analysis.

To quantitatively associate the hemodynamic activity with the resting-state CSD-analyzed LFP signal, the authors employed the event-trigger average technique. The neural data were separated into consecutive 6s bins across each trial and the largest negative deflection above a threshold of 2 standard deviations from the mean was selected to be a neural event. The 6s time period for the

bin was selected to allow the resting-state hemodynamic fluctuations to peak. After a neural event was identified, a single epoch of the accompanying hemodynamic fluctuations was taken from 3s before each neural event to 16s after each neural event. The epochs were then averaged for each hemodynamic component per animal and then across all of the animals in the cohort. The average for the hemodynamics was then normalized to the maximum overall mean HbT magnitude, such that the HbT maximum was unity and the relative magnitudes of HbO and HbR changes were preserved.

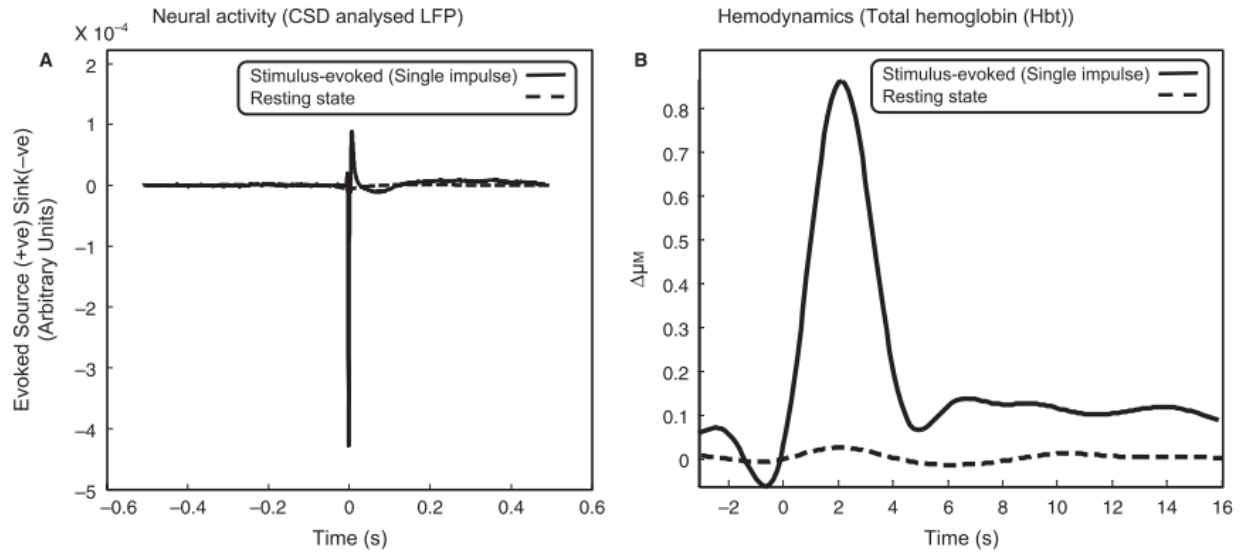


Figure 1. 6 Comparison of spontaneous and stimulus-induced neural and hemodynamic response. (a) Time series of current source density analysed LFP in average. (b) Time series of HbT averaged across animals (figure adapted from Bruyns-Haylett et al. 2013).

The averaged epochs of hemodynamic fluctuations after neural events showed an increase in HbT and HbO concentrations and a decrease in HbR concentration similar to the hemodynamic responses induced by stimulation (Figure 1. 6), while the randomly selected epochs did not follow this trend. Similar trends of increase in HbT and HbO and decrease in HbR were shown by the averaging hemodynamic epochs identified from all the frequency bands, and controls

consistently showed random trends of hemodynamic changes. In comparing multi-laminar CSD-analyzed LFPs and temporal dynamics of HbT changes elicited by spontaneous neural events and single electrical stimuli, the authors found that the magnitudes of both neural events and accompanying hemodynamics derived from resting-state data are around 40 times smaller than those evoked by single electrical whisker pad stimulation.

This study was one of the first to quantitatively access the resting-state neurovascular coupling with neuroimaging techniques other than fMRI and attempted to compare that with stimulus-driven results. However, the conclusion about the amplitude of spontaneous hemodynamic response was an underestimation of the scale of spontaneous fluctuation. This result can be attributed to oversampling of neural events: even though the lump average reveals the general trends of spontaneous hemodynamic response, the actual scale was diminished in the process of averaging highly variable events.

1.4 Challenges of studying resting-state neurovascular coupling

From the review of previous neurovascular studies, it is apparent that experiments and analysis have a lot of limitations. One particular challenge in studying dynamic changes in the brain is accessing the global neural activity. Due to the spatial limitation of electrophysiological recordings, neurovascular coupling was evaluated only within a small region. Direct evidence of the connection between neural and hemodynamic signal is needed to infer the spatiotemporal characters of functional connectivity derived from fMRI.

To evaluate cortical neurovascular coupling, it is essential to record concurrent changes in neurons and blood. Even though measuring the electrical property of the neurons is the gold standard, it is

challenging to record it at the same time as fMRI scanning due to the artifacts induced by changing the magnetic field.

Analyzing simultaneous neural and hemodynamic signals acquired at resting state is another problem we need to address. A numerical approach to evaluating the degree of coupling is necessary for comparison between regions and states. Additionally, unlike stimulus-driven responses, the spontaneous fluctuations cannot be quantified by repeated measurements and averaging. Thus, methods to statistically summarize the results need to be developed.

Chapter 2

In vivo Methods for Observing Brain Functions

Reliable recording of brain activity is essential to for the study of brain function. Over the past century, various techniques have been developed to improve the recording capabilities and increase the access to the brain. Based on the inherent electrical property of the neurological system, the most direct way of monitoring brain activity is through electrophysiological recordings. However, the invasiveness of the electrode limits the clinical application of this method. To overcome this constraint, non-invasive neuroimaging techniques, such as positron emission tomography (PET) and functional magnetic resonance imaging (fMRI) have been widely applied to neuroscience research. Most recently, multi-modal optical imaging techniques have become more prevalent since they provide high spatial and temporal resolution. In this chapter, several techniques for monitoring brain's function will be reviewed and their respective merits and limitations will be discussed.

2.1 Electrophysiology

Nerve cells, or neurons, are the main component of the central nervous system. They are morphologically and functionally specialized for the generation and propagation of electrical events. Neurons communicate within the central and peripheral nervous system as well as with

other end organs via electrical signals. Therefore, as a direct measurement of neurons' electrical properties, electrophysiology has been able and will continue to provide first-hand information of the 'language' of neurons.

Classical electrophysiology requires insertion of conductive electrodes made of metal, glass or silicon inserted into biological tissues, and the impedance, or the contact area, of the electrode determines the spatial resolving power of this technique. As the contact area increases, the impedance of the electrode decreases and as a result, the electrode integrates electrical activity from a wider space, thus reducing the electrode's resolving power. If the electrode is small enough to be inserted into a single cell, the membrane potential of the neuron can be recorded intracellularly. If the recording electrode is placed outside a cell, the extracellular electrical activity, including unit-activity and local field potential, can be detected.

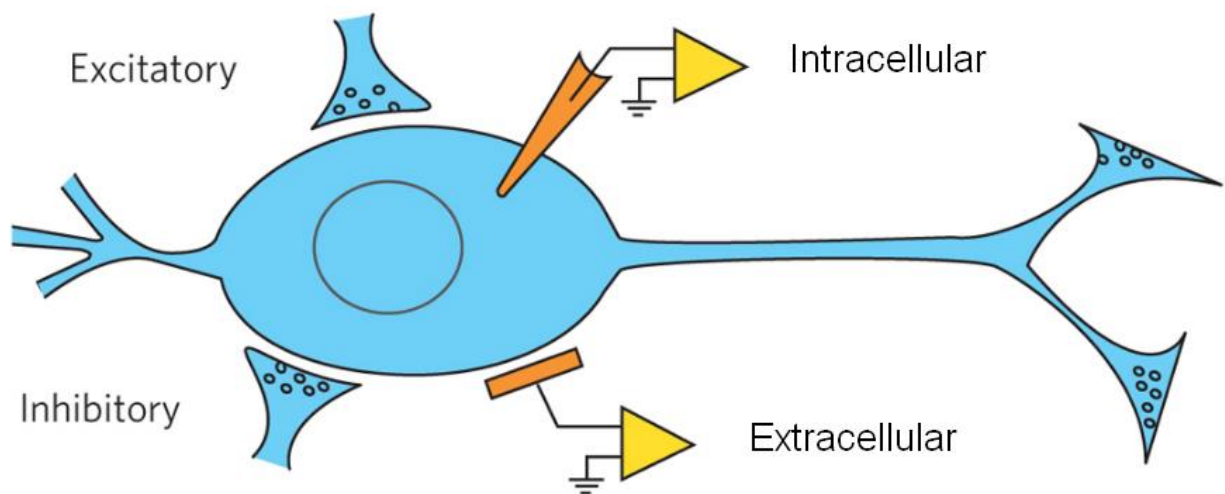


Figure 2. 1 Schematic diagram of intracellular and extracellular recordings. The neuronal firing patterns of individual neurons modulated by excitatory and inhibitory synaptic inputs can be detected by intracellular and extracellular recordings. The electrodes are marked in orange and the amplifiers in yellow. Figure adapted from Spira and Hai (2013).

Electrodes with an even larger contact surface, such as surface electrodes, can be placed directly on the intact brain or even on the scalp to detect the net activity from an ensemble of neurons. Even though the spatial resolution of electrophysiology is limited by electrodes, the information provided by millisecond-range temporal resolution is still valuable and irreplaceable in both research and clinical settings.

2.1.1. Intracellular recordings

Intracellular recording in the field of neuroscience usually involves measuring the transmembrane voltage or current in a living neuron. The concept of the measurement is simple: one electrode is inserted into the intracellular space without breaking the seal between the electrode and membrane, and the other electrode is placed outside the cell as reference. The transmembrane voltage difference or current flow is amplified and continuously recorded. While the concept of intracellular recording is straightforward, the instrumentation requirement for recording is the most technologically challenging among electrophysiology techniques. Glass micropipettes filled with a conductive electrolyte solution are the most commonly used electrodes for intracellular recordings. The diameter of the electrode's tip is typically under 500 nanometers, and the DC resistance is on the order of 100 Mega ohms.

Intracellular recording is as an essential method for studying electrical properties on the single cell level. In 1952, Alan Lloyd Hodgkin and Andrew Fielding Huxley utilized intracellular recording and voltage clamp to describe how action potentials in neurons are generated and propagated in the giant neuron of squid. The voltage clamp, an advanced version of intracellular recording, requires another electrode that injects ionic current into the cell while the membrane potential is maintained at a determined level monitored by the intracellular electrode. Other advanced

intracellular recording techniques, such as current clamp, and patch clamp have also enabled studies of cell signaling since their development in 1970.

2.1.2 Extracellular recordings

Unlike intracellular recordings, extracellular recordings require placement of both electrodes in the extracellular space (Figure 2. 2a). To record single-unit activity, the recording electrode must be positioned immediately adjacent to a neuron. The impedance of the electrode governs the size of the reception field, and the higher the impedance, the smaller the reception field. In the case of single-unit recording, the impedance of the electrode is above $1\text{M}\Omega$ to ensure that the electrical signal from only one neuron can be detected. If the impedance of the electrode is reduced to around $0.5\text{M}\Omega$, the reception area of the electrode will be large enough to include several neurons. This type of recording is called multi-unit recording. Both single-unit and multi-unit recordings emphasize the time of action potentials, which last a few millisecond and requires sampling frequencies above 20 kHz. In order to generate the time stamps of unit activity, spike detection and spike sorting must be applied to the high-pass filtered (300-5000 Hz) extracellular signals.

Local field potential, on the other hand, is the low frequency component (0.1-300 Hz) of the electrical signal recorded extracellularly. The low impedance of the electrode allows for detection of electrical signals from a relatively large volume. Local field potential is often considered to be the spatial combination of a large amount of post-synaptic activity, even though the exact biophysical origin of this signal is less understood.

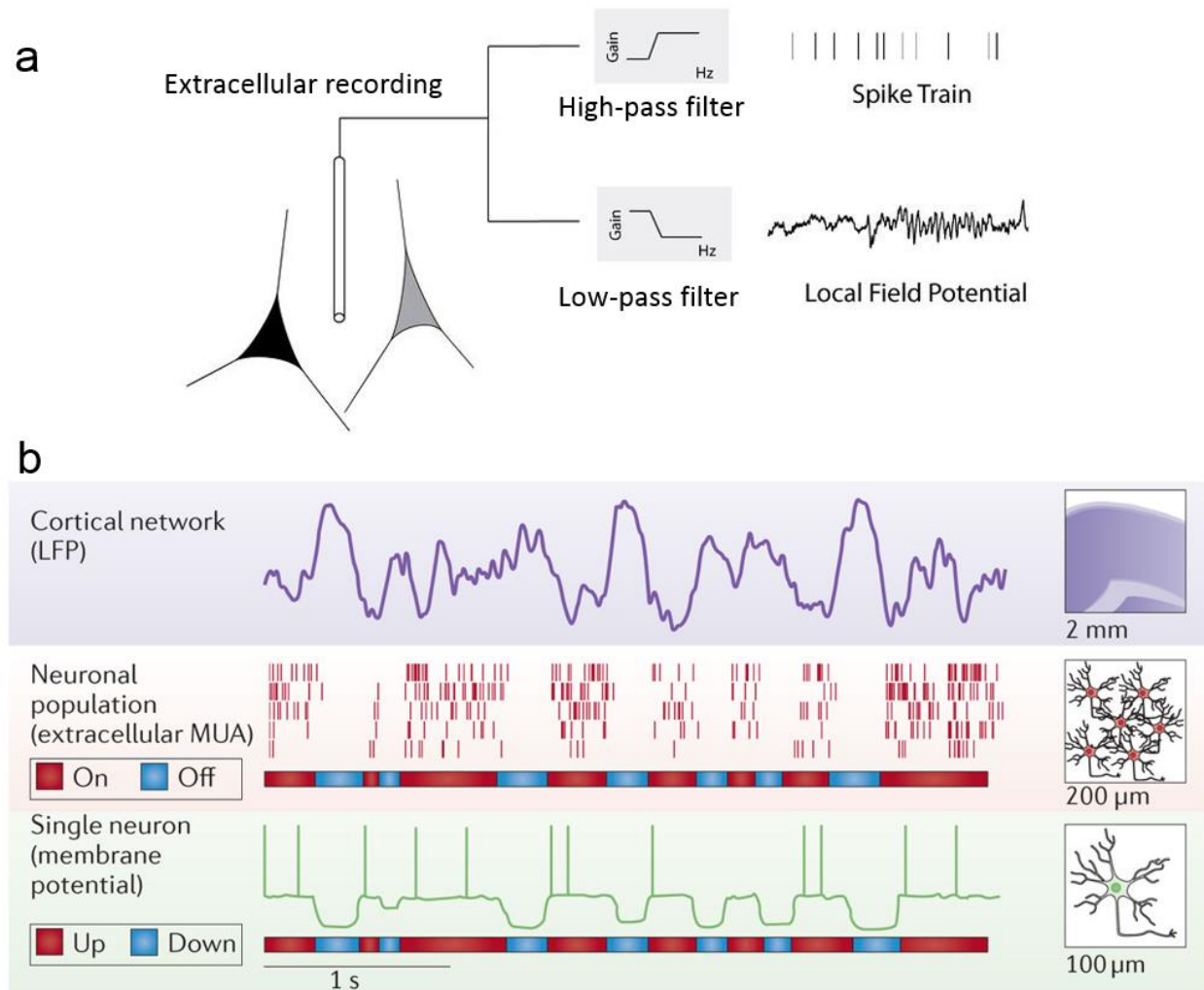


Figure 2. 2 Illustration of extracellular recordings in electrophysiology. (a) Schematic diagram demonstrating that the extracellular recording can be separated into unit activity (high frequency component) and local field potential (low frequency component) according to the frequency. Figure adapted from Berens et al. (2008). (b) Example signals of local field potential (top), multi-unit activity (middle) and intracellular membrane potential recorded from a single neuron (bottom) in a rat during non-rapid eye movement sleep. The ‘on’ periods indicate a state of globally synchronized neuronal activation, while the ‘off’ state comprises generalized population silence and inactivation. Figure adapted from Vyazovskiy and Harris (2013).

2.1.3 Electroencephalography (EEG) and Electrocorticography (ECoG)

Another type of electrophysiology that is most commonly used in clinical settings is electroencephalography (EEG). The electrodes for EEG detection are usually placed on the scalp, making this type of detection non-invasive. The skull and scalp insulate the high frequency components ($>50\text{Hz}$) in the electrical signal (Tatum, 2014) and the remaining EEG is subdivided into several bands based on frequency. One common set of division is the delta ($<4\text{ Hz}$), theta (4-8 Hz), alpha (8-12 Hz), beta (12-30 Hz) and gamma ($>30\text{ Hz}$) bands. Similar to EEG, intracranial EEG, or electrocorticography (ECoG), also uses a low-impedance surface electrode grid. However, the electrodes of ECoG are placed directly on the exposed brain instead of recording electrical signal from outside the scalp. Therefore, ECoG is a more invasive procedure compared to EEG but inherently processes higher spatial resolution and is commonly used in clinics to determine the origin of epileptic seizures.

2.2 Non-invasive neuroimaging techniques

Even though electrophysiology is the most direct way to record neural activity, this method is limited in clinical settings. Spurred by the need to observe dynamic human brain function non-invasively, researchers began to develop neuroimaging technologies, including single-photon emission computed tomography (SPECT), positron emission tomography (PET) and functional magnetic resonance imaging (fMRI). These techniques have since been widely applied to clinical diagnosis.

2.2.1 Radioactive neuroimaging

The biggest challenge for in vivo non-invasive neuroimaging is access to the brain itself, as it is well-protected by the skull and scalp. Since most of the visible and near visible light will be blocked by the bony tissue, scientists have turned their eyes to electromagnetic waves that have significantly shorter wavelength. Gamma rays, with wavelengths less than 10 picometers, have become the detection agent in SPECT. Radioactive tracers with a gamma-emitting isotope are introduced into the bloodstream through injections. The emitted gamma rays detected by a rotating gamma camera can be reconstructed in 3-D using computation tomography (CT). Radioisotopes chosen for SPECT are usually heavy elements with a long half-lives. In the field of neuroimaging with SPECT, the signal from the radioactive tracer usually correlates with regional brain perfusion and metabolic assumptions. Even though SPECT has relatively poor resolution both spatially (on the centimeter scale) and temporally (tens of seconds to minutes) compared to PET and fMRI, it is the most accessible and least expensive neuroimaging technique, and has been proven to assist in diagnosing neural degenerative diseases such as Alzheimer's disease.

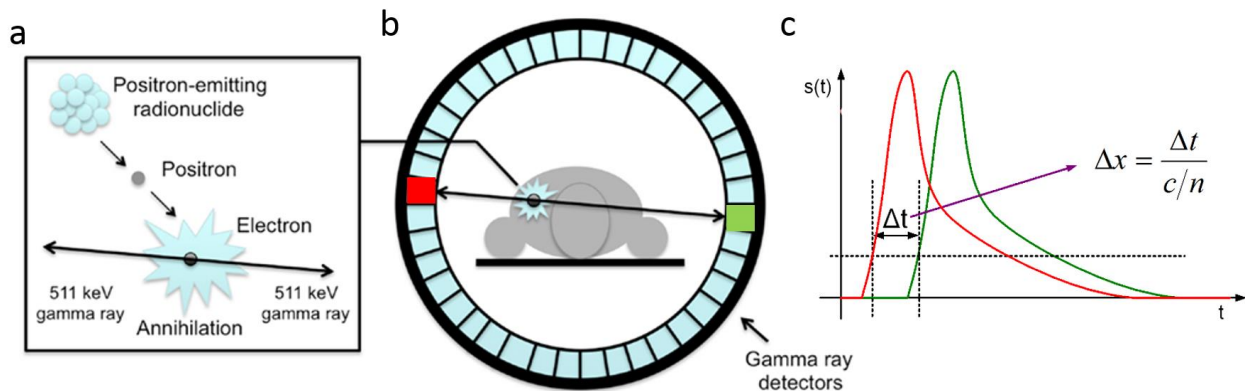


Figure 2. 3 Schematic illustration of positron emission tomography. (a) The process of positron emission and annihilation, which generates a pair of anti-parallel gamma ray photons. (b) The released gamma ray pairs released by the positron are received by the ring-shaped detectors. (c) The difference in arrival time between two detectors informs the location of the positron-emitting radionuclide. Figures adapted from van der Veldt et al. (2013).

Another modern nuclear medical technology, PET, also makes use of gamma rays to access the in vivo brain non-invasively. However, unlike SPECT, the PET detector receives pairs of gamma photons released by positron annihilation. Positron emission is one of two types of beta decay, in which a proton is converted into a neutron and a positron is released in the process. The emitted positron quickly finds an electron and annihilates, releasing a pair of anti-parallel gamma photons (Figure 2. 3a). The energy of a positron-emission released gamma ray, which can be calculated by leveraging the conservation of energy during annihilation and the power of each gamma photon is around 511 keV. The gamma ray detector for PET is usually ring-shaped and by calculating the position of the detectors and the difference in arrival time between the two photons, the location of annihilation can be determined. The positron emitting radioactive isotopes chosen for PET imaging generally have short half-lives. For example, to study the changes of cerebral blood flow and cerebral blood volume, ^{15}O -labeled H_2O is often used (Eichling et al., 1975; Raichle et al., 1983). Later, with the development of radioligands, ^{18}F -labeled fludeoxyglucose (FDG) which is an analogue of glucose, became widely used in multiple fields including neuroimaging as well as clinical oncology (Reivich et al., 1979). The spatial resolution of PET is considerably higher than SPECT, due to the pair-wise detection of gamma rays. Even though the time delay between the gamma photon pairs is on the nanosecond scale, numerous incidences need to accumulate to form the contrast for PET scanning. The temporal resolution of PET is typically around tens of seconds.

2.2.2 Magnetic resonance imaging

The development of MRI has facilitated the discovery of physical phenomenon called nuclear magnetic resonance (NMR) in 1946. Nuclei with an odd number of protons have an intrinsic spinning moment, and when placed in a static magnetic field they are aligned in the same direction

of the magnetic field. To perturb the alignment, additional energy at the resonance frequency is transmitted through radiofrequency pulses which tilts the spinning momentum perpendicular to the static magnetic field. According to the principle of NMR, the required perturbation frequency is proportional to the strength of the static magnetic field and related to the property of the nuclei. Once the perturbation is removed, the nuclei relaxes from a high energy state to equilibrium while releasing energy at a measurable radio frequency. This signal, known as free-induction decay (FID) response signal, forms the MRI image.

In order to produce 3-dimensional images based on FID signal, gradients are added in each axial direction. Because the resonance frequency is directly dependent on the strength of the magnetic field, the axial position in space is encoded by the detected frequency. Specifically, each reading contains information of one row with their position in the x-direction encoded in frequency. By applying a gradient in y, the line projections from multiple angles are obtained, and the image of brain slice is reconstructed by back-projection algorithm that have been used in computed tomography. To enable slice selection, a gradient is introduced in the same direction of the static magnetic field (z direction), so that the radiofrequency pulses can only excite a plane in the selected z direction.

Even though all isotopes containing an odd number of protons respond to a magnetic field, hydrogen isotopes are the most widely used to form MRI contrast due to the natural abundance of hydrogen atoms (99.985%) in the human body (Danquah, 2017). For this reason, MRI eliminates the reliance on exogenous contrast agents to form contrast and is the least invasive neuroimaging technique.

2.2.3 Functional MRI

While MRI can reveal static anatomical structures in 3D based on the distribution of hydrogen atoms in the brain, functional MRI focuses on dynamic changes by repetitive MRI scanning throughout the brain. However, since changes in the distribution of hydrogen atoms are minimal over time, other compounds have been considered to form signal contrast in a magnetic field. Deoxygenated hemoglobin (deoxy-hemoglobin, or HbR) has natural advantages for being a targeted molecule of fMRI: (1) deoxy-hemoglobin is paramagnetic, which means it has unpaired electrons rendering it susceptible to magnetic fields to produce detectable MRI contrast, (2) studies have shown that changes in blood flow and blood oxygenation in the brain are closely related to local neural activity and (3) the changing rate of blood flow is relatively slow and matches the repetition rate or sampling frequency of fMRI (~1Hz). Therefore, since the development of fMRI in 1992 by Seiji Ogawa (Ogawa et al., 1993), changes in cerebral deoxygenated hemoglobin concentration as measured by fMRI, termed blood-oxygen-level-dependent (BOLD) signal, have been used as the primary method to study the functionality of human brain non-invasively.

The spatial resolution of fMRI depends on the strength of the static magnetic field. A stronger magnetic field suggests better image resolution. In clinical settings, MRI scanners usually have a magnetic field around 1.5 T and a spatial resolution of several millimeters. Scanners used for small animals can have magnetic fields of up to 9 T, and with the help of additional contrast agents, the spatial resolution can reach 100 micrometers. The temporal resolution is determined by the sampling time or repetition time (TR), which stands for the amount of time between two successive RF pulses applied to the same slice. TR is heavily dependent on the number of voxels that the MRI scanner raster through. For a human full brain scan, each repetition takes several seconds. In some applications, to achieve higher temporal resolution (around 100 millisecond) the number of slices

is reduced to the minimum capacity in order to only cover the region of interest. However, the repetition time needs to be sufficiently long so that the net magnetization fully relaxes to the equilibrium before the next excitation.

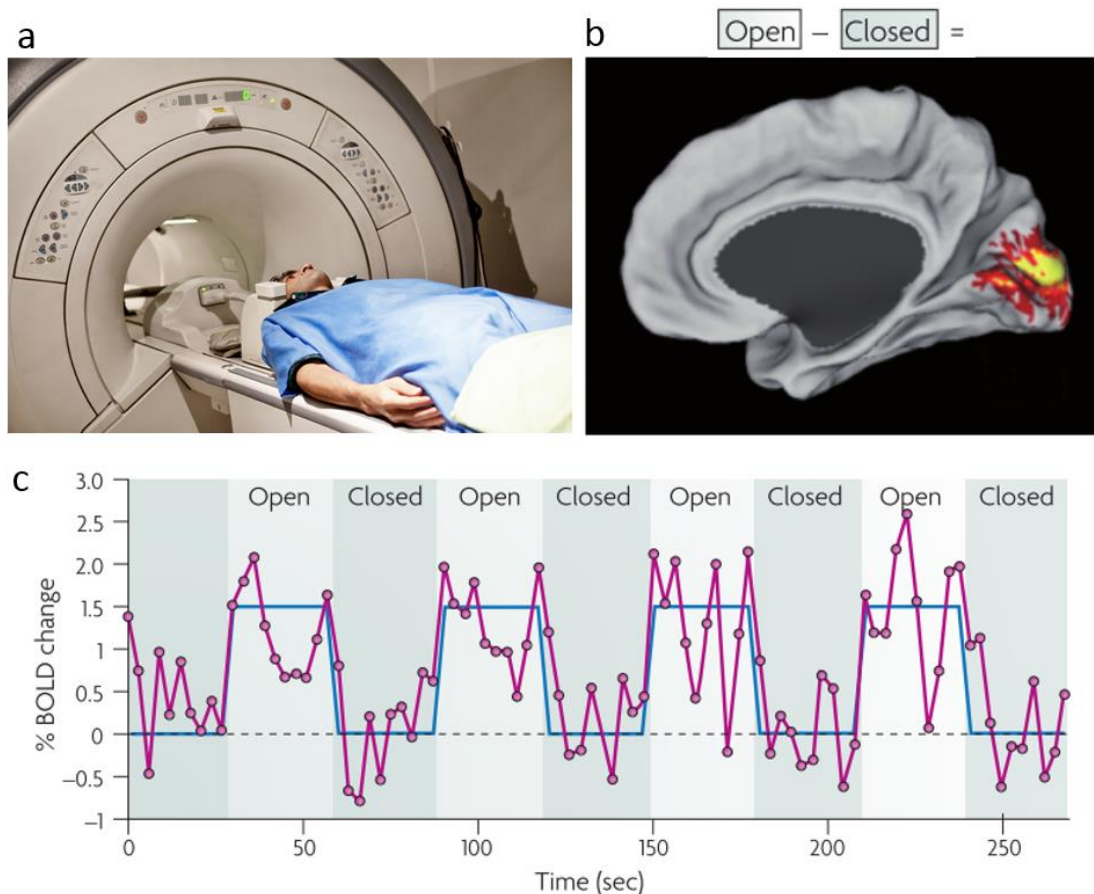


Figure 2. 4 fMRI scanning and standard analysis for functional mapping. (a) Example of an MRI scanning machine. (b) Extraction of a functional region (visual cortex) by subtracting averaged eye-closed epochs from averaged eye-open epochs. (c) Time courses of the fMRI BOLD signal from primary visual cortex during repetitive eye opening and close task. Figures adapted from Fox and Raichle (2007).

Even though fMRI has outstanding spatiotemporal resolution compared to other neuroimaging techniques, changes in the BOLD fMRI signal are difficult to determine due to the high noise level and the small changes in the concentration of HbR. Therefore, traditional ways of mapping functional regions require the patient to repeat the task several times. For example, to map the

human primary visual cortex in human brain, patients were asked to open and close their eyes repetitively. The epochs from the same condition were averaged to reduce variations between different physiological conditions. The eyes-closed condition was subtracted from the eyes-open condition to highlight the regions that were modulated by the task, which in this case was the primary visual cortex (Figure 2. 4).

2.2.4 Magnetoencephalography

Magnetoencephalography is an innovative way to record brain activity by detecting the magnetic fields induced by changing electrical currents associated with neural activity. The temporal resolution of MEG, typically in the range of millisecond, is comparable to EEG. Spatial discrimination can reach several millimeters (Hamalainen et al., 1993). However, MEG is technically challenging compared to EEG because the weak magnetic fields induced by brain's activity is usually on the scale of 10^8 , which is smaller than noise. To address the SNR issue, MEG uses superconducting quantum interference devices such as detection arrays. However, these devices require helium cooling and magnetic field shielding, making MEG much more expensive to acquire than EEG.

2.3 Optical Imaging

Observing brain function with light comes with a unique set of merits and limitations. Unlike the BOLD fMRI signal, which can be detected through the skull and brain tissue, light in the visible and near-infrared spectrum is severely scattered by biological tissues at short wavelength. Therefore, the sample needs to be directly exposed to light in order to be imaged optically, making optical imaging a more invasive approach. On the other hand, shorter wavelengths provide

outstanding spatial resolution capable of resolving details of function or anatomy where other techniques cannot. Moreover, unlike Gamma rays and X rays, the electromagnetic waves in the visible and near visible band have limited ionizing effects on biological tissues, making them ideal for in vivo imaging applications.

There are a number of different ways to image the brain optically. Some of the techniques, such as two-photon laser scanning microscopy and confocal microscopy, require fluorescent labeling of neurons to provide contrast. Other methods including intrinsic optical imaging, optical coherence tomography and laser speckle contrast imaging directly measure the changes in vasculature and infer the underlying neural activity via neurovascular coupling. Here, I will briefly review two-photon microscopy and laser speckle contrast imaging and their application for in vivo neuroimaging.

2.3.1 Two-photon Microscopy

Traditional fluorescence microscopy utilizes fluorescent stains that bind to specific cellular structures to provide optical contrast. A given fluorophore receives energy from a single photon and releases photon with lower energy. Optically imaging deep structures in the intact brain, however, is complicated by heavy scattering at the cortical surface, which prevents single-photon excitation light from penetrating deep into the tissue. In two-photon laser scanning microscopy, fluorescence excitation is achieved by delivering two photons with half the energy of a single photon excitation. The arrival time of the two photons need to be close enough (on femtosecond scale) to achieve the same excitation. This excitation mechanism ensures that only the fluorophores within the focal point get excited (demonstrated by Figure 2. 5) which allows for both optical sectioning at the focal plane, and decreased photo-bleaching and tissue damage to the regions

above and below the focal plane. Another merit of two-photon excitation comes with the usage of longer wavelength light, which reduces scattering effects and increases penetration depth in the tissue.

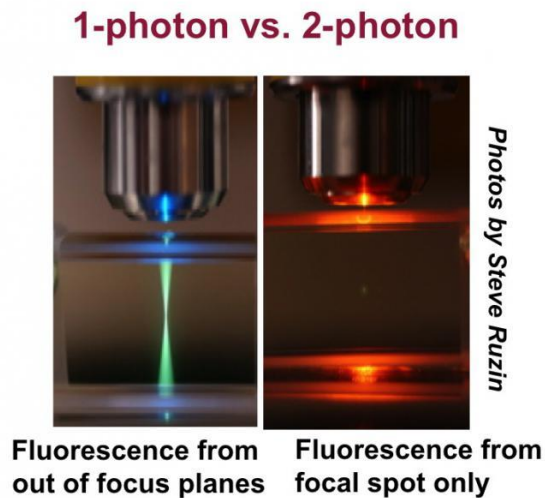


Figure 2. 5 Illumination profile of one-photon and two-photon excitation. Photo credits to Steve Ruzin and Robey lab at U.C. Berkley.

With proper fluorescent labeling, two-photon laser scanning microscopy can visualize brain's structures and dynamics up to 600 μm deep into the living brain. To visualize cerebral vasculature in vivo, fluorescence dyes such as fluorescein (FITC) and Texas Red conjugated with dextran polysaccharides are administered intravenously into circulation. The blood-brain barrier prevents large molecular structure such as dextran conjugated dyes from leaking into the blood stream. However, labeling the neurons and glia cells in the intact and living brain is more challenging, which usually involves loading, incubating and washing the synthetic calcium indicator on the exposed cortex.

Recent development of genetically encoded calcium indicators (GECIs) provides a brand new approach to overcome the technical difficulties and enables chronic imaging of neural activity in

the awake and behaving animal. As a result, researchers have incorporated use of head restrained of transgenic mice with GECIs labeling into two-photon microscopy. Figure 2. 6a illustrates an example of such a system. Another merit of GECIs as compared to synthetic dyes is selective labeling, which is achieved by cell-type specific promoters or cellular targeting sequences. Figure 2. 6b displays a two-photon image of pyramidal cells at cortical layer II/III in an awake behaving mouse that was virally transfected by the Thy1 promoter and Figure 2. 6c plots the GCaMP fluorescent changes in the cell body along with the animal's movement on the treadmill (Tian et al., 2009).

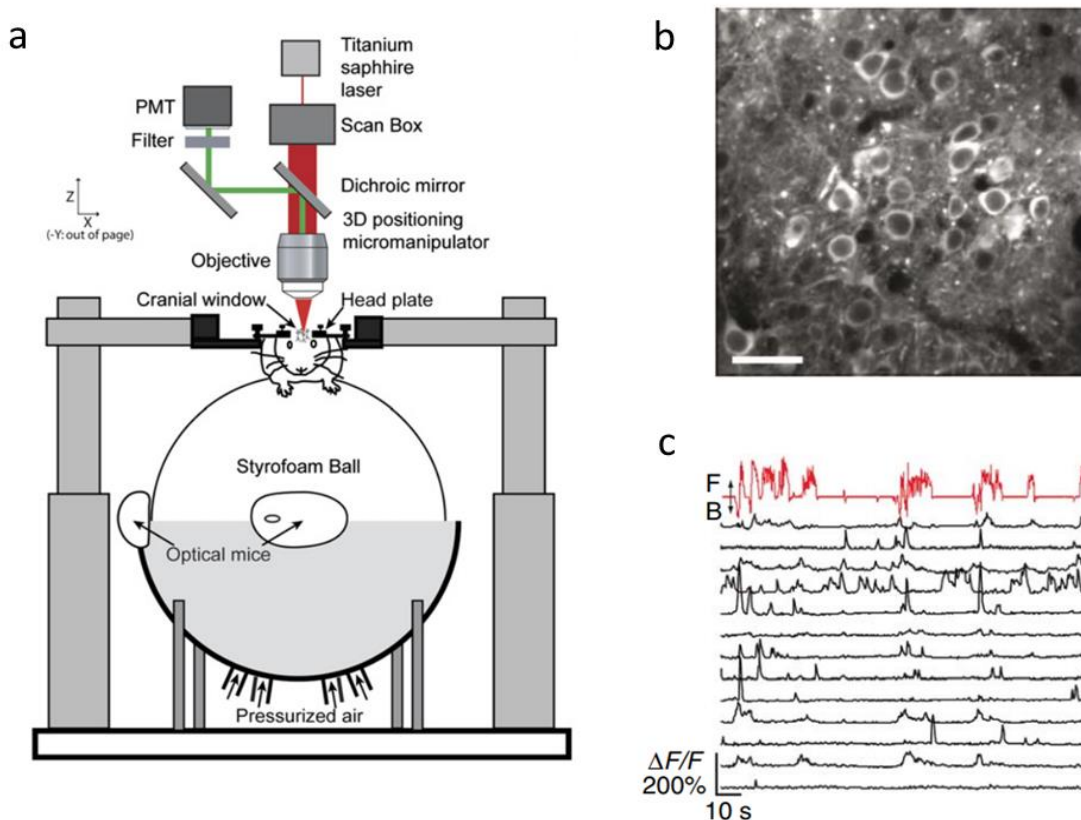


Figure 2. 6 Demonstration of two-photon microscopy in chronic awake mouse imaging. (a) Schematic diagram of the experimental setup used to image an awake, behaving mouse that is able to maneuver the spherical treadmill

(Dombeck et al., 2007). (b) GCaMP3 expression in layer II/III pyramidal cells in the primary motor cortex. (c) Fluorescent traces of the neurons segmented from (b), aligned with the treadmill movement plotted in the red (Figure adapted from Tian et al., 2009).

2.3.2 Laser Speckle Contrast Imaging

A speckle pattern, or random interference pattern is formed by the constructive and destructive interferences when illuminating a surface with coherence laser light. While most optical imaging techniques attempt to reduce speckle patterns, laser speckle contrast imaging makes use of the altered interference pattern when coherent light hits moving, scattering particles to provide contrast. For in vivo brain imaging, the red blood cells in the vasculature are the primary moving scattering source which induces the blurring of the speckle pattern. To quantify the alteration of the speckle patterns, the statistical distribution of constructive and destructive events over either a period of time or an area is calculated. In areas of increased blood flow velocity, there is more blurring of the speckle pattern and therefore, reduced variability in the interference. Therefore the speckle contrast is defined as the ratio of the standard deviation to the mean intensity, and the contrast value can be calculated either temporally or spatially. In practice, the spatial speckle contrast is usually calculated with a 7x7 pixel moving window and the temporal speckle contrast needs to be around 30 time points to provide decent contrast. Configuring the two constants needs to be based on the specific application in order to balance the trade-off between spatial and temporal resolutions.

According to the definition of speckle contrast, the value of the contrast is inversely proportional to the blood flow. As demonstrated in Figure 2. 7 (c) and (d), the speckle contrast and flow contrast are inversely related. Speckle contrast is useful for visualizing small vessels and capillaries that cannot be resolved in the reflectance imaging (Figure 2. 7 (a)), while the flow contrast is more

sensitive to the flow changes in the blood vessel. Laser speckle contrast is indicative of the level of motion in the sample, but the absolute value of the cerebral blood flow cannot be determined by this method. As a result, the changes in blood flow responding to external stimulus is of more interest when studying the brain's functionality.

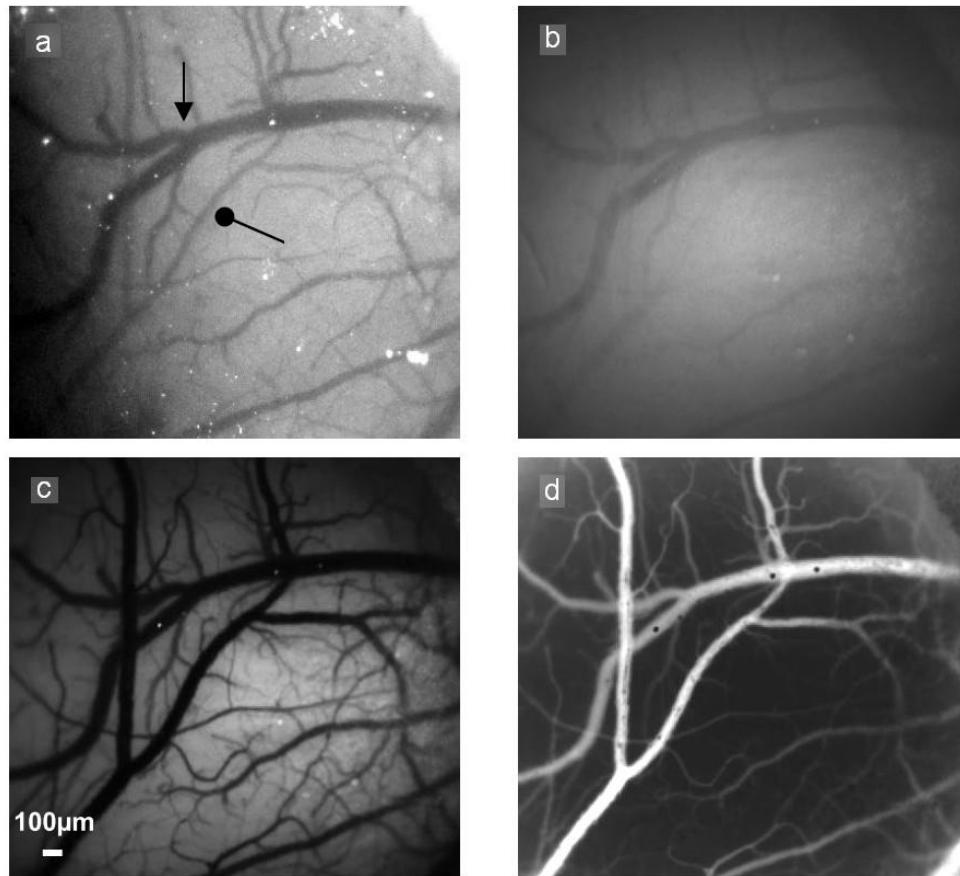


Figure 2. 7 Studies of cortical blood flow in the rat barrel cortex using laser speckle contrast imaging. (a) white light reflectance image, (b) red laser reflectance image, (c) temporal laser speckle constrast image and (d) cerebral blood flow image over the same field of view. The dot arrow marks a pial artery and the sharp arrow marks a vein (Adapted from Li et al., 2011).

2.4 Summary

This chapter has introduced several methods for monitoring dynamic changes in the brain. Some techniques, such as EEG and MEG, directly measure neural activity, while others including PET, SPECT, fMRI and speckle imaging rely on cortical blood flow and metabolism. The temporal resolution, spatial resolution and field of view of the most clinically applicable modalities are compared in

Table 1.

Table 1. Spatiotemporal resolution of the most commonly used neuroimaging modalities.

Imaging method	Temporal resolution	Spatial resolution	Field of view
Electrophysiology	<1 ms	>10 mm	Localized to electrode
PET	Around 45 s	>5 mm	Whole brain
SPECT	Around 60 s	>6 mm	Whole brain
fMRI	200ms-1 s	1-5 mm	Whole brain
MEG	<1 ms	>5 mm	Brain surface

Optical neuroimaging methods have various modalities, and while their spatiotemporal resolution may differ across applications, they generally have better spatiotemporal resolution than fMRI and PET. On the other hand, their field of view is limited to the surface of brain.

The field of neuroimaging in both clinical and research settings has benefited from technological advancements over the years. The rapid progression of various neuroimaging applications has enabled us to observe the brain's morphology, as well as functional dynamics from the systemic level to molecular level. Each of the techniques has its unique advantages, limitations and specific applications. Combining the data and comparing the results across these tools will provide a

comprehensive picture of the functional organization of the brain, and facilitate rapid development in translational research of brain health.

Chapter 3

Wide-field optical mapping (WFOM) of cerebral neural and hemodynamic activity

3.1 Introduction

Although modern techniques such as two-photon microscopy can now provide cellular-level imaging of the intact living brain, the speed and fields of view of these techniques remain limited. Conversely, wide-field optical mapping (WFOM), a simpler technique that uses a camera to observe large areas of the exposed cortex under visible light, can detect changes in both neural activity and hemodynamics at very high speeds. This new imaging modality exploits light emitting diodes (LEDs), sensitive and high-speed digital cameras and genetically-encoded fluorophores that can report neural activity. Thus, although WFOM does not provide single-neuron or capillary-level resolution, it delivers the ability to map neural activity and hemodynamics simultaneously over large areas of the brain in awake, behaving mammals at speeds fast enough to observe

widespread neural firing events, as well as their dynamic coupling to hemodynamics. This chapter provides a description of WFOM implementation for simultaneous mapping both neural activity and hemodynamics, analysis and interpretation of the signals including correction of fluorescence for hemodynamic cross-talk as well as verification of the method with electrophysiology.

3.2 Methods and Materials

3.2.1 Genetically-encoded calcium indicators (GECIs)

A major advance in neuroscience in the past 10 years has been the refinement of genetically-encoded calcium indicators (GECIs). These indicators were built upon the development of green fluorescent protein (GFP), which can be selectively expressed in genetically-targeted cell types by incorporating the gene for the production of GFP into the genome of the organism in the region of the DNA that codes for the targeted proteins (Chalfie et al., 1994). Modification of GFP allowed its fluorescence to be calcium sensitive, such that animals can now be bred (or virally transfected) to express calcium sensitive fluorescence within select cell types such as excitatory (Akerboom et al., 2013) or inhibitory neurons (Akerboom et al., 2013), but also cells like astrocytes (Khakh and Sofroniew, 2015). GECIs, like calcium sensitive dyes, are slower reporters of neural activity than voltage sensitive dyes. However, GECIs offer (continually improving) levels of $\Delta F/F$ that are similar to calcium sensitive dyes, with the major benefit that bulk-loading of a dye is not needed. Strains of animal can be bred with genetically-selective expression of GECIs (generally GCaMP) throughout the brain, or in selective regions targeted with viral injections or in-utero electroporation. It is this widespread availability of fluorescent indicators of neural activity that has yielded a surge in studies using in-vivo two-photon microscopy to study the dynamics of single

neurons in the rodent brain. However, such indicators also provide the unique opportunity to employ WFOM techniques to map neural activity across large regions of the brain, in parallel and at high temporal resolution (Vanni and Murphy, 2014; Xu et al., 2015; Kozberg et al., 2016).

Continuing work is seeking to develop improved GECIs including red-shifted RCaMPs (Akerboom et al., 2013). Notably, work is also progressing on the development of genetically-encoded voltage indicators (GEVIs), which are bringing the promise of much higher speed fluorescent tracking of neural activity, on the scale of single action potentials (St-Pierre et al., 2014; Carandini et al., 2015; Gong et al., 2015). The expression of GECIS are regulated by the promotor, which makes cell type-specific labeling possible. In this thesis, one of GFP-based GECIs, the GCaMP family, has been used to detect calcium dynamics induced by neural activation. Under the regulation of the Thy1 promotor, GCaMP is selectively expressed in the excitatory neurons in the cortex, hippocampus, thalamus, superior colliculus, cerebellum and various nuclei in the brain stem (Figure 3. 1A). The cortical excitatory neurons in layer 2/3 and 5 are densely labeled (Figure 3. 1B).

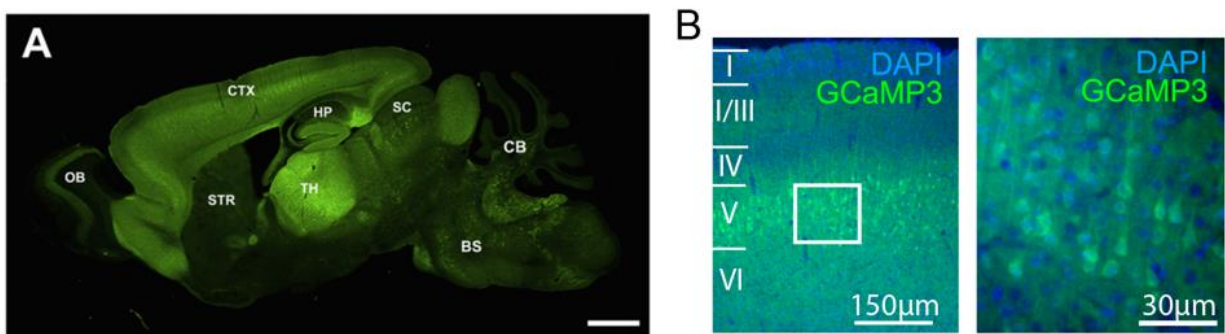


Figure 3. 1 Expression patterns of Thy1-GCaMP3 transgenic mice. (A) A sagittal section of brain from a Thy1-GCaMP3 mouse (Chen et al., 2012). (B) Thy1-GCaMP3 mouse cortical section at 4x (left) and 20x (right) shows selective expression of GCaMP in cortical layer 2/3 and 5 pyramidal neurons.

3.2.2 Animal preparation

A range of techniques have been developed for exposing the cortex for WFOM. Placement of cranial windows is performed under anesthesia, usually isoflurane, ketamine-xylazine or urethane (non-survival). After shaving and retraction of the scalp, the surface of the skull is cleaned of membranes and dried (in non-survival studies, additional surgery may be performed beforehand to place cannulas for drug delivery or monitoring, or tracheotomies for ventilation).

Basic thinned skull window:

Early acute studies, particularly in rats, would expose relatively small regions of cortex (e.g. 3 mm x 4 mm) by thinning the skull using a dental burr. Gentle thinning, with water irrigation to reduce heating and dust, can reduce skull thickness to 20-50 microns allowing a clear view of the underlying cortex. Drilling is typically done initially with a coarser drill bit, moving to smaller, finer drill bits to create a smooth final window. Great care must be taken to avoid puncturing the skull, and pressing on the soft thinned skull which can cause microhemorrhages in the underlying dura / brain, obscuring imaging. Drilling over the sutures of the skull can cause significant bleeding, so windows are often bounded by sutures (e.g. unilaterally between bregma and lambda). Once thinned, windows would be surrounded by either dental acrylic (methyl methacrylate polymer) or petroleum jelly to support a well of liquid such as water or mineral oil. This liquid serves to index-match the slightly rough surface of the skull to enhance translucency and simplify reflections of light from the skull's irregular surface. Alignment of optics must ensure that the single specular reflection from the surface of the liquid does not enter the camera.

Skull-removed cranial window:

Common for in-vivo two-photon microscopy, fully exposed cortex preparations can also be used for WFOM, allowing clearer visualization of cortical vasculature without dural vessels in view as well as the chance to do multi-scale wide-field and cellular level microscopic imaging in the same animal. Such windows can be prepared as above, initially by thinning the skull, at least in a ring around the region to be exposed. Once thinned, the piece of skull can be lifted using sharp tweezers and removed. Removal of the dura is usually necessary in rats, although less-so in mice where dural removal can be very challenging and damaging to the brain. In rats, mitigating swelling is important such that the brain is recessed underneath the dura. In acute preparations, this brain swelling can be reduced by puncturing the IVth ventricle at the base of the back of the skull prior to removal of the piece of skull. Some researchers also give intraperitoneal mannitol before surgery to mitigate brain swelling (Shibuki et al., 2003). After skull removal, a sharp needle can be used to raise the dura and allow it to be cut or torn. Dural vessels extend up from the lateral side of the head, so cutting medially and folding the dura laterally can reduce bleeding compared to cutting the lateral edge. Care should be taken not to touch the brain, or let blood sit on the surface of the brain. The preparation should be irrigated with sterile and pH-balanced artificial cerebral fluid (ACSF) at body temperature. Once exposed and stable, the brain should then be covered with a glass (or similar) cover-slip, typically with a drop of sterile ACSF in low-scattering ~1% agarose between the brain and the window (at body temperature). Critically, once the skull is open significant brain motion is likely to occur during imaging, with heart beat and breathing as well as any animal motion. This motion can be reduced by very carefully ensuring that the glass window is rigidly and completely sealed to the skull using dental acrylic. This requires the skull to be completely dry. Properly covering the exposed cortex is also important as exposure to room air

can alter the physiological state of the brain compared to closed-skull preparations, a factor we have found to be particularly important for imaging flavin adenine dinucleotide (FAD) fluorescence dynamics. These constraints make it challenging to combine wide-field optical imaging with electrophysiology and / or superfusion of the brain with dyes or pharmacologic agents, although creative strategies for the latter have been developed (Ngai and Winn, 2002). Thinned-skull preparations are usually more robust for simultaneous electrophysiology experiments, where a very small hole can be made in the skull, limiting motion and contamination of the brain (Berwick et al., 2008).

Chronically implanted cranial windows for awake imaging

The recent move towards imaging in the awake, behaving brain requires development of more complex methodologies to implant cranial windows. Waking and imaging an animal immediately after cranial window surgery is likely to result in data that is strongly affected by the discomfort and distress of the animal. It is thus more common to implant the window under anesthesia, carefully recover the animal with analgesia and rest, and then image on subsequent days, with the benefit that the same animal can then be imaged multiple times longitudinally e.g. in studies of learning, development or disease progression. It is also necessary to consider how to immobilize the head of the animal during imaging relative to the camera. For this, a range of different designs for ‘head-plates’ have been developed that encircle the exposed region, which are generally attached to the skull during the initial cranial window surgery (Hillman et al., 2007).

In all cases, preparatory surgeries must be fully aseptic, and must be performed under anesthesia, usually with pre-operative (and follow-up) administration of analgesia such as buprenorphine to mitigate post-operative pain. Small cranial windows with removed skull, and sometimes dura are common for in-vivo two-photon imaging experiments. However, larger glass windows over skull-

removed craniotomies, as desirable for WFOM, are far more challenging to maintain longitudinally. Our highly successful approach builds upon skull-thinning approaches developed by Drew et al (Drew et al., 2010) but extended to the entire superficial cortex of the mouse. Mice are anesthetized with isoflurane, homeothermically maintained and monitored using pulse oximetry. The scalp over the craniotomy area is resected back to prevent interference with drilling. Skull thinning is then performed with constant saline irrigation, avoiding excessive drilling of the sutures but ensuring maximal removal of skull vessels or opaque skull. The thinning area can be extended beyond the bound of bregma and lambda, towards the frontal area for visualizing motor cortex or occipital area for cerebellum as needed. Once drilled to translucency, the dry surface of the skull is coated with a thin layer of cyanoacrylate (liquid-type Superglue™) which serves to index-match the rough surface of the skull, prevent bone re-growth and provide mechanical protection. The skin around the thinned skull preparation is sealed using cyanoacrylate tissue adhesive (e.g. 3M™ Vetbond™ Tissue Adhesive). In our case, a custom-made head-plate made from laser-cut acrylic plastic is used to enable immobilization. This approach enables custom-fit, rapid manufacture of head-plates for each mouse, and results in a light and un-obtrusive head-plate for the mice. The design encircles the bilaterally-exposed cortex, and is glued to the skull using cyanoacrylate (gel-type Superglue™). To protect the thinned skull during recovery, a layer of Kwik-Sil™, a two-part, rapid cure silicone rubber is placed over the window and can be peeled off for imaging (and then renewed following imaging). Post-operative care ensures that animals are properly hydrated, have adequate pain relief and are in an environment where they cannot catch or damage their head-plates. Training of animals to perform behavioral tasks can be performed before surgery (with head-fixing) and following post-operative recovery.

Similar approaches have been used for imaging the cat and primate cortex. In the latter case, chronic windows include surgical removal of dura within the window, and cranial windows can be dismantled and cleaned to ensure optical clarity for extended periods of time (Sirotin and Das, 2009).

3.2.3 Imaging Instrumentation

A microcontroller monitoring the camera's 'expose' signal can be used to generate signals to selectively illuminate different color LEDs in sequence, while allowing the camera to run at its fastest free-running speed (Bouchard et al., 2009; Sun et al., 2010). LEDs should each be band-pass filtered to ensure accurate knowledge of the illuminating wavelengths for subsequent spectral analysis, and can be combined using dichroics to yield a single beam that can be used to illuminate the brain. The use of LEDs means that wavelengths can be changed adaptively, and brighter illumination can be achieved for wavelengths where broadband light sources typically have lower power (e.g. UV or blue colors). Modern LEDs can also have their power levels adjusted electronically, meaning that the relative intensities of each wavelength band can be tuned to maximize dynamic range of the imaging system across all colors. The effective frame rate of imaging is the camera's frame rate divided by the number of spectral bands used.

The strobed LED strategy described above offers an ideal way to incorporate fluorescence imaging into multi-spectral reflectance imaging. The system can be modified slightly by including an LED at the fluorophore's excitation wavelength (e.g. peaking around 488 nm for GCaMP), and adding a long-pass emission filter (e.g. 500 nm) positioned in front of the camera (illustrated in Figure 3. 2a). During illumination of the cortex at wavelengths such as 530 nm and 630 nm, diffuse reflectance will pass through the 500 nm long-pass filter and be imaged onto the camera yielding

data for hemodynamic analysis. However, during (much brighter) 488 nm LED illumination, this excitation light will be blocked, enabling detection of green fluorescence from GCaMP (Figure 3. 2b). It should be noted that a high quality band-pass filter in front of the blue LED is required to ensure that light from the edges of the LED spectrum does not leak through the 500 nm long-pass filter. This powerful strategy can be further expanded to include a near infrared laser diode within the strobe-order to collect laser speckle images from which blood flow can also be calculated (Devor et al., 2003).

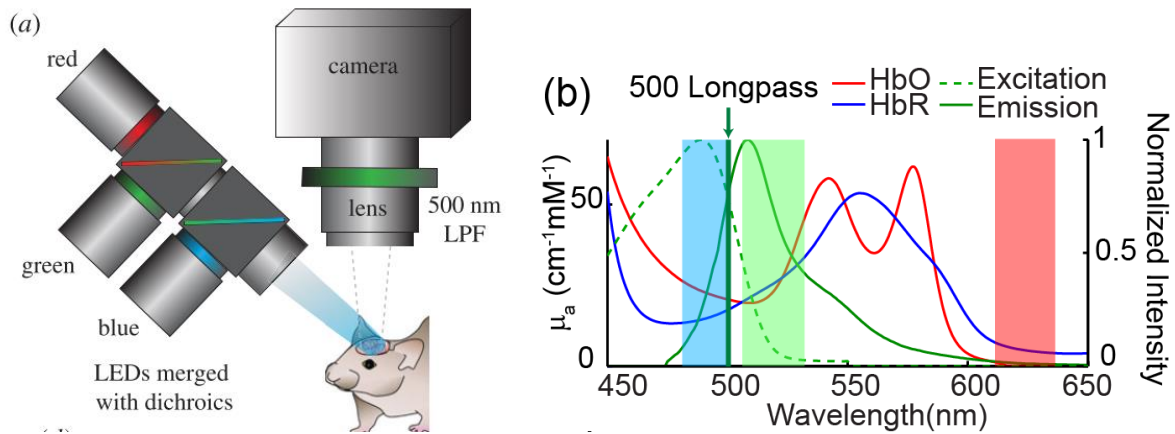


Figure 3. 2 Instrumentation for WFOM and examples of raw diffuse reflectance data. (a) Imaging system including blue, green and red LEDs illuminating the surface of the cortex – the resulting reflectance and fluorescence images (500 nm long pass filter - LPF) are recorded by the camera. (b) Absorption spectra of HbO and HbR (left axis) and the fluorescence excitation and emission spectra of GFP (right axis). Blue, green and red shading represents the wavelength bands of the LEDs used for imaging. Conversion of reflectance data into hemodynamics

3.3 Quantification of hemodynamic changes from reflectance WFOM

As described above, the basic method of performing reflectance WFOM is to illuminate the brain with continuous wave visible light and detect an image of the cortical surface using a camera. A sequence of 2D images is acquired over time, usually while the animal receives a stimulus, performs a task or is observed in a 'resting state'. Raw images generally show the surface vasculature of the brain with good contrast, as well as signal originating from deeper layers from light that has been more deeply scattered. When a discrete region of the cortex is activated, the intensity of the diffusely reflected light will change within the local area. This change can be detected by camera and used to map hemodynamic changes of the cortex. Early studies identified that a large contributor to changes in diffuse reflectance was hemoglobin absorption (Malonek and Grinvald, 1996). Moreover, hemoglobin is known to have an oxygenation-dependent absorption spectrum in the visible and near infrared range, corresponding to the bright red color of arterial blood and the darker brown color of venous blood (Figure 3. 2b). It was, therefore, recognized that measurements of diffuse-reflectance changes at specific wavelengths across the hemoglobin absorption bands would differently represent contributions from changes in the local concentration of oxy- and deoxy-hemoglobin ($\Delta[\text{HbO}]$ and $\Delta[\text{HbR}]$) as well as their total ($\Delta[\text{HbT}] = \Delta[\text{HbO}] + \Delta[\text{HbR}]$), which represents a change in local blood volume.

The raw images acquired at different wavelengths carry clear information about the concentrations of HbO and HbR within the cortex. However, to convert reflectance data into estimates of changes in the concentration of hemoglobin, the physical principles of light propagation in scattering brain tissue must be examined. In a simple, absorbing but non-scattering medium the transmission of light will follow Beer's law:

$$I = I_0 e^{-\mu_a x}$$

Equation 3. 1

where I_0 is the incident intensity, and I is the resulting intensity after the light has travelled a pathlength x through the medium with absorption coefficient μ_a . However, the brain is highly scattering at visible wavelengths. In fact, scattering is what permits light entering the brain's surface to be diffusely reflected and detected by a camera focused on the brain's surface. As scattering turns the incident light around, each scattering event adds to the photon's pathlength through the absorbing medium. This redirection also introduces spatial uncertainty in terms of where a photon detected at a particular point on the brain originally entered the brain, and where it visited within the brain. Finally, the light emerging from the brain will exit in a range of directions, based on its last scattering event, such that every photon entering will not necessarily be detected by the aperture of the camera lens. In practical implementations, it is impossible to know precisely how scattering has affected each detected photon across the field of view. However, the overall effects of scattering on Equation 3. 1 can be approximated by the 'modified Beer Lambert law':

$$I = I_0 e^{-\mu_a X + G}$$

Equation 3. 2

where $X = DPFx$, and DPF is the 'differential pathlength factor' which represents scaling of the original pathlength x to account for the longer distance traveled by the photon due to scattering. G represents geometric factors that introduce uncertainty regarding how much of the light exiting the brain can be detected by the camera. Calibrating to know exactly the distribution of I_0 on the brain's surface, as well as geometric factor G can be achieved, but it is possible to use relative

measurements (e.g. dividing by $I_{(t=0)}$) to remove the influence of these common terms.

Incorporating wavelength (λ) and time (t) dependences:

$$\frac{I(t, \lambda)}{I(t_0, \lambda)} = e^{-(\mu_a(t, \lambda) - \mu_a(t_0, \lambda))X(\lambda)} = e^{-\Delta\mu_a(t, \lambda)X(\lambda)}$$

Equation 3. 3

So the change in absorption coefficient from time t_0 to time t can be estimated from the ratio of the detected intensity at time t , relative to the intensity at time t_0 , scaled by a wavelength-dependent estimate of pathlength.

$$\Delta\mu_a(t, \lambda) = \mu_a(t, \lambda) - \mu_a(t_0, \lambda) = \frac{-1}{X(\lambda)} \ln \left(\frac{I(t, \lambda)}{I(t_0, \lambda)} \right)$$

Equation 3. 4

Note that this analysis assumes that scatter is not changing over time, and the wavelength-dependent pathlength in the brain is known.

Considering the contribution of hemoglobin, assuming that Equation 3. 4 holds, and if the only change occurring in the brain is the concentration of absorbers in the tissue, the final step in analysis is to use the following relationship:

$$\mu_a(\lambda, t) = \sum_n \xi_n(\lambda) c_n(t)$$

and thus

$$\Delta\mu_a(\lambda, t) = \sum_n \xi_n(\lambda) \Delta c_n(t)$$

Equation 3. 5

where $\xi_n(\lambda)$ is the molar extinction coefficient of a given chromophore (absorber), and Δc_n is the change in the chromophore's concentration relative to an earlier time point.

As shown previously, in the visible range (400-700 nm) the major absorbers in the brain are HbO and HbR. Below 450 nm, protein absorption increases, while at wavelengths higher than 700 nm, water and lipids can contribute significantly to absorption (Bevilacqua et al., 2000). However, even if these absorbers contribute to the baseline absorption, if we consider only changes in absorption (as in Equation 3. 4) these effects will cancel unless there is a change over time. In this case, only a slight contribution might be expected from changes in cytochrome oxidase (Mason et al., 2014). So with a change over time denoted by Δ below, measurements of $I(t)/I(t_0)$ at two wavelengths can yield the following pair of equations:

$$\Delta\mu_a(\lambda_1) = \xi_{HbO}(\lambda_1)\Delta c_{HbO} + \xi_{HbR}(\lambda_1)\Delta c_{HbR}$$

$$\Delta\mu_a(\lambda_2) = \xi_{HbO}(\lambda_2)\Delta c_{HbO} + \xi_{HbR}(\lambda_2)\Delta c_{HbR}$$

Equation 3. 6

Values of $\xi_n(\lambda)$ correspond to the absolute absorption spectra of HbO and HbR. Values of wavelength-dependent pathlength ($X(\lambda)$) must be estimated. With knowledge of $X(\lambda)$ and $\xi_n(\lambda)$, these equations can be simply solved to find the two unknowns (Δc_{HbO} and Δc_{HbR}) at each pixel, which correspond to the time-varying change in molar concentration of HbO and HbR over time:

$$\Delta c_{HbR} = \frac{\xi_{HbO}(\lambda_1)\Delta\mu_a(\lambda_2) - \xi_{HbO}(\lambda_2)\Delta\mu_a(\lambda_1)}{\xi_{HbO}(\lambda_1)\xi_{HbR}(\lambda_2) - \xi_{HbO}(\lambda_2)\xi_{HbR}(\lambda_1)}$$

$$\Delta c_{HbO} = \frac{\xi_{HbR}(\lambda_1)\Delta\mu_a(\lambda_2) - \xi_{HbR}(\lambda_2)\Delta\mu_a(\lambda_1)}{\xi_{HbR}(\lambda_1)\xi_{HbO}(\lambda_2) - \xi_{HbR}(\lambda_2)\xi_{HbO}(\lambda_1)}$$

Equation 3. 7

For a larger number of wavelength measurements, this analysis becomes a linear model that can be solved through least-squares fitting or other inversion of the matrix form below. However, the analysis above demonstrates that a minimum of two wavelengths are required to determine (and estimate) or the relative changes in HbO and HbR.

$$\begin{bmatrix} \Delta\mu_a(\lambda_1, r) \\ \vdots \\ \Delta\mu_a(\lambda_n, r) \end{bmatrix} = \begin{bmatrix} \xi_{HbO}(\lambda_1) & \xi_{HbR}(\lambda_1) \\ \vdots & \vdots \\ \xi_{HbO}(\lambda_n) & \xi_{HbR}(\lambda_n) \end{bmatrix} \begin{bmatrix} \Delta c_{HbO}(r) \\ \Delta c_{HbR}(r) \end{bmatrix}$$

Equation 3. 8

3.4 Wide-field optical mapping of fluorescence contrast

In addition to hemodynamic and ‘intrinsic signal’ optical imaging, the exposed brain can also be imaged to capture a range of dynamic changes in fluorescence contrast including voltage (Orbach et al., 1985; Shoham et al., 1999) and calcium sensitive dyes (Bouchard et al., 2009; Ma et al., 2014), genetically encoded calcium (Heim et al., 2007; Chen et al., 2013) and voltage indicators (Carandini et al., 2015; Gong et al., 2015) and intrinsic fluorophores as markers of oxidative metabolism (Mayevsky and Chance, 1982).

Instrumentation for imaging fluorescence contrast in a wide-field geometry can be almost identical to that used for reflectance WFOM. The major practical difference is that fluorophores excite with lower wavelength (higher energy) light, and emit at higher wavelengths (lower energy light). This means that the brain must be illuminated at the fluorophore’s excitation wavelength, and this wavelength must be blocked from entering the camera to enable sensitivity to photons at the emission wavelengths. Emission intensities are typically much lower than excitation energies. Additionally, we argue here that reflectance WFOM measurements should always be acquired in

parallel with fluorescence measurements to protect against hemodynamic cross-talk as explained below.

3.4.1 The origin of hemodynamic contamination of wide-field fluorescence data

Figure 3. 3 illustrates the simplified paths taken by light to and from an interaction with a fluorophore. Excitation light must travel a pathlength $X(\lambda_{ex})$ through the brain before reaching the fluorophore, and along this path will experience the absorption properties of the tissue it travels through. An equivalent effect will attenuate light emitted from the fluorophore. As shown in Figure 3. 2b, the excitation and emission bands of GCaMP overlap with strong (and different) absorption bands of HbO and HbR. If background absorption properties remained constant, these effects would have minimal consequence; however, through the process of neurovascular coupling, almost all neural activity should be accompanied by functional hyperemia(Hillman, 2014).

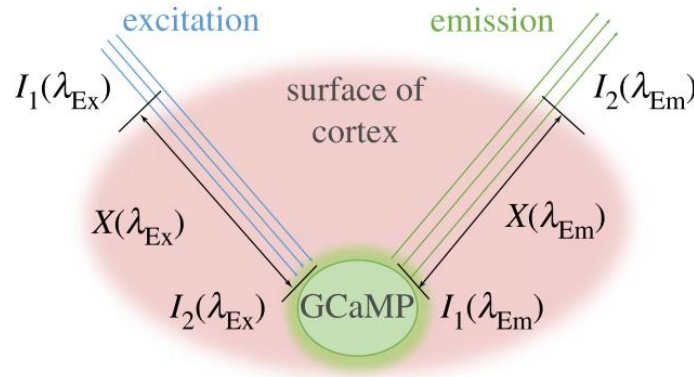


Figure 3. 3 Schematic of light paths in WFOM travelling to and from a GCaMP fluorescence interaction.

This diagram demonstrates that both excitation and emission light were influenced by brain's absorption when entering and exiting the cortical brain tissue.

As evidenced by the strongly detectable signals in reflectance WFOM, these changes in hemodynamics will thus modulate detected fluorescence, contaminating recordings of fluorescence. From Figure 3. 3 we can formulate a simple model of this effect:

$$\frac{I_2(\lambda_{Ex})}{I_1(\lambda_{Ex})} = e^{-\mu_a(\lambda_{Ex})X(\lambda_{Ex})}$$

Equation 3. 9

and

$$\frac{I_2(\lambda_{Em})}{I_1(\lambda_{Em})} = e^{-\mu_a(\lambda_{Em})X(\lambda_{Em})}$$

Equation 3. 10

where $I_1(\lambda_{Ex})$ represents the initial intensity of excitation light entering the tissue, $I_2(\lambda_x)$ represents the intensity of the excitation light reaching the fluorophore after travelling pathlength $X(\lambda_{Ex})$ through tissue with absorption coefficient $\mu_a(\lambda_{Ex})$. Similarly, $I_1(\lambda_{Em})$ represents the initial intensity of fluorescent emission light and $I_2(\lambda_{Em})$ is the intensity of emission light exciting the tissue after travelling pathlength $X(\lambda_{Em})$ through tissue with absorption coefficient $\mu_a(\lambda_{Em})$. Conversion of excitation light to fluorescence by a fluorophore is a function of σ , the fluorophore's conversion efficiency and c_f , representing either the concentration of the fluorophore or the effect (e.g. concentration of calcium) that fluorescence is proportional to. Therefore,

$$I_1(\lambda_{Em}) = I_2(\lambda_{Ex}) \cdot \sigma \cdot c_{GCaMP} .$$

Equation 3. 11

By substituting Equation 3. 9 and Equation 3. 10 into Equation 3. 11, the intensity of fluorescence emission light emerging from the tissue is given by:

$$I_2(\lambda_{Em}) = I_1(\lambda_{Ex})e^{-[\mu_a(\lambda_{Ex})X(\lambda_{Ex})+\mu_a(\lambda_{Em})X(\lambda_{Em})]} \cdot \sigma \cdot c_f$$

Equation 3. 12

It is common practice to present data as the ratio of fluorescence (or $\Delta F/F$) relative to a baseline state $F(t_0)$. This ratio cancels out the unknown distribution of initial excitation light $I_1(\lambda_{Ex})$ entering the tissue, as well as the fluorescence conversion efficiency σ , leaving,

$$\frac{F(t)}{F(t_0)} = e^{-[\Delta\mu_a(t,\lambda_{Ex})X(\lambda_{Ex})+\Delta\mu_a(t,\lambda_{Em})X(\lambda_{Em})]} \cdot \frac{c_f(t)}{c_f(t_0)}$$

Equation 3. 13

In practice, care must be taken to ensure that any camera background counts (corresponding to its ‘dark’ signal) are subtracted from $F(t)$ and $F(t_0)$ prior to ratioing to ensure cancellation of variables.

Equation 3. 13 is a very important result as it demonstrates that the effects of absorption (hemodynamic) cross-talk are multiplicative with respect to the ratiometric change in intracellular

calcium. This relationship means that using brighter GCaMPs or other fluorophores will not overcome the effects of hemodynamic cross-talk owing to their larger signal amplitude.

The result does, however highlight the dependence of cross-talk on the pathlength traveled by photons on their way to and from the fluorophore. In the case of a brain expressing strong, uniform fluorescence, most fluorescent light will be detected from superficial layers, photons that will have travelled a shorter pathlength and will therefore carry exponentially less hemodynamic contamination than in measurements of fluorophores situated in deeper layers.

3.4.2 Methods of correcting for hemodynamic cross-talk in fluorescence WFOM

To correct fluorescence WFOM data we must remove the time-varying absorption term from Equation 3. 13. We note from Equation 3. 3 that diffuse reflectance measurements give us an approximation to this absorption term, if measured at the excitation or emission wavelengths of the fluorophore. In the case of fairly broadband 530 nm (green) diffuse reflectance, which approximates the emission band of GCaMP:

$$\frac{I(t, \lambda_{Em})}{I(t_0, \lambda_{Em})} = e^{-\Delta\mu_a(t, \lambda_{Em})X_{DR}(\lambda_{Em})}$$

Equation 3. 14

The main difference is the pathlength term $X_{DR}(\lambda_{em})$, with DR denoting diffuse reflectance, which is not the same as the pathlength term $X(\lambda_{em})$ in Equation 3. 13 which corresponds to the light's path from the fluorophore to the tissue surface. Nevertheless, this formulation demonstrates that simultaneously acquiring green reflectance data (or the fluorophore's emission band) while acquiring fluorescence WFOM data will provide a valuable measure of the spatiotemporal properties of absorption changes that could confound interpretation of fluorescence changes.

Mathematically removing contributions from changes in absorption can be achieved, but will again each require approximations. We have developed 3 different methods for correction.

3.4.2.1 *Hemodynamic correction using only green diffuse reflectance (single-wavelength method)*

The first approach to hemodynamic correction is to utilize simultaneously-recorded 530 nm (green) diffuse reflectance signals. In this case, the properties of the tissue (and changes in absorption) are assumed to be the same at λ_{ex} and λ_{em} (so $\Delta\mu_a(t, \lambda_{Ex}) \approx \Delta\mu_a(t, \lambda_{Em})$) and the pathlength of the 530 nm diffuse reflectance light is assumed to be approximately the sum of the excitation and emission pathlengths ($X_{DR}(\lambda_{Em}) \approx X(\lambda_{em}) + X(\lambda_{ex})$). Contamination removal (under these approximation) can be done by simply dividing the fluorescence ratio by the reflectance ratio:

$$\frac{\frac{F(t)}{F(t_0)}}{\frac{I(t, \lambda_{Em})}{I(t_0, \lambda_{Em})}} = e^{-[\Delta\mu_a(t, \lambda_{Ex})X(\lambda_{Ex}) + \Delta\mu_a(t, \lambda_{Em})X(\lambda_{Em}) - \Delta\mu_a(t, \lambda_{Em})X_{DR}(\lambda_{Em})]} \times \frac{c_f(t)}{c_f(t_0)} \approx \frac{c_f(t)}{c_f(t_0)}$$

Equation 3. 15

3.4.2.2 *Hemodynamic correction using estimated excitation and emission attenuation (Ex-Em method)*

A more rigorous way to correct the hemodynamic confound is to correct for attenuation changes at both the excitation and emission bands of the fluorophore. In practice, acquiring reflectance images at the fluorophore's excitation band is difficult to achieve for high frame-rate imaging using a single camera, since the long-pass filter in front of the camera would need to be alternated. A second camera could be used to detect diffusely reflected excitation light, e.g. by reflecting this light from a long-pass dichroic. However, this approach adds cost, complexity and the need to

spatially and temporally register both cameras. Moreover, even these measurements cannot overcome the potential mismatch in pathlength between $X_{DR}(\lambda)$, and the pathlength of light going to and from fluorescent events.

An improvement on the single-wavelength method described above that does not require instrumentation changes is to calculate an estimate of the time-varying absorption at the fluorophore excitation wavelength using measurements at two other wavelengths. In our case, GCaMP is excited at 488 nm and diffuse reflectance is measured at 530 nm and 630 nm. Spectroscopic analysis (Equation 3. 7) can be used to infer time-varying changes in [HbO] and [HbR] for each pixel using the 530 nm and 630 nm reflectance measurements. Equation 3. 6 can then be used to calculate the effective cortical $\Delta\mu_a$ at the 488 nm excitation wavelength at the same point in time. We can therefore formulate an absorption part of the correction factor as:

$$\begin{aligned} & \Delta\mu_a(t, \lambda_{Ex})X(\lambda_{Ex}) + \Delta\mu_a(t, \lambda_{Em})X(\lambda_{Em}) \\ & \approx (\xi_{HbO}(\lambda_{Ex})\Delta c_{HbO}(t) + \xi_{HbR}(\lambda_{Ex})\Delta c_{HbR}(t))X_{est}(\lambda_{Ex}) \\ & \quad + (\xi_{HbO}(\lambda_{Em})\Delta c_{HbO}(t) + \xi_{HbR}(\lambda_{Em})\Delta c_{HbR}(t))X_{est}(\lambda_{Em}) \end{aligned}$$

Equation 3. 16

Although pathlength values X_{est} in this case must be estimated, this additional degree of freedom can help in accounting for the inherent differences in $X_{DR}(\lambda)$ and $X(\lambda)$, enabling a better approximation to the fluorescence case, and differences in absorption and pathlength properties at excitation and emission wavelengths. In practice, values of $X_{est}(\lambda_{Ex}) = .56 \text{ mm}^{-1}$ and

$X_{est}(\lambda_{Em})=0.57 \text{ mm}^{-1}$ in Thy1-GCaMP mice have been found to yield corrected GCaMP images with minimal vessel artifacts and low frequency trends resembling hemodynamic cross-talk.

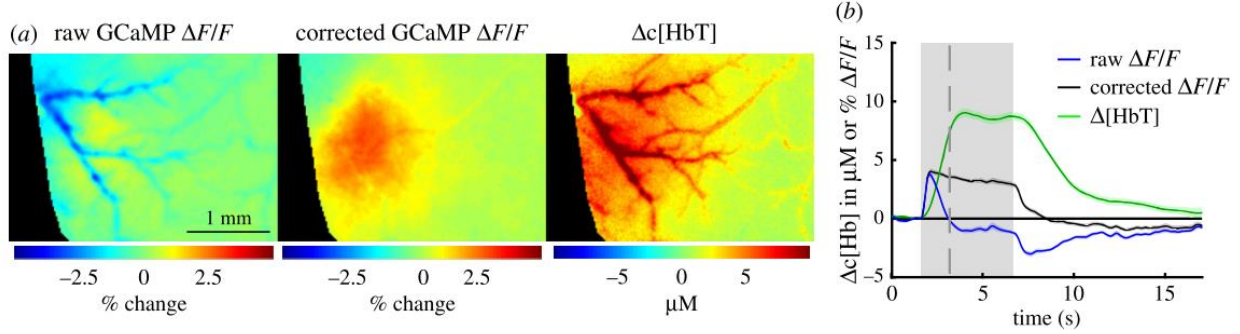


Figure 3. 4 Hemodynamic correction of WFOM GCaMP data. (a) before and after hemodynamic correction using the Ex-Em method. Maps are for 1.7 seconds after onset of a 5 second tactile whisker stimuli in an awake, behaving mouse (average of 38 trials). Corrected image shows only minor vessel artefacts, whereas original response is dominated by negative contrast corresponding to the the hemodynamic response. (b) Time-courses of the GCaMP signal before and after correction, in comparison to the $\Delta[HbT]$ hemodynamic response.

The Thy1-GCaMP6f images and time courses were corrected using the Ex-Em method and pathlength values used here were described above. Figure 3. 4 shows the data spatiotemporally before and after correction. The GCaMP image before correction shows strong vessel artifacts corresponding to absorption by hemoglobin, which are removed after correction (Figure 3. 4a). The time-course of the uncorrected GCaMP trace for a 5 second tactile whisker stimulation peaks at first and then dips below baseline as the hemodynamic response reaches its peak (Figure 3. 4b). After correction, the GCaMP signal stays positive for the duration of the stimulus as expected.

3.4.2.3 Hemodynamic correction by blind source separation

In cases where diffuse reflectance measurements cannot be acquired, or provide an uncertain or inaccurate correction of fluorescence data, it is possible in some cases to extract the hemodynamic component using blind-source separation techniques such as principal component analysis (PCA).

Such methods assume that data can be modeled as a linear sum of temporal components, and seek the largest contributors to variance within the data (which here is multiple measurements given by all of the pixels in the image). The most important consideration in this approach is to note that hemodynamic contamination of fluorescence data is multiplicative (Equation 3. 13), whereas PCA and associated methods assume that data are composed of a linear sum of separable components. As such, PCA for contamination removal should be done on the logarithm of fluorescence data, which reduces the contamination problem to a linearly added component (from Equation 3. 13)

$$\text{Ln} \left(\frac{F(t)}{F(t_0)} \right) = -[\Delta\mu_a(t, \lambda_{Ex})X(\lambda_{Ex}) + \Delta\mu_a(t, \lambda_{Em})X(\lambda_{Em})] + \text{Ln} \left(\frac{c_f(t)}{c_f(t_0)} \right)$$

Equation 3. 17

In many cases, PCA of a raw WFOM fluorescence dataset (e.g. GCaMP or FAD) will yield two primary temporal components that closely resemble the neural response and the hemodynamic confound. The spatial representation of these temporal components should be carefully examined to ensure that they also share features with expected neural and hemodynamic components (e.g. the latter showing vessel structures). Ideally, components can be compared to simultaneously acquired diffuse reflectance data to ensure a likeness. In this case, the principal component time-course found to represent hemodynamics can be multiplied by its spatial representation and subtracted from the (logarithmic) dataset.

This methodology will work optimally for short datasets capturing a single, simple event such as a response to a localized stimulus. In more complex or longer-duration data, where multiple neural events take place in different regions, components will become much more difficult to separate reliably and could remove important information from the dataset. In general, great care should be taken when using non-supervised algorithms such as PCA for this purpose, since even in the

simplest case, the order of principle components can vary (e.g. hemodynamic could be first, second or third).

Performance of PCA (and regression techniques) can be improved with reduction of noise in the data, for example by registering motion in each trial, averaging across trials and low pass filtering (at around 3-5Hz) to remove physiological noises such as heart rate and breathing rate.

3.5 Verification of fluorescence WFOM with electrophysiology

Changes in GCaMP fluorescence have been widely shown to correspond to neural activity in studies using two-photon microscopy (Chen et al., 2012; Chen et al., 2014; Issa et al., 2014) and the kinetics of GCaMP3 and GCaMP6f are similar (Akerboom et al., 2013). High-speed wide-field imaging of GCaMP fluorescence provides a depth-integrated, ensemble measurement of neural events over a much larger field of view compared to two-photon microscopy (Issa et al., 2014; Vanni and Murphy, 2014; Kozberg et al., 2016). However, an essential consideration when using wide-field GCaMP imaging is the spectral overlap between hemoglobin absorption and GCaMP excitation and emission bands. Simultaneous measurement of cortical hemodynamics and GCaMP fluorescence in our experiments enabled a correction for these absorption effects as described before.

To verify whether hemodynamics-corrected GCaMP fluorescence signals reflect underlying neural activity, GCaMP fluorescence measurements were compared to simultaneously recorded multi-unit activity (MUA) in anesthetized animals (n=9 mice) at the same cortical locations (Figure 3. 5a). Data were acquired in a urethane anesthetized Thy1-GCaMP3 mice during resting state and 8s duration, 3Hz electrical hindpaw stimulation. Electrophysiological data were spike-sorted to

yield multi-unit activity (MUA). Raw fluorescence data were corrected using the single-wavelength method.

A gamma-variate function was chosen as the kernel to mimic the fast onset and gradual decay kinetics of neural calcium and the kinetics of GCaMP fluorescence in response to intracellular calcium changes (Figure 3. 5b). As expected from the spectral overlap of hemoglobin and GCaMP excitation and emission bands (Figure 3. 5b), correction for the contaminating effects of hemodynamics was applied to raw GCaMP data. Figure 3. 5d shows a spontaneous MUA recording, along with the time-course of hemoglobin-corrected GCaMP fluorescence from the same region, and a prediction of GCaMP fluorescence based on the convolution of MUA with a best-fit gamma function (correlation coefficient = 0.86). Figure 3. 5c compares the quality of the fit between predicted GCaMP and measured data, before and after correction, showing an average correlation coefficient of 0.72 ± 0.01 for spontaneous activity and 0.70 ± 0.01 for stimulus-evoked activity after correction. The gamma function parameters describing the best-fit GCaMP fluorescence kernel also agree well with GCaMP characterization results using two-photon and cell-attached recording (Chen et al., 2012) (time to peak = 0.18 ± 0.01 s and width = 0.35 ± 0.02 s for spontaneous activity). This strong agreement between recorded GCaMP fluorescence and MUA-predicted fluorescence both confirms that hemodynamic corrected data are a more precise representation of neural data than raw fluorescence, while also demonstrating that wide-field GCaMP signals in Thy1-GCaMP mice provides an accurate representation of the integrated spiking activity of excitatory neurons.

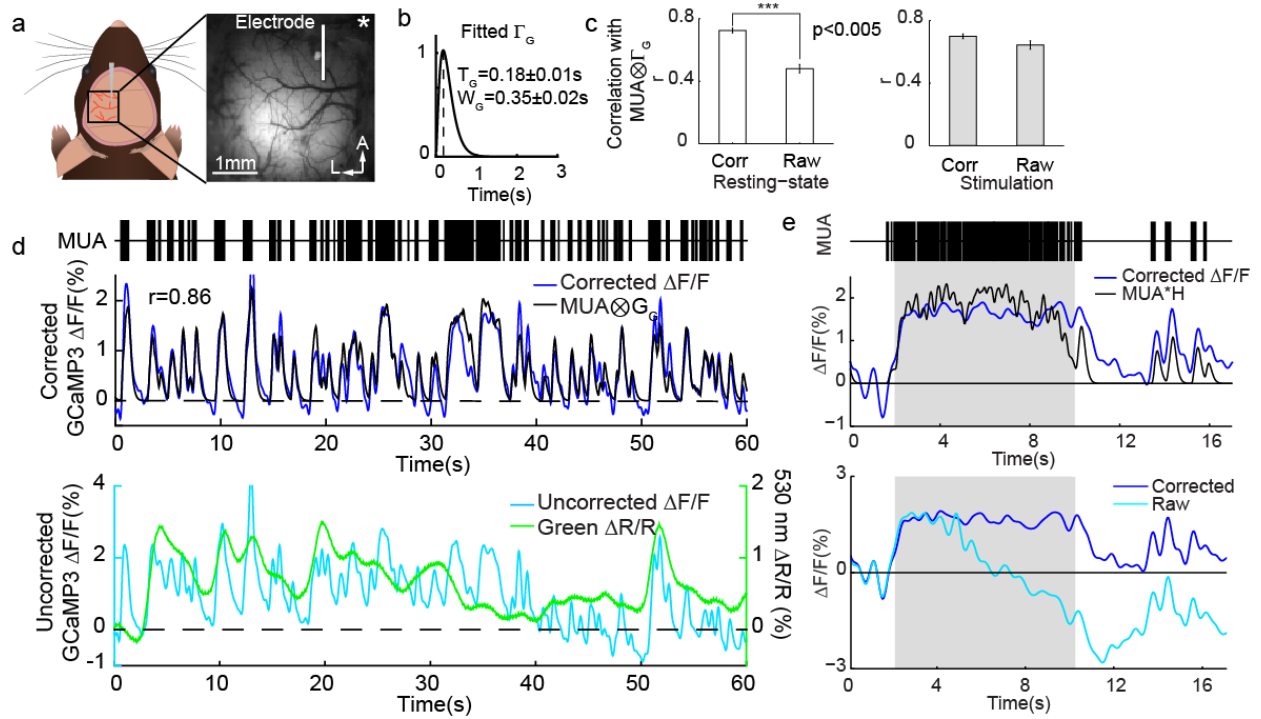


Figure 3. 5 Validating wide-field GCaMP fluorescence with electrophysiology in presence and absence of stimulation. (a) Field of view for simultaneous imaging and micro-electrode recording in the somatosensory hind-paw region (urethane anesthetized). Star indicates bregma. (b) Average best-fit gamma-variate function Γ_G fitting convolved MUA to hemodynamics-corrected Thy1-GCaMP3 fluorescence at resting state. (c) Hemodynamic correction of spontaneous GCaMP fluorescence yielded significantly higher correlations with convolved MUA compared to raw fluorescence. (d) Example of resting state MUA at the micro-electrode, and comparison of corrected GCaMP $\Delta F/F$ and the best-fit of MUA convolved with the gamma function. Uncorrected GCaMP $\Delta F/F$ accompanied with concurrent change in green reflectance, demonstrating the effect of hemodynamic cross-talk in the fluorescence channel. (e) Example of MUA, corrected and uncorrected GCaMP $\Delta F/F$ driven by a 4s hind paw electric stimulation (shaded region).

Chapter 4

Assessing neurovascular coupling at resting state

4.1 Introduction

Functional magnetic resonance imaging (fMRI) measures local changes in [HbR] as a surrogate for neural activity. In stimulus-evoked studies, the positive fMRI blood oxygen level dependent (BOLD) signal corresponds to a *decrease* in [HbR] caused by a local increase in blood flow leading to over-oxygenation of the region. However, a growing number of studies are utilizing resting-state functional connectivity fMRI (fc-fMRI) in which spontaneous fluctuations in the BOLD signal are recorded in the absence of a task (Raichle et al., 2001). Spatiotemporal correlations in these hemodynamic signals across the brain have been found to be bilaterally symmetric and synchronized in distant brain regions. This synchrony is interpreted as representing the connectivity of intrinsic neural networks (Biswal et al., 1995; Beckmann et al., 2005; De Luca et al., 2006; Tomasi and Volkow, 2012). Many studies have identified changes in these resting-state networks during brain development (Salzwedel et al., 2015; Smyser and Neil, 2015) and in neurological and even psychological disorders (Anand et al., 2005; Zhou et al., 2007; Ekstrom, 2010). However, understanding the meaning of both normal and altered functional connectivity

networks requires a clearer picture of the neural activity underlying the hemodynamic fluctuations detected by resting-state fMRI.

Prior studies using electrophysiology (Liu et al., 2013), electrocorticography (Nir et al., 2008) and magnetoencephalography (Brookes et al., 2011) have observed synchronous patterns of neural activity in distant, often bilateral brain regions, consistent with a neural representation of functional connectivity networks. Studies combining acquisition of electrophysiology and fMRI data in both anesthetized (Shmuel and Leopold, 2008; Magri et al., 2012) and awake (Scholvinck et al., 2010) primates have also found correlations between resting-state BOLD signals and local field potentials (LFPs). However, the highest correlations reported to date are around 0.3 for gamma band powers between 40-100 Hz. Questions thus remain regarding the extent to which resting-state hemodynamics correspond to neural activity, the kinds of neural activity represented by resting-state fMRI signals, and whether additional hemodynamic components contribute to and confound fc-MRI analysis.

In this chapter, simultaneous wide-field optical imaging of hemodynamics and neural activity was performed in awake and anesthetized mice expressing the genetically encoded calcium-sensitive fluorophore GCaMP in excitatory neurons in layers 2-3 and 5. This experimental approach enabled high-speed imaging across the entire superficial cortex, depicting both spontaneous neural activity and hemodynamics in parallel (Kozberg et al., 2016; Ma et al., 2016a). Single-site electrophysiology with simultaneous GCaMP imaging was used to confirm that recorded fluorescence, after hemodynamic correction, represents local multi-unit activity (MUA). The causal relationship between spontaneous activity in excitatory neurons and resting-state hemodynamics was then assessed using both deconvolution and a gamma-variate fit based convolution model. This analysis demonstrates that resting-state hemodynamics in the awake brain

can be well-predicted by spontaneous neural activity over the entire superficial cortex, representing a summation of successive increases in blood flow coupled to spontaneous neural events. Urethane anesthesia resulted in slower coupling, and in some cases introduced slow trends in hemodynamics that were not accounted for by Thy1-GCaMP signals. The patterns of spontaneous neural activity founds to be driving resting-state hemodynamics exhibit strong bilateral synchrony in both awake and anesthetized states, in patterns consistent with resting-state functional connectivity networks.

4.2 Materials and Methods

4.2.1 Animal preparation

For mice in the anesthetized group, six adult Thy1-GCaMP3 mice (Jackson Laboratory, B6;CBA-Tg(Thy1-GCaMP3)6Gfng/J) were anesthetized with 1.5mg/kg urethane administered intraperitoneally, accompanied with 0.5 mg/kg Glycopyrrolate. The animal's core body temperature was monitored and maintained at $36.5 \pm 0.5^{\circ}\text{C}$ using a homoeothermic temperature controller (FHC 40-90-8D). After the mouse was securely positioned in a stereotaxic frame (Kopf), the scalp was retracted and the skull between the coronal and lambdoid sutures was thinned to translucency. Wide-field optical mapping (WFOM) data was then acquired. The animal's heart rate, breathing rate and arterial oxygen saturation throughout both surgery and imaging were monitored with a rodent pulse oximeter (Kent Scientific MouseSTAT). Resting-state trials were acquired for periods of 180 seconds and no stimulation was given during these recordings. Electrophysiology methods are described below.

For awake studies, six adult Thy1-GCaMP6f mice (Jackson Laboratory, C57BL/6J-Tg(Thy1-GCaMP6f)GP5.17Dkim/J) were handled and acclimated to a saucer-wheel treadmill. Animals

were then anesthetized with isoflurane, their scalp was retracted and skull thinned over the entire accessible superficial cortex. The thinned-skull was then protected with a layer of cyanoacrylate glue and a custom acrylic headpiece surrounding the craniotomy region was glued onto the skull. Following this preparatory surgery, mice were recovered, receiving buprenorphine analgesic for 72-hour post-operatively. A removable layer of Kwik-Sil (WPI) silicone is applied to the cranial window between imaging sessions to provide mechanical protection. One week after window implantation, the animals were imaged in sessions lasting up to two hours with at least three days between each session. For each imaging session, the animal was lightly anesthetized with isoflurane during initial head fixation, and was then fully recovered before imaging began.

Mice were allowed to stand, walk or run freely on a customized transparent saucer-wheel treadmill during imaging. A camera positioned underneath the animal tracked the treadmill's rotation and hence the animal's movement in synchrony with imaging of the brain. Up to 40 repeated 60 second resting-state trials were acquired during each imaging session. Trials with at least a continuous 30s of the animal not moving were identified and only these non-running epochs were included in 'resting-state' analysis. Awake animals were trained with acclimatization, handling and were given treats after imaging. No food or water deprivation was used.

4.2.2 Electrophysiology acquisition and analysis

Simultaneous optical imaging and electrophysiology recordings was performed on urethane-anesthetized Thy1-GCaMP animals. In half of the animals, a piece of skull (2x2mm) overlaying the somatosensory cortex was carefully removed (e.g. Figure 4. 7b). In other half, a unilateral thinned-skull craniotomy was prepared between the coronal and lambdoid sutures, and a small (<200 microns) piece of skull overlying the responding region was removed to allow electrode

insertion while imaging was performed through surrounding thinned skull (e.g. Figure 4. 7a and Figure 4. 7c). WFOM imaging during hindlimb stimulation was performed to confirm the location of the somatosensory cortex. A well was then built up around the cranial window with dental acrylic (Henry Schein) and filled with artificial cerebrospinal fluid (ACSF: 124mM NaCl, 5mM KCl, 4.1mM CaCl₂, 10mM C₆H₁₂O₆, 2.8mM MgCl, 10mM C₈H₁₂N₂O₄S). A tungsten single channel microelectrode (0.5M Ω , A-M systems) was then advanced into the somatosensory hindpaw region to a depth of 300~600 μ m by a micromanipulator that was mounted on the stereotaxic frame. The ACSF fluid in the well covering the cortical window served as the ground for the electrophysiological recordings. The animal's heart rate, breathing rate and arterial oxygen saturation throughout both surgery and imaging were monitored with a rodent pulse oximeter (Kent Scientific MouseSTAT).

A differential AC Amplifier (Model 1700, A-M system) was used with 1000 x gain, and the signal was then sampled at 25 kHz (Micro 1401, CED). The high frequency band (500 - 3000Hz) of the recorded signal was analyzed using spike detection in the Spike2 software (CED). Specifically, the high frequency signal was thresholded by 2.5 times the standard deviation, and then detected spikes went through template matching to make sure at least 20 repetitions of similar spikes appeared within 60s. The sorted spikes were then combined together and treated equally as MUA. The timestamps of detected MUAs were then loaded in MATLAB (Mathworks) for further analysis.

4.2.3 Optical hemodynamic and GCaMP fluorescence imaging

Simultaneous wide-field GCaMP fluorescence and cortical hemodynamics were imaged using wide-field optical mapping (WFOM) as described in Chapter 3. WFOM can map the dynamics of

[HbO] and [HbR] based on their oxygen-dependent optical absorption spectra. Multi-spectral reflectance data is acquired interlaced with fluorescence data by using a camera configured to acquire images in synchrony with three strobing light emitting diodes (LEDs). Reflectance images were acquired during periods of green LED light illumination at 530nm (M530L2, Thorlabs with 534/43nm filter - NT67031, Edmund Optics) or red LED light illumination at 630nm (M625L2, Thorlabs), while a 500nm long-pass filter (FF01-496/LP-25, Semrock) mounted in front of the camera enabled imaging of GCaMP fluorescence during periods of illumination with blue LED light with a wavelength around 490nm (M490L2, Thorlabs with 460/60nm filter - FB460-60, Thorlabs).

For anesthetized animals a CCD camera (Dalsa 1M60) was operated at 45 or 75 frames per second (equivalent 3-color frame rate in each channel is 15 or 25 Hz) with 6-8 ms exposure and 8x8 binning (128 x 128 pixels), mounted with a VZM300 optical zoom lens (Edmund Optics) with operating magnification ranged from 2.5x to 3x (equivalent field of view: 4.1mm x 4.1mm). Awake animals were imaged using an EMCCD camera (ANDOR Ixon 897) at 31.22 Hz (equivalent frame rate per spectral channel: 10.41 Hz) with 5 ms exposure and no binning (512 x 512 pixels, equivalent field of view: 8.2mm x 8.2 mm), mounted with an AF Micro-NIKKOR 60 mm lens (Nikon).

Green and red reflectance data were converted to changes in HbO and HbR concentrations using the modified Beer Lambert law with Monte-Carlo derived wavelength-dependent pathlength factors (Hillman, 2007; Chen et al., 2014; Ma et al., 2016b). Interspersed fluorescence images of genetically encoded GCaMP were hemodynamic-corrected and converted into $\Delta F/F$, where ΔF is the mean-subtracted raw fluorescence signal and F is the mean of the entire time course.

4.2.4 Imaging data pre-conditioning and statistics

For pixel-wise HRF fitting, 512x512 imaging data from awake animals were downsampled to 128x128 to reduce computation time. Anesthetized data with a unilateral field of view were analyzed at their native 128x128 resolution. Anesthetized data with a bilateral field of view were analyzed downsampled to 64x64 resolution.

Unless otherwise noted, non-running awake resting-state epochs ranging from 30 – 60s in duration were temporally band-pass filtered at 0.02 Hz-2Hz (both fluorescence and hemodynamic signals), with a 2Hz low-pass chosen to reduce physiological noise such as heart rate, and the 0.02 Hz high-pass to detrend the baseline. Analysis was repeated with a 0.04 Hz high pass filtered as noted and shown in Figure 4. 16.

In most anesthetized results shown, fluorescence and hemodynamic signals were temporally band-pass filtered at 0.04 – 2 Hz unless otherwise noted (e.g **Error! Reference source not found.**). A .04 Hz high-pass filter was found to reduce the influence of slow hemodynamic trends as described in the text. All the filtering was performed using a zero-phase filter (filtfilt) in MATLAB (Mathworks).

4.2.5 GCaMP fluorescence correction for hemodynamic cross-talk

As described in the previous chapter, it is important to note that both the excitation and emission wavelengths of GCaMP fluorescence are absorbed by HbO and HbR, whose concentrations are known to be varying substantially over time. If this contamination is not corrected, it could influence analysis of the coupling relationship between neural activity and hemodynamics. In here, approximate correction of GCaMP signals is achieved via Ex-Em method described in Chapter 3.

Simply put, reflectance measurements were used to derive an estimate of $\mu_{aEx}(t)$ where $Ex \sim 490$ nm. For every pixel, values of $\Delta [HbO]$ and $\Delta [HbR]$ are calculated, these can be used to estimate $\mu_{a490nm}(t)$ and the known extinction coefficients of HbO and HbR. An improved estimate of $\mu_{aEm}(t)$ for the emission band of GCaMP can be calculated in the same way. These values can then be used in Equation 3. 13, with estimates of the pathlength factors x_{Ex} and x_{Em} chosen ($x_{Ex}=0.56 \text{ mm}^{-1}$, $x_{Em}=0.57 \text{ mm}^{-1}$ in this case) as constants across the image and dataset) that minimize the appearance of vessel artifacts in the hemoglobin-corrected GCaMP images.

4.2.6 Optimizing gamma-variate functions in fits of GCaMP response and HRF

A gamma-variate function was chosen as the kernel to convolve with the timestamp of MUA to predict GCaMP fluorescence (Γ_G), and to convolve with corrected GCaMP fluorescence to predict hemodynamics (Γ_H). The function is defined by three parameters A , T and W where:

$$\Gamma(t) = A \cdot \left(\frac{t}{T}\right)^\alpha \cdot e^{-\frac{t-T}{\beta}}$$

Equation 4. 1

where $\alpha = \left(\frac{T}{W}\right)^2 * 8 * \log(2)$, $\beta = \frac{W^2}{T} * 8 * \log(2)$. A represents the maximum amplitude, T is the time delay of the peak and W is full width at half maximum. The total duration of the kernel convolved with the data was set to be 3s for Γ_G (MUA to GCaMP fluorescence kernel) and 30s for Γ_H (HRF). To determine these function parameters, optimal values were calculated using the constrained multi-variable optimization function in MATLAB (fminsearchbnd, MATLAB File Exchange), minimizing the sum square difference between the predicted and original signal. All the parameters were constrained to be positive real numbers.

4.2.7 Estimating HRF by least-square deconvolution

Another method used to estimate the HRF from GCaMP fluorescence and cortical hemodynamics is least-square deconvolution. For a linear system the convolution can be expressed as

$$\begin{bmatrix} y_1 \\ y_2 \\ y_3 \\ \vdots \\ y_t \end{bmatrix} = \begin{bmatrix} x_1 & 0 & 0 & \dots & 0 \\ x_2 & x_1 & 0 & \dots & 0 \\ x_3 & x_2 & x_1 & \dots & 0 \\ \vdots & \vdots & \vdots & \ddots & \vdots \\ x_t & x_{t-1} & x_{t-2} & \dots & x_{t-n} \end{bmatrix} \begin{bmatrix} h_1 \\ h_2 \\ h_3 \\ \vdots \\ h_n \end{bmatrix}$$

Equation 4. 2

or $y=X*h$, where X is the system's input in matrix format which is changes in fluorescence, y is the system's output with the length of observations (t) which is the $\Delta[HbT]$ and h is the system's impulse function which is the HRF in the context of neurovascular coupling and its length n is assigned by the user. In our analysis, n was assigned to be half the length of the trial ($t/2$) or 30s if the half-length is bigger than that.

Instead of using the direct solution to this linear system

$$h = X \backslash y$$

Equation 4. 3

a diagonal loading least square deconvolution method was used to solve for the HRF to avoid the problem of rank deficiency. This least square method minimize cost function

$$J(x) = \|y - Xh\|_2^2 + \lambda \|h\|_2^2$$

Equation 4. 4

Which is the weighted sum of the energy of the error ($\|y - Xh\|_2^2$) and the solution ($\|h\|_2^2$). By setting the derivative of the cost function to zero, the solution is given by

$$h = (X^T X + \lambda I)^{-1} X^T y$$

Equation 4. 5

The constant weight λ was chosen to be 0.01 throughout our analysis. The first 10s of the deconvolved function was used as HRF. (Reference: Ivan Selesnick, Least Squares with Examples in Signal Processing, <https://cnx.org/contents/XRPKcVgh@1/Least-Squares-with-Examples-in>). The deconvolution was operated on each pixel individually.

4.2.8 Spike-triggered averaging

As an independent method for analysis of neurovascular coupling, spike-triggered averaging can demonstrate the averaged effect of neural events on a variable without involving estimation of HRFs (Bruyns-Haylett et al., 2013). Spike events were defined as local maxima in the uncorrected $\Delta F/F$ time courses from somatosensory cortex and identified using the ‘findpeaks’ function in MATLAB. A local peak was defined as one 0.3% (percentage as the unit for $\Delta F/F$) higher than an adjacent valley and with a full width half max of at least 0.3s. The changes in uncorrected GCaMP fluorescence, $\Delta[\text{HbT}]$, $\Delta[\text{HbR}]$ and $\Delta[\text{HbO}]$ 3s before to 10s after each identified peak event were averaged across all trials within each animal (for awake and anesthetized conditions separately). Plots show the average spike-triggered averages among animals. Shaded regions represent the standard error between animals.

4.2.9 Frequency-dependent cross-correlation analysis

Cross-correlation analysis between Thy1-GCaMP6f and $\Delta[\text{HbT}]$ measurements was performed as a function of temporal frequency. To ensure consistent sampling in the frequency domain, only the last 30s in each awake resting-state epoch was used in this analysis. Unfiltered $\Delta[\text{HbT}]$ and corrected Thy1-GCaMP6f fluorescence data from the somatosensory region of all awake resting-state trials were band-pass filtered with a 0.35 Hz sliding window in the frequency domain from 0.035 to 5.2 Hz with an increment of 0.035 Hz. Band pass filtered neural and hemodynamics were then cross-correlated. The peak amplitude of the cross-correlation within a -5 to 5 s window around 0 shift was determined, along with its phase delay for each epoch. Plots of the peak cross-correlation coefficient and phase delay as a function of frequency were then averaged within animals. Plots show the mean \pm SEM between animals, with frequencies denoting the start of the frequency window. The peak correlation frequency was determined from the grand average. The phase delay was calculated as the mean and standard deviation of phase delays between animals at the peak correlation frequency.

4.2.10 Statistical analysis

Goodness of fit between measured and modeled $\Delta[\text{HbT}]$ data were evaluated using Pearson's correlation coefficients. Statistical analyses were performed using a two-tailed Student's t test (all pair-wise comparisons are specified). All the results are expressed in the form mean \pm SEM, unless specified. All data analyses were performed using MATLAB (Mathworks).

4.3 Bilaterally symmetric patterns observed in resting-state neural and hemodynamic activity

To visualize both neural and hemodynamic activity, awake (Thy1-GCaMP6f) and urethane-anesthetized (Thy1-GCaMP3) mice were imaged using simultaneous fluorescence and multi-spectral wide-field optical mapping (WFOM) through a cranial window (Bouchard et al., 2009; Ma et al., 2016a). Cyan light (490 nm) provided excitation of GCaMP fluorescence, while green (530 nm) and red (630 nm) reflectance signals were converted into images of changes in oxy-, deoxy- and total hemoglobin concentrations ($\Delta[\text{HbO}]$, $\Delta[\text{HbR}]$ and $\Delta[\text{HbT}] = \Delta[\text{HbO}] + \Delta[\text{HbR}]$). Hemodynamic signals were also used to correct recorded GCaMP fluorescence for the time-varying effects of hemoglobin absorption. Awake animals were head-fixed but positioned on a saucer-wheel and were free to run during imaging. The motion of the wheel was monitored throughout imaging using a webcam synchronized with image acquisition. All periods of running were removed, and ‘resting-state’ epochs were defined as periods of at least 30 seconds of continuous rest.

Figure 4. 1a shows a sequence of the spatial patterns of spontaneous neural activity recorded in the awake mouse brain during a period of rest using wide-field GCaMP6f imaging (after hemodynamic correction), along with concurrent maps of hemodynamics given by $\Delta[\text{HbT}]$. The patterns of spontaneous neural activity evolve rapidly, exhibiting synchronization between regions and bilateral symmetry. Changes in $[\text{HbT}]$ occur at a much slower pace, but can be seen to resemble the same spatial pattern at $t = 24.1$ seconds as the neural pattern at 25.3 seconds (corresponding patterns marked by A, B and C). Figure 4. 1c shows time-courses of corrected GCaMP fluorescence with concurrent changes in $[\text{HbT}]$, $[\text{HbO}]$ and $[\text{HbR}]$ for the two regions indicated in Figure 4. 1b during the same awake, resting-state trial. Increased $[\text{HbT}]$ and $[\text{HbO}]$

and decreased [HbR] can be seen to occur following peaks in the GCaMP signal (black arrows), consistent with stimulus-evoked functional hyperemia (Sirotin and Das, 2009). Although the need to correct GCaMP fluorescence measurements for hemodynamic contamination is a potential confound, these time-sequences underscore that patterns of neural activity are detected many frames before hemodynamic changes, yet are clearly coupled to spatially correlated hemodynamics.

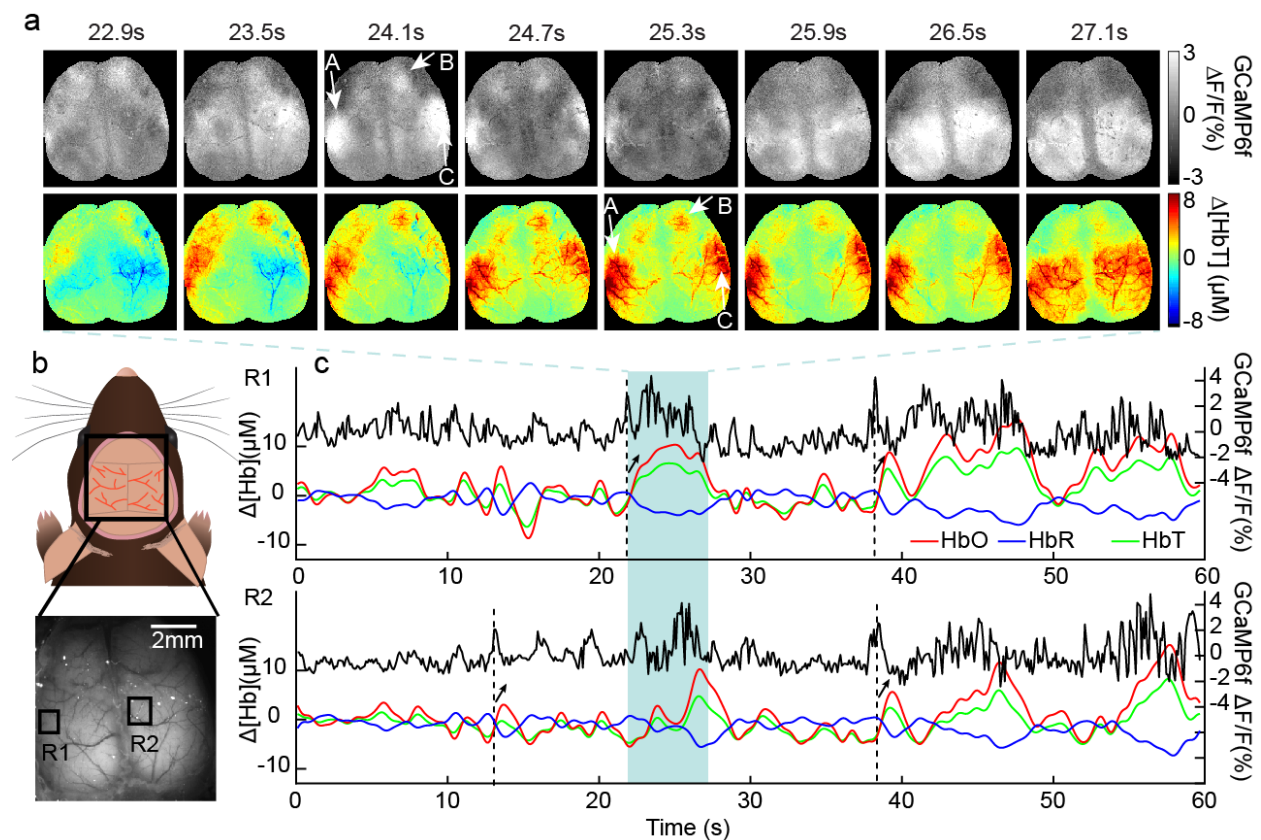


Figure 4. 1 Wide-field imaging of GCaMP fluorescence and hemodynamic activity in the awake mouse brain.

(a) Consecutive maps of recorded GCaMP6f $\Delta F/F$ (top) showing spontaneous synchronized events symmetric across the bilaterally exposed cortex of an awake mouse and concurrent maps of hemodynamics (bottom, given by $\Delta[HbT]$) showing similar spatial patterns (A,B,C) but with a time delay. (b) Schematic and example of chronic bilateral thinned-skull window imaged in awake animals. Gray scale image shows raw fluorescence, star indicates bregma. (c) Time-courses of simultaneously acquired resting-state GCaMP6f $\Delta F/F$ (black), $\Delta[HbO]$ (red), $\Delta[HbR]$ (blue) and $\Delta[HbT]$

(green) are shown from the two regions marked in b. Dotted lines indicate neural events with arrows indicating corresponding hyperemias given by increased $\Delta[\text{HbO}]$, $\Delta[\text{HbT}]$ and decreased $\Delta[\text{HbR}]$.

Changes in $[\text{HbR}]$ are the primary contributor to the fMRI BOLD signal (Hillman, 2014). However, $[\text{HbR}]$ can be affected by changes in oxygen consumption, blood flow and blood volume, making it ambiguous to interpret. Conversely, $\Delta[\text{HbT}]$ represents a change in the concentration of blood in tissue, independent of local changes in oxygenation and thus provides a more pure measure of a physical change in vascular tone. Calculating the average peak amplitude of the cross correlation between $\Delta[\text{HbR}]$ and $\Delta[\text{HbT}]$ across anesthetized resting-state trials and mice (allowing for relative temporal delays), we find a -0.86 ± 0.10 ($n=6$ mice) correlation between $\Delta[\text{HbT}]$ and $\Delta[\text{HbR}]$. This result suggests that, as in stimulus-evoked fMRI, the driving component of changes in $[\text{HbR}]$ in the resting-state are evoked increases in local blood flow causing increased oxygenation (leading to positive BOLD (Sirotin and Das, 2009)) rather than modulations in oxygen consumption. Analysis here thus focuses on $[\text{HbT}]$ dynamics rather than $[\text{HbR}]$, in order to examine physical coupling of vascular modulations to neural activity.

4.4 Analysis of spatiotemporal neurovascular coupling in awake animal

Although a qualitative relationship between neural activity and hemodynamics can be appreciated from the data shown in Figure 4. 1, a more quantitative approach is needed to evaluate the properties of resting-state neurovascular coupling. A commonly used approach is to assume a linear model of neurovascular coupling, such that hemodynamics would correspond to the convolution of neural activity and a gamma-shaped hemodynamic response function (HRF)

(Boynton et al., 1996; Cardoso et al., 2012). Here, three independent strategies were developed to test this linear relationship: gamma-variate fitting, deconvolution and spike-triggered averaging.

Gamma-variate fitting analysis has been performed previously to analyze stimulus-evoked neurovascular coupling data (Madsen, 1992; Martin et al., 2006; Cardoso et al., 2012). Here, a three-parameter gamma-variate function was used to approximate an HRF. Fit parameters were optimized to yield the best-fit (minimized least-squares error) to measured hemodynamic data after convolution with corrected GCaMP-based recordings of neural activity (Heeger and Ress, 2002; Cardoso et al., 2012). The resulting best-fit HRF at each pixel was then convolved with the GCaMP time-course of that pixel and compared to measured $\Delta[\text{HbT}]$ at the same position using a Pearson's correlation coefficient to quantify goodness of fit. Unlike correlation-based analysis of LFP band power (Murayama et al., 2010; Pan et al., 2011; Magri et al., 2012) this method assumes a clear linear model of neurovascular coupling where excitatory activity is expected to generate a proportional, localized increase in $[\text{HbT}]$ (local hyperemia).

Deconvolution is an alternative approach that similarly assumes a linear convolved model of neurovascular coupling but does not impose constraints on the temporal shape of the convolved HRF. A diagonal loading method was used to deconvolve each pixel of $\Delta[\text{HbT}]$ data from corrected GCaMP data, yielding a similar spatially-resolved HRF for each dataset. The resulting HRF at each pixel was then temporally cropped and reconvolved with the pixel's GCaMP time-course, and compared to the pixel's measured $\Delta[\text{HbT}]$ using Pearson's correlation.

Spike-triggered averaging (Magri et al., 2012; Bruyns-Haylett et al., 2013) was also used as an independent approach to demonstrate the form of coupling between resting-state neural events and hemodynamic activity independent of GCaMP corrections and model dependencies as described further below.

4.4.1 Model-based analysis of awake, resting-state data

Figure 4. 2 shows fitting results for awake, resting-state mice. For two cortical locations within the same trial, traces of corrected GCaMP are plotted along with measured $\Delta[\text{HbT}]$, gamma-variate fit $\Delta[\text{HbT}]$ and deconvolution-predicted $\Delta[\text{HbT}]$. Before fitting, both GCaMP6 and $\Delta[\text{HbT}]$ data were pre-conditioned using a 0.02 Hz high pass filter (HPF) to remove slow drifts, as well as a 2Hz low pass filter (LPF) to reduce physiological noise (although all corrected GCaMP traces are shown without low pass filtering). Both fits show good agreement with measured $\Delta[\text{HbT}]$ and resemble the characteristic fluctuations of resting-state hemodynamics. HRFs derived using both methods exhibit similar temporal shapes and correlation coefficients (Figure 4. 2c).

Performing fitting analysis for each pixel individually permits HRFs to vary spatially over the field of view. Figure 4. 2d shows a map of the Pearson's correlation coefficient between measured and gamma-variate modeled $\Delta[\text{HbT}]$, and maps of optimized fit parameters (amplitude A_H , peak time T_H and width W_H) from the same trial shown in Figure 4. 2b. Fit parameters vary somewhat across the cortex, with A_H tracing the distinct shapes of the cortical arteries reflecting the higher amplitude contribution of surface vessels to WFOM hemodynamics (Hillman, 2007; Ma et al., 2016b).

Figure 4. 2e shows a sequence of images from the same trial including corrected GCaMP, measured $\Delta[\text{HbT}]$, the best-fit (gamma-variate) prediction of $\Delta[\text{HbT}]$ and fit residuals over the full field of view. Even though the spatial patterns of neural activity have a much faster pace compared to the observed hemodynamics, convolution of the GCaMP signal with fitted HRFs yields a predicted $\Delta[\text{HbT}]$ that is a close match to the measured $\Delta[\text{HbT}]$ dynamics. Both increases and decreases in $\Delta[\text{HbT}]$ are accurately modeled from the observed increases and decreases in excitatory neural activity.

Equivalent analysis was performed for all non-running epochs lasting > 30 s from 6 awake mice, each imaged multiple times on different days (two recording days were removed owing to excessive motion artifacts). To summarize fit quality across all trials and all mice, a region over the somatosensory cortex was binned to 16×16 pixels (equivalent to a 1 mm^2 region) and analyzed using both deconvolution and gamma-variate fitting. Figure 4. 2f shows average Pearson's correlation coefficients and their standard deviations over these regions for individual trials in chronological order for the deconvolution model. The overall distribution of averaged correlation

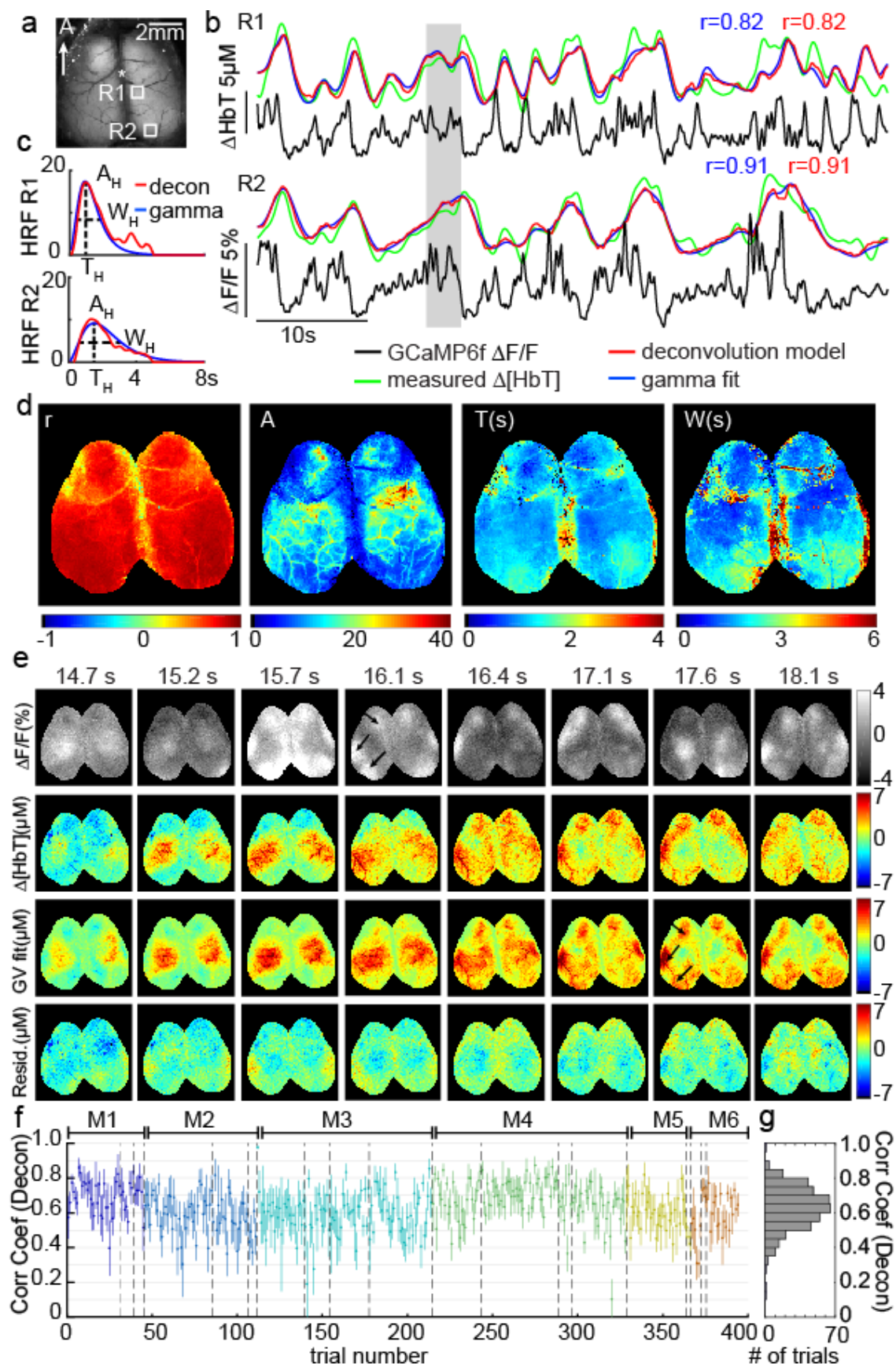


Figure 4. 2 Spatiotemporal modeling of hemodynamics from wide-field Thy1-GCaMP6f recordings in the awake, resting brain. Field of view under blue illumination, (b) 60s examples of awake, resting-state GCaMP6f $\Delta F/F$ time-courses (after hemodynamic correction) with simultaneously recorded $\Delta[\text{HbT}]$ from the two regions indicated in (a) (same trial). Red and blue traces show the results of convolving corrected GCaMP fluorescence with hemodynamic response functions (HRFs) derived via deconvolution or gamma-variate fitting respectively (c) Deconvolved HRF and best-fit gamma-variate HRF for the time-series shown in (b) illustrating the amplitude A_H , time of peak as T_H and width at half-maximum as W_H gamma-fit parameters. (d) Left: map of gamma-variate fit Pearson's correlation coefficients (r) per pixel, Right: Gamma-variate HRF best-fit parameters (A_H , T_H and W_H) for the trial shown in (b). (e) Example epoch, top row: corrected Thy1-GCaMP6f $\Delta F/F$, 2nd row: $\Delta[\text{HbT}]$, 3rd row: gamma-variate model fit to $\Delta[\text{HbT}]$ based on the GCaMP signal, bottom row: fit residuals. Arrows highlight specific neural events that are mirrored in later hemodynamics. Supplemental Movies S2 and S3 show the full time-sequence for this trial for gamma-variate and deconvolution fits respectively. (f) Plot of mean average and standard deviation (over 1 mm² region over S1) Pearson's correlation coefficients for the deconvolution model for all resting-state epochs in all 6 mice (histogram right shows overall distribution for all trials). Values are chronological with dotted lines indicating different days and colors indicating different mice M1-M6.

coefficients across trials, days and animals is shown in Figure 4. 2g. Correlation coefficients ranged from 0.3 to 0.9, with an average across all animals and trials of 0.63 ± 0.02 over 6 animals (0.53 ± 0.03 for gamma-variate fitting, where the temporal shape of the HRF is more constrained).

4.4.2 Frequency-dependence of neurovascular correlations

Mathematically, convolution of a broadband signal with a gamma function will act primarily as a low pass filter, integrating faster activity into a moving average over time. The fits above thus suggest that a low frequency component of resting state neural activity accounts for resting state hemodynamic fluctuations. The frequency-dependence of the cross-correlation between (unfiltered) corrected GCaMP and $[\text{HbT}]$ data was assessed by band-pass filtering (BPF) both datasets with a 0.35 Hz sliding frequency-domain window from 0.035 to 5.2 Hz with an increment

of 0.035 Hz. The peak amplitude and phase delay of the cross-correlation between neural activity and hemodynamics for each frequency band was calculated for all awake resting state epochs in all animals. Peak correlations were found at a frequency of around 0.21 Hz, decreasing both towards 0 Hz and above 0.4 Hz (Figure 4. 3a). The average temporal delay of the cross correlation at 0.21 Hz was 0.86 ± 0.05 s across all animals representing the phase shift between neural activity and [HbT] (Figure 4. 3b).

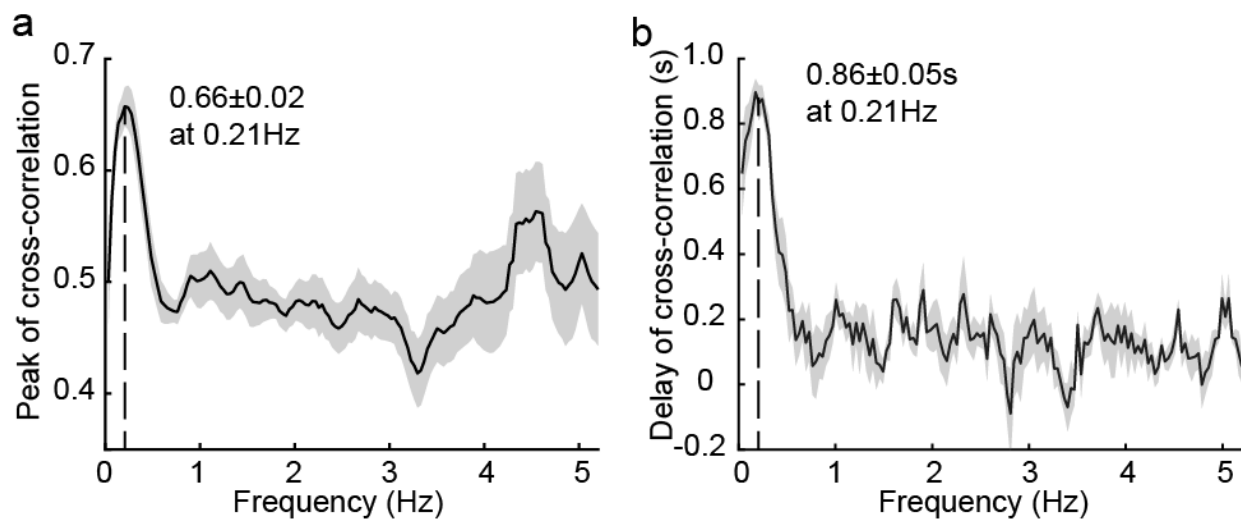


Figure 4. 3 Frequency-dependence of neurovascular correlations. a) Plot of the average peak cross correlation value between Thy1-GCaMP6f and [HbT] signals as a function of temporal band-pass frequency (0.35 Hz window, 0.035Hz increment up to Nyquist frequency at 5.2Hz, plotted frequency is the start of each band). b) Phase delay of the cross-correlation between corrected Thy1-GCaMP and [HbT] as a function of frequency. The results show the average and s.e. for all the awake animals (n=6). Time courses and image sequences with <0.4 Hz LPF are compared in Figure 4. 12.

Low pass filtering awake Thy1-GCaMP6f and [HbT] data at 0.4 Hz reveals a clear correlation (with an evident phase delay) across the cortex. Strong correlations within the 0-0.4 Hz frequency band imply that hemodynamics act as a slow temporal integrator of neural spiking activity. The clear time-shift further confirms the causality between neural and hemodynamic signals and

demonstrates that HRF-based fitting results do not originate from hemodynamic cross-talk or the correction of GCaMP fluorescence.

4.5 Model-based analysis of anesthetized resting-state data

In urethane-anesthetized Thy1-GCaMP3 animals (n=6), data were acquired using both a bilateral and unilateral thinned-skull windows (unilateral with simultaneous electrophysiological recordings). Model fitting analysis was performed utilizing the full 180 second duration of each imaging trial. Since anesthesia caused much higher variability in physiological state, mice were excluded from analysis if poor physiological state led to non-typical patterns of neural activity or hemodynamics, or if physiological monitoring implied poor health.

An example of analysis on a urethane-anesthetized mouse exhibiting a high overall correlation coefficient is shown in Figure 4. 4. Both gamma-variate and deconvolution models show excellent agreement with measured $\Delta[\text{HbT}]$ values, with Pearson's correlation coefficient of 0.89 and 0.85 respectively. A_H , T_H and W_H values exhibit consistent trends with awake data, highlighting arterioles with high A_H values (Figure 4. 4c).

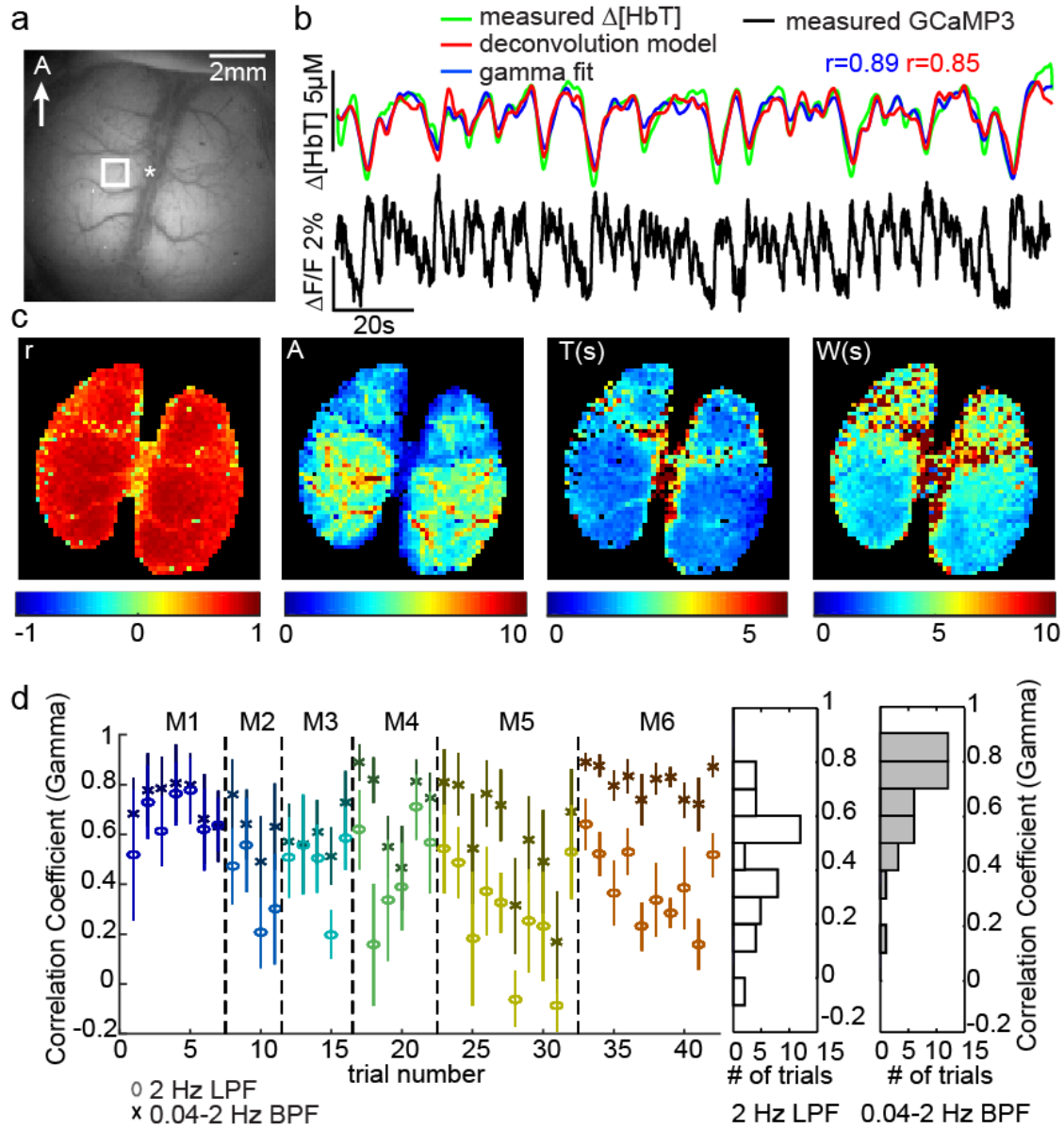


Figure 4. 4 Spatiotemporal modeling of hemodynamics from wide-field GCaMP recordings in the resting-state urethane anesthetized brain. a) An example of a urethane anesthetized Thy1-GCaMP3 mouse imaged with a similar, bilateral window over the cortex to awake mice. b) $\Delta F/F$ time-course (after hemodynamic correction) lasting 180s with simultaneously recorded $\Delta[\text{HbT}]$ from the region indicated in (a). Red and blue traces show the result of convolving the GCaMP fluorescence signal with hemodynamic response functions (HRFs) derived via deconvolution or gamma-variate fitting respectively. Both the hemodynamic and neural activity time coursed were low-pass filtered at 2Hz. (c) The spatial maps of Pearson's correlation coefficient of gamma fit, amplitude (A), time to peak (T) and width at half maximum (W) of gamma-variate function by pixel-wise HRF estimation by from the trial in (b). This

example represents the highest correlation value found within urethane anesthetized mice. Additional anesthetized mice were found to have stronger contributions from low frequency (<0.04 Hz) hemodynamic trends that were not well predicted by Thy1-GCaMP3 recordings. (d) Shows the gamma-variate equivalent result to figure 5f, demonstrating correlation coefficients across anesthetized animals, fitting before and after >0.04 Hz high pass filtering of [HbT] and corrected Thy1-GCaMP3 fluorescence.

However, other anesthetized trials yielded poorer fits. A trial with a correlation coefficient of 0.19 is shown in Figure 4. 5b. The measured Δ [HbT] time-course in this case exhibits a large decrease in [HbT] in the middle of the trial that is not accounted for in either deconvolution or gamma-variate based model-fitting. High pass filtering of hemodynamic time-courses at 0.04 Hz was found to remove these slow trends, yielding resting-state hemodynamics that more closely resemble those seen in awake data. Performing deconvolution and gamma-variate fitting after 0.04 Hz high pass filtering of both GCaMP and Δ [HbT] data dramatically improved fit correlation coefficients as shown in Figure 4. 5c. Repeated across all anesthetized animals, fitting before and after <0.04 Hz slow trend removal, the average correlation coefficients across all anesthetized animals and trials improved from 0.44 ± 0.05 to 0.68 ± 0.04 for gamma fit and 0.41 ± 0.06 to 0.70 ± 0.03 for deconvolution ($p=0.005$ and $p = 0.006$ respectively, $n=6$, paired t-test) (Figure 4. 5f and g).

4.5.1 Spatial properties of <0.04 Hz slow trends

It is possible to visualize the spatiotemporal properties of <0.04 Hz slow trends. Figure 4. 5d maps 0.04 Hz low pass filtered frames across the duration of the large decrease in [HbT] seen in Figure 4. 5b, showing a large trend across the field of view with a clear structure of pial arterioles. Figure 4. 5e shows a shorter epoch, separating frequency components of Δ [HbT] below and above 0.04

Hz and demonstrates that faster [HbT] components >0.04 Hz are still modeled by gamma-variate fitting to Thy1-GCaMP3 data during slow hemodynamic trends whereas frequencies <0.04 Hz show vascular detail consistent with arterial dilations and constrictions across the field of view. In all cases, slow trends in $\Delta[\text{HbT}]$ are not well-predicted by Thy1-GCaMP data, have vascular structure, and in animals with bilateral cortical exposures, slow trends exhibit bilateral symmetry.

4.5.2 Slow trends in awake v/s anesthetized animals

To determine whether slow hemodynamic trends are unique to urethane anesthesia, <0.04 Hz slow-trend removal analysis was repeated on all awake data. With the caveat that awake but non-running data epochs were shorter in duration (30-60 seconds), and thus trends <0.033 Hz may not be fully represented, high-pass filtering awake data at 0.04 Hz prior to fitting had a much smaller effect on fit correlation coefficients than for anesthetized data (Figure 4. 5g) (average correlations changed from 0.51 ± 0.02 to 0.58 ± 0.02 for gamma-variate fitting and 0.64 ± 0.01 to 0.63 ± 0.01 n.s. $p = 0.63$, for deconvolution all for $n=6$, paired t-test. Figure 4. 5h shows that high pass filtering at 0.04 Hz removes significantly more variance from anesthetized data than data acquired in the awake brain ($p=0.015$, $n=6$, paired t-test).

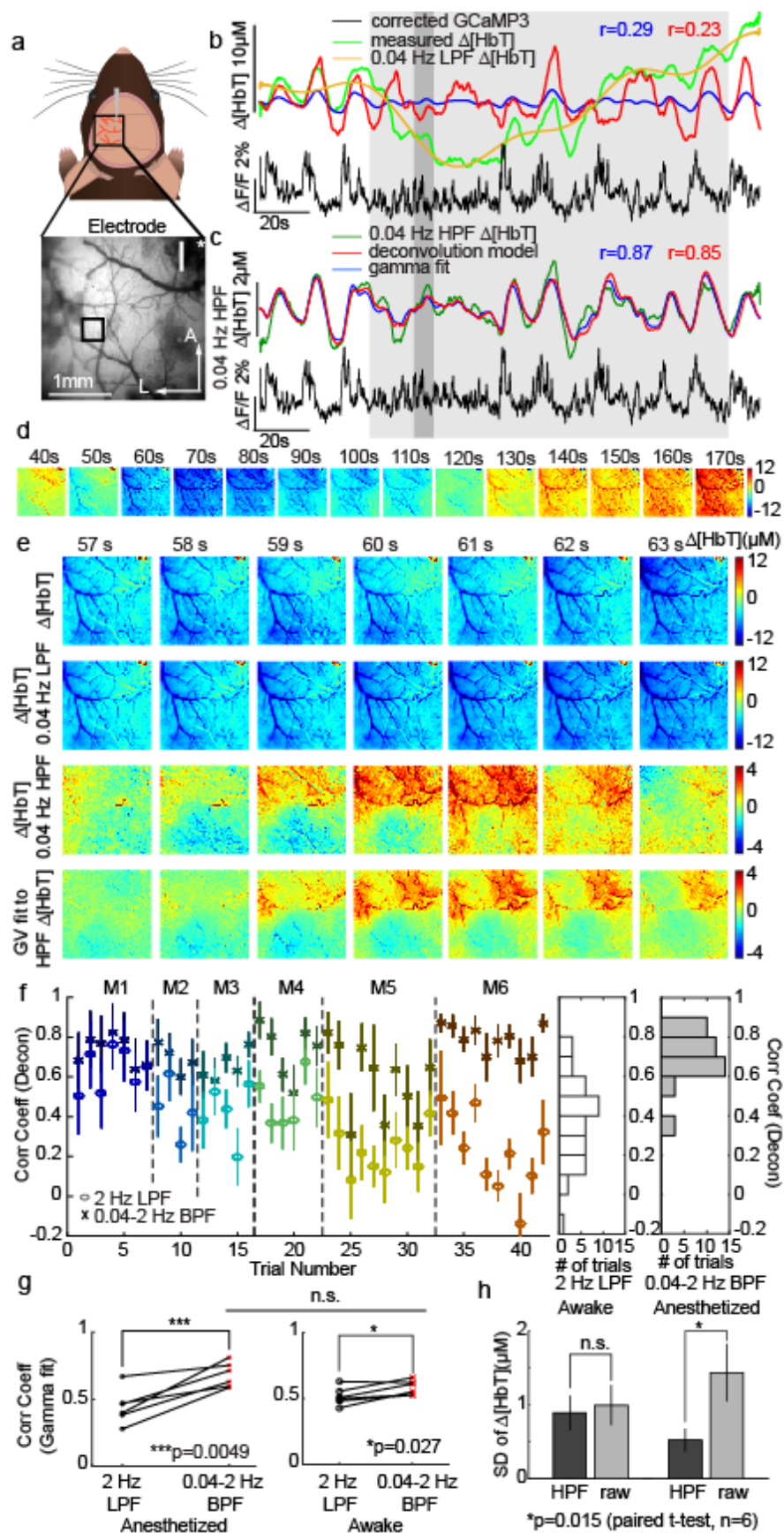


Figure 4. 5 Analysis of urethane-anesthetized animals and the presence of slow hemodynamic trends. (a) A smaller, unilateral window over S1. (b) Time courses of original $\Delta[\text{HbT}]$ and Thy1-GCaMP3 fluorescence (2 Hz LPF only) with ‘best fit’ deconvolution and gamma-variate fits. Yellow shows $<0.04\text{Hz}$ slow trend in $[\text{HbT}]$. (c) Plots as in (b) after 0.04-2 Hz band pass filtering (BPF) of both $[\text{HbT}]$ and GcaMP3 fluorescence to remove slow trends yielding improved fits. (d) Image sequence showing $<0.04\text{Hz}$ component of $\Delta[\text{HbT}]$ from 40s-170s for the same trial. (e) Image sequence from 57s-63s showing from top to bottom: original $\Delta[\text{HbT}]$ ($<2\text{ Hz LPF}$), slow trend $\Delta[\text{HbT}]$ ($<0.04\text{Hz LPF}$), $\Delta[\text{HbT}] >0.04\text{-}2\text{ Hz BPF}$, gamma-variate fit to 0.04-2 Hz BPF $\Delta[\text{HbT}]$ from 0.04-2 Hz BPF corrected GCaMP3. (f) Mean average Pearson’s correlation coefficients and SD over S1 for deconvolution model for all anesthetized animals (M1-M6) before (circles) and after (crosses) $>0.04\text{Hz}$ HPF of $[\text{HbT}]$ and GCaMP3 fluorescence. Histogram to right shows summary distributions for before (white) and after (gray) $>0.04\text{Hz}$ HPF. Gamma-variate fit results shown in Figure 4. 4. (g) Pearson’s correlation coefficients for gamma-variate fitting with only a 2 Hz LPF and after 0.04 - 2 Hz BPF of $\Delta[\text{HbT}]$ for both anesthetized and awake data for each mouse. n.s: $p = 0.05$. (h) Standard deviation of $\Delta[\text{HbT}]$ (2 Hz LPF) over time before and after $>0.04\text{ Hz HPF}$ for awake and anesthetized data.

4.6 Comparison of resting-state coupling in awake and anesthetized states

HRFs generated in awake and anesthetized conditions across all trials and mice, calculated using both gamma-variate fitting and deconvolution are compared in Figure 4. 6. The HRF in awake Thy1-GCaMP6f animals (using 0.02-2 Hz BPF) was consistently found to have a shorter time to peak ($p < 0.005$ for both models) and a narrower peak than anesthetized Thy1-GCaMP3 mice (0.04-2 Hz BPF), Figure 4. 6c ($p < 0.005$ for both models, double-sided Student’s t-test, $n=6$). These temporal features agree well with stimulus-evoked HRFs measured in awake and urethane-anesthetized rats (Martin et al., 2006), including the observation of stronger post-stimulus undershoots in the awake state (Uhlirva et al., 2016). Differences cannot be accounted for by the minimal ($<0.1\text{ s}$) difference between the temporal properties of these two GCaMP types

(Akerboom et al., 2013). However, HRF amplitudes between awake (all GCaMP6f) and anesthetized (all GCaMP3) conditions are not compared for this reason. Higher variance of HRF parameters in anesthetized animals may be due to the more widely varying physiological states of the animals during acute experiments compared to robust HRFs in awake animals (Figure 4. 6b). Spike-triggered averaging was also performed on data from both awake and anesthetized mice, averaging hemodynamic changes in [HbT], [HbO] and [HbR] corresponding to events identified within resting-state GCaMP recordings (Figure 4. 6d) (Bruyns-Haylett et al., 2013). This method is independent of an expected hemodynamic model, and was performed on GCaMP data without hemodynamic correction, and without high or low pass filtering of hemodynamic data. Results show clear evoked increases in Δ [HbT] and Δ [HbO] with decreases in Δ [HbR], consistent with functional hyperemia, and agree well with the properties of awake and anesthetized HRFs modeled by gamma-variate fitting and deconvolution (Figure 4. 6d). The anesthetized response agrees well with results reported in resting-state, urethane anesthetized rats (Bruyns-Haylett et al., 2013). Spike-triggered averaging provides strong, independent evidence that spontaneous neural activity in the resting-state awake or anesthetized brain evokes local, correlated functional hyperemia.

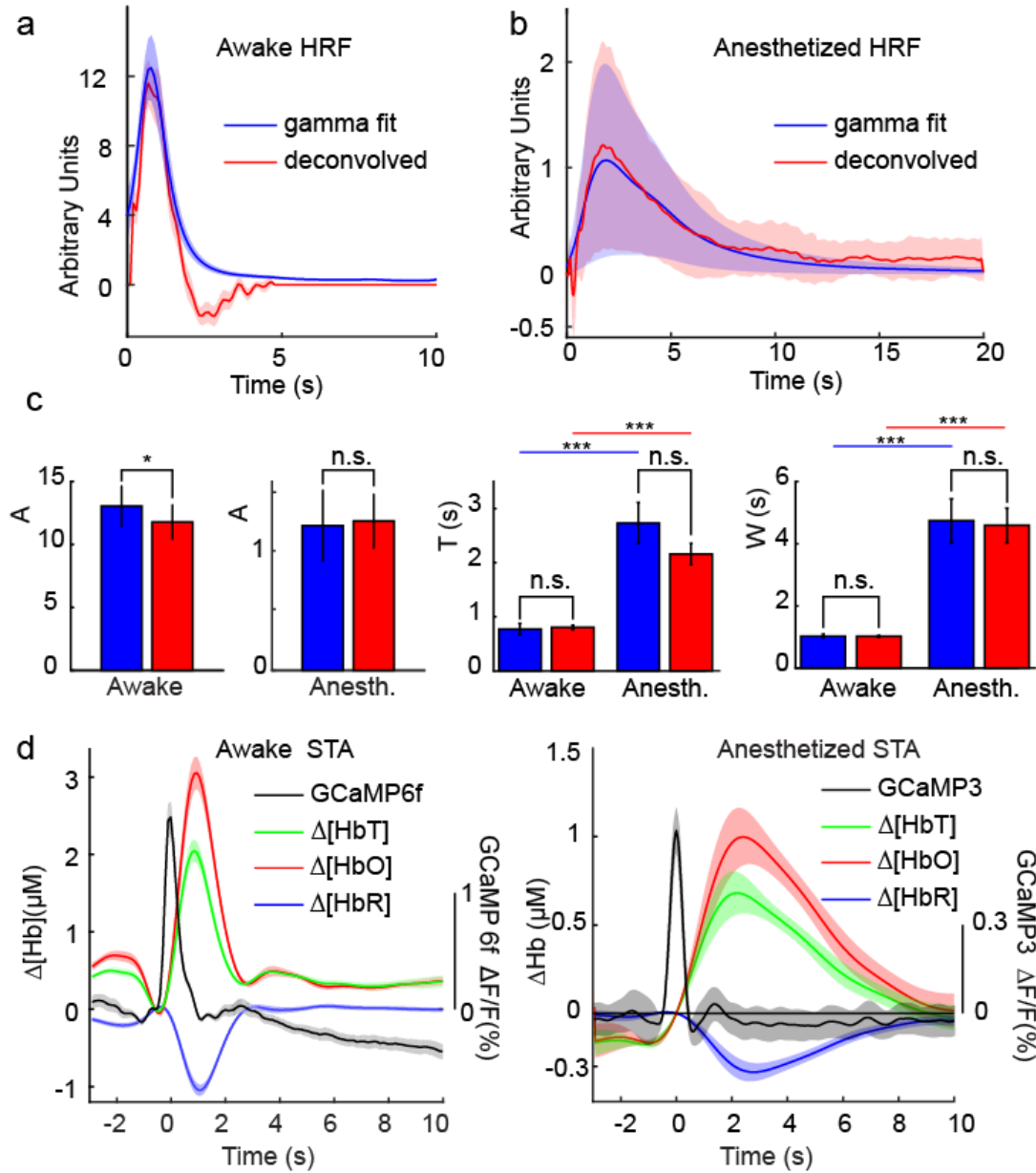


Figure 4. 6 Summary of HRFs derived from multiple analysis methods. (a-b) Comparisons of HRFs derived from gamma-variate fitting (blue) and deconvolution (red) in awake (a) and anesthetized (b) animals within the somatosensory cortex. Shaded regions show standard error across $n=6$ mice in each group. (c) Parametric comparison of values from gamma-variate fits (averaged over S1), A (* $p = 0.024$, n.s. $p=0.66$), T (n.s. awake $p=0.76$, anesth $p=0.094$, *** $p<0.005$) W (n.s. awake $p=0.88$, n.s. anesth $p=0.76$, *** $p<0.005$) all paired-wise t-test, $n=6$ group. (d) Spike triggered averaging for awake and anesthetized animals. Plots show the average among animals, shading shows standard error across animals ($n=6$ mice in each group).

4.7 Discussion

This study used wide-field optical imaging of both neural GCaMP and cortical hemodynamics in awake and anesthetized mice to visualize underlying neural correlates of resting-state hemodynamics. Electrophysiological recordings demonstrated that measured Thy1-GCaMP signals (after hemodynamic correction) could be predicted from MUA, corresponding to spiking of excitatory neurons. Thy1-GCaMP imaging of the bilaterally-exposed cortex revealed synchronous patterns of symmetric, spontaneous resting-state neural activity in both awake and anesthetized conditions. Gamma-variate fitting and deconvolution methods, assuming a linear HRF-convolution based model of neurovascular coupling, were both shown to be able to spatiotemporally predict resting-state hemodynamics from this spatially-resolved neural activity across the cortex in both awake and anesthetized mice (although slow hemodynamic trends in anesthetized animals (<0.04 Hz) were not well-predicted by Thy1-GCaMP recordings). Together, these results demonstrate that resting-state fluctuations in cortical $\Delta[\text{HbT}]$ correspond to a summation of hyperemias coupled to analogous patterns of spontaneously firing of excitatory neurons.

4.7.1 Comparison to prior studies of resting-state neurovascular coupling

Prior studies exploring resting-state neurovascular coupling have reported relatively low correlations between fMRI BOLD signals and electrophysiological recordings, typically around 0.3 (Shmuel and Leopold, 2008; Scholvinck et al., 2010; Magri et al., 2012). The methods utilized here yielded much higher spatiotemporal correlations over large areas of the mouse cortex. We attribute this improved fitting and correlation to a number of factors: 1) High-speed wide-field GCaMP imaging acts as a spatiotemporal integrator, averaging ensemble activity of multiple

neurons at a given site and over the time between measurements. The use of Thy1-GCaMP mice enabled selective sensitivity to spiking activity in excitatory neurons, without contributions from other brain cells, other types of electrical activity or interference from confounds such as simultaneous fMRI acquisition. This integration and selectivity combined might more readily reveal correlations and trends between distant groups of neurons that cannot be appreciated from single unit recordings, or two-photon microscopy observations of small, unilateral fields of view.

2) Improvements in GCaMP, illumination sources and cameras enabled high-speed, large field of view imaging of spontaneous neural activity and concurrent hemodynamics with good signal to noise with no averaging. The resulting clear view of patterns of bilaterally synchronous spontaneous neural activity in the awake brain ensure that signals are not contaminated by movement artifacts, which can be difficult to distinguish in single-point measures, or anesthesia-dependent effects.

3) The analysis approach used here assumed a neurovascular coupling model in which neural events would (directly or indirectly) evoke a stereotyped $\Delta[\text{HbT}]$ response, a model with a strong physiological basis (Hillman, 2014). HRF parameters were allowed to vary over the cortex to account for expected differences in the dynamics of different vessel types (Vanzetta et al., 2005; Hillman, 2007; Drew et al., 2011; Ma et al., 2016a). Analysis focused on modeling $\Delta[\text{HbT}]$ rather than $\Delta[\text{HbR}]$, assuming a linear neurogenic hyperemia model and removing the need to account for oxygen consumption as another variable (although $\Delta[\text{HbT}]$ was shown to be strongly correlated to $\Delta[\text{HbR}]$, and thus anticipated BOLD signals).

4) fMRI data is typically acquired at < 0.5 Hz volume rates, although longer epochs give access to lower frequencies than examined here. Our HRF analysis revealed that the awake mouse brain has a temporally narrow resting-state hemodynamic response, and frequency-dependent correlation analysis revealed a peak correlation at 0.21 Hz. The temporal resolution of prior fMRI comparisons

may thus not have been sufficient to capture hemodynamic coupling at its peak correlated frequency. 5) The removal of baseline trends was found to be important in performing fitting analysis, since different physical effects can affect neural and hemodynamic recordings (such as photobleaching), while slow hemodynamics trends seen in some anesthetized animals strongly degraded fitting and correlations. Bilateral imaging enabled the different spatiotemporal patterns of slow trends to be distinguished from higher-speed events predicted by GCaMP imaging.

Together, these factors combined to yield fits across multiple trials and animals exceeding correlations of 0.8 in both awake and anesthetized states.

4.7.2 What do observed patterns of spontaneous neural activity represent?

Wide-field Thy1-GCaMP imaging revealed bilaterally symmetric, synchronous fluctuations in neural activity across the brain, in both awake and anesthetized states, which were shown to be spatiotemporally coupled to resting-state fluctuations in hemodynamics. Previous reports using both voltage sensitive dyes and wide-field GCaMP imaging have noted similar bilaterally-symmetric cortical patterns of neural activity, inferring functional connectivity between temporally correlated regions (Mohajerani et al., 2010; Vanni and Murphy, 2014). Kozberg et al demonstrated the transition of spontaneous neural events from unilateral to bilateral in mice between P7-P14, a period of postnatal development where transcallosal axonal projections are establishing (Kozberg et al., 2016). Widespread correlations and apparent waves of activity given by correlations between fMRI and discrete LFP recordings have also been noted in the primate brain (Shmuel and Leopold, 2008). However, the origin and the physiological meaning of these patterns of neural activity remains controversial (Logothetis et al., 2009).

Waves and bursts of neural activity in the cortex are typically reported under conditions of non-rapid eye movement (REM) sleep (Destexhe et al., 1999), anesthesia (urethane, ketamine), and quiet wakefulness (Gentet et al., 2010; Mohajerani et al., 2010). Such events are characterized by alternating subthreshold cortical membrane depolarization and hyperpolarization (UP/DOWN states), slow wave activity that has been associated with memory consolidation (Destexhe and Contreras, 2006), and shaping responses to incoming stimulation (Petersen et al., 2003). Although electrophysiological recordings in both animals (Fox and Raichle, 2007; Liu et al., 2013) and awake human subjects (Nir et al., 2008) have demonstrated symmetry of spontaneous neural activity, characterization of brain-wide patterns of spontaneous neural activity in the awake brain has been limited (Brookes et al., 2011).

We propose that resting-state neural fluctuations observed here might correspond to network-based modulations of local excitability in ‘connected’ regions, with similar origins to rhythmic neocortical UP and DOWN states. A modulation in excitability would increase the likelihood of neurons with the region to fire, but would not necessarily cause the same neuron to fire each time excitability increased. This mechanism could explain why neural correlations are less evident in single-unit recordings and cellular-level imaging of small brain regions (Li et al., 2015) but are evident in spatiotemporally integrated wide-field Thy1-GCaMP recordings. Examining raw Thy1-GCaMP traces, a clear enveloping of neural activity can be seen in most cases, where events periodically become more frequent or cluster to form higher amplitude GCaMP signals, preempting subsequent increases in local HbT. Frequency-resolved cross-correlations (Figure 4. 3) confirm that hemodynamics and GCaMP share a low frequency component from which correlations arise. The observation that UP states can synchronize activity in the LFP gamma band (Ruiz-Mejias et al., 2011) may explain previous findings of correlations between gamma band LFP

and fMRI signals (Murayama et al., 2010; Scholvinck et al., 2010; Magri et al., 2012). However, since Thy1-GCaMP measurements provide sensitivity to spiking activity, with no expected representation of low frequency changes in LFPs, our results demonstrate that resting state hemodynamics result from a pathway of events that includes modulation in the spike rate of excitatory neurons, an effect that may be causally or otherwise coupled to modulations in gamma band LFP (Shmuel and Leopold, 2008).

It should also be noted that our results do not exclude the contribution of other cellular activity to resting state hemodynamics. Interneurons, for example, have been implicated to play a role in neurovascular coupling (Cauli et al., 2004; Uhlirova et al., 2016), while there has also been significant debate regarding the BOLD response that should result from interneuron activation (Devor et al., 2007; Ekstrom, 2010; Anenberg et al., 2015; Boorman et al., 2015). Our results demonstrate that the activity of excitatory neurons is correlated to resting state hemodynamics. However, any other form of cellular activity in the brain that is spatiotemporally coupled to neural spiking could thus also be correlated to resting state hemodynamics. For example, spontaneous interneuron activity could feasibly be correlated to the modulation of excitatory neural activity and could therefore share a correlation with resting state hemodynamics. This possibility also underscores that correlation does not imply causality. Similarly, synchronous activation of astrocytes, pericytes or interneurons in the context of neurovascular coupling could contribute to the properties of the HRF, with the delayed undershoot observed in our awake, deconvolved HRFs being particularly interesting in the context of interneuron involvement (Uhlirova et al., 2016). Thus, although our studies here focused on correlations between excitatory neural activity and resting state hemodynamics, further work is needed to chart the cellular pathways and dependencies of both neuromodulation, and neurovascular coupling in the resting state.

4.7.3 Effects of anesthesia and slow hemodynamic trends

Despite differences in the temporal shape of HRFs between urethane-anesthetized and awake mice, our results demonstrate that resting-state coupling between excitatory neurons and hemodynamics is intact in both conditions. In some cases, anesthetized animals were found to exhibit large, slow (<0.04 Hz) hemodynamic trends that were not well predicted by simultaneous GCaMP recordings. However, despite poor fitting, these periods did not represent complete ‘uncoupling’, since removal of the slow hemodynamic component using a 0.04 Hz high pass filter left residual hemodynamics that could still be well predicted by local GCaMP fluctuations.

In considering the origin of these slow hemodynamic trends, it should again be noted that Thy1-GCaMP fluorescence selectively reports spiking activity in excitatory neurons in layers 2/3 and 5. Slower hemodynamic trends could thus be driven by other neuronal or cellular components of the brain whose activity is not spatiotemporally coupled to excitatory neural activity. Many prior studies have reported that activation or inhibition of structures such as the basal forebrain (nucleus basalis of Meynert) and the locus coeruleus (Bekar et al., 2012; Takata et al., 2013) can modulate cortical blood flow, and might be expected to have lower spatial specificity, consistent with the spatial patterns of slow trends shown in Figure 4. 5. Pisauero et al. demonstrated ‘global’ hemodynamic fluctuations in awake mice that correlated with pupil diameter, which infers brain arousal or alertness (Pisauero et al., 2016), while similar results were also found in awake behaving primates by Cardoso M. et al (Cardoso et al., 2012). Interneurons subtypes capable of altering blood flow may also play a role here (Cauli et al., 2004), while systemic blood pressure changes (Chen et al.), or even activities such as running (Huo et al., 2014) and anticipation (Sirotnin and Das, 2009) have been shown to cause blood flow modulations. Hemodynamics caused by these mechanisms may not be driven through the same neural pathways captured through recordings of

local cortical spiking in Thy1-GCaMP mice. If the spatial dependencies of these alternative coupling mechanisms are different from local coupling, they could feasibly influence derived functional connectivity networks if present in resting-state fMRI data.

4.7.4 Implications for resting-state fMRI

Our ability to visualize excitatory neural activity as ‘ground truth’ enabled linearly-coupled resting-state hemodynamics to be distinguished from noise, experimental variance and slow hemodynamic trends. However, removal of contamination from (already random) resting-state fMRI data is far more challenging without this prior. Without proper characterization of contamination effects, non-specific pre-conditioning of fMRI data such as low pass filtering and global regression could feasibly yield inferred networks with different dependencies on brain state, physiology or other components of brain activity dependent on the source of hemodynamic contamination. Our results further suggest that fMRI analysis should consider the possibility of region-specific HRFs (and contamination) throughout different brain regions (Handwerker et al., 2004).

Despite these caveats, the results presented here demonstrate the clear presence of network-like, bilaterally symmetric spontaneous neural events in the awake and anesthetized brain that can accurately predict spatiotemporal patterns of resting-state hemodynamics. Although analysis focused on changes in HbT, these dynamics were shown to be temporally correlated to HbR changes (Figure 4. 1) indicating that evoked hyperemias are the primary drivers of the resting-state BOLD signal in fMRI. Model-based fitting results imply a more reliably linear relationship between neural activity and hemodynamics in the resting-state compared to non-linearities observed in stimulus-evoked responses (Devor et al., 2003; Jones et al., 2004; Yesilyurt et al.,

2008). This demonstration suggests a firm basis for resting-state functional connectivity mapping as resolving the properties of a brain-wide network of activity observed as modulations in the spike rate of excitatory neurons. Coupling was most robust in the awake mouse brain, a closer state to awake human studies than conditions under anesthesia.

4.8 Supplemental Figures

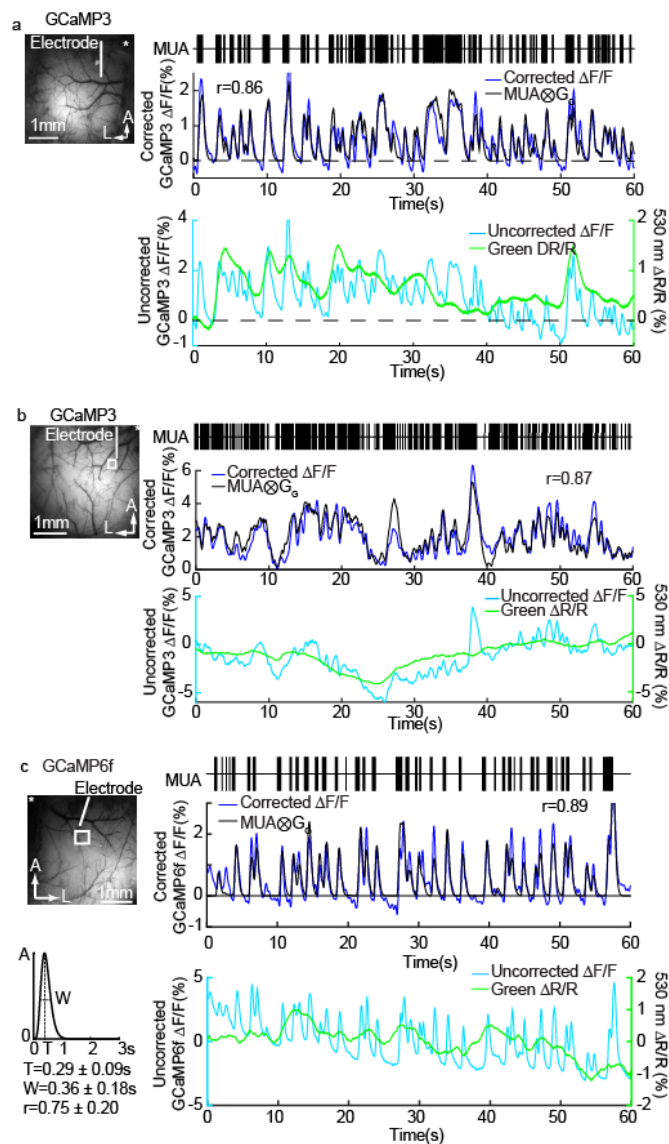


Figure 4. 7 Electrophysiology comparison in Thy1-GCaMP3 and Thy1-GCaMP6f mice. (a) Concurrent recordings of MUA and hemodynamics-corrected GCaMP3 fluorescence and (b) recordings from a Thy1-GCaMP3 animal (open skull craniotomy) accompanied by uncorrected GCaMP fluorescence time-courses and simultaneous green (530nm) reflectance, showing contaminating effects of hemodynamics in the wide-field fluorescence imaging. (c) An example from a Thy1-GCaMP6f animal (unilateral thin-skull) showing similar correspondence of electrophysiological recordings and fluorescence changes. The GCaMP6f MUA kernel shows the averaged gamma-variate function used to fit fluorescence with MUA and the values shown

represent mean \pm std. All measurements were made under urethane anesthesia. All fluorescence and hemodynamic data is shown after low-pass filtering at 2Hz.

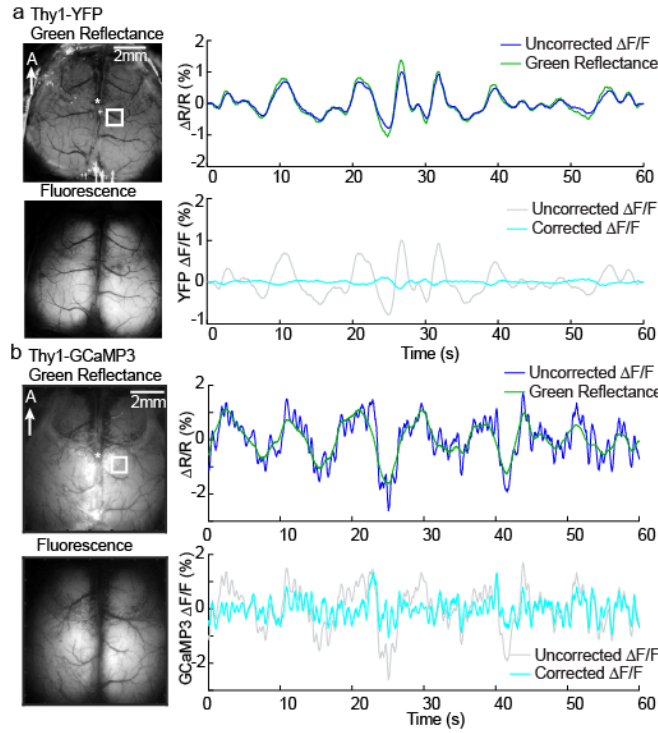


Figure 4. 8 Control experiment comparing WFOM measurements in Thy1-YFP and Thy1-GCaMP3 mice. (a) Urethane anesthetized Thy1-YFP mice were imaged using an EM-CCD based WFOM system. Representative time courses from the somatosensory region (marked by the white box) show that changes in YFP fluorescence closely follow the trend of green reflectance demonstrating the dominant effect of hemodynamic cross-talk. (b) Shows equivalent measurements in a urethane-anesthetized Thy1-GCaMP3 mouse. All neural and hemodynamic signals are shown band-pass filtered at 0.02-2Hz. After correcting for hemodynamic cross-talk in the fluorescence signals, residual changes in the Thy1-YFP mouse are around 0.2 % compared to >1 % spikes of activity remaining following hemodynamic correction of data from the Thy1-GCaMP3 mouse. Residual fluctuations in the YFP signal after hemodynamic correction may be attributable to the dynamics of flavoprotein fluorescence (Kozberg et al., 2016), which are expected to follow neural activity (Shibuki et al., 2003). The small contribution of flavoprotein fluorescence to GCaMP fluorescence measurements is difficult to discern, but would be expected to slightly broaden the apparent GCaMP response kernel.

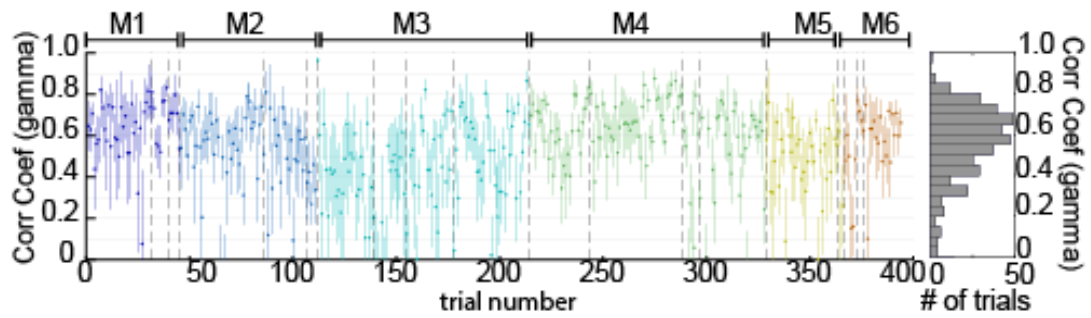


Figure 4. 9 Mean average and standard deviation Pearson's correlation for gamma-variate fitting in awake animals. All resting-state trials in all the awake animals (n=6) are shown. Values are ordered chronologically with dotted lines indicating recordings on different days and colors indicating different mice. Histogram to right shows the distribution of average (over S1) Pearson's correlation coefficient across all resting-state epochs in all trials in all awake mice. Similarly to Figure 4. 2f, the hemodynamic and corrected neural signals were temporally band pass filtered between 0.02 – 2 Hz before fitting.

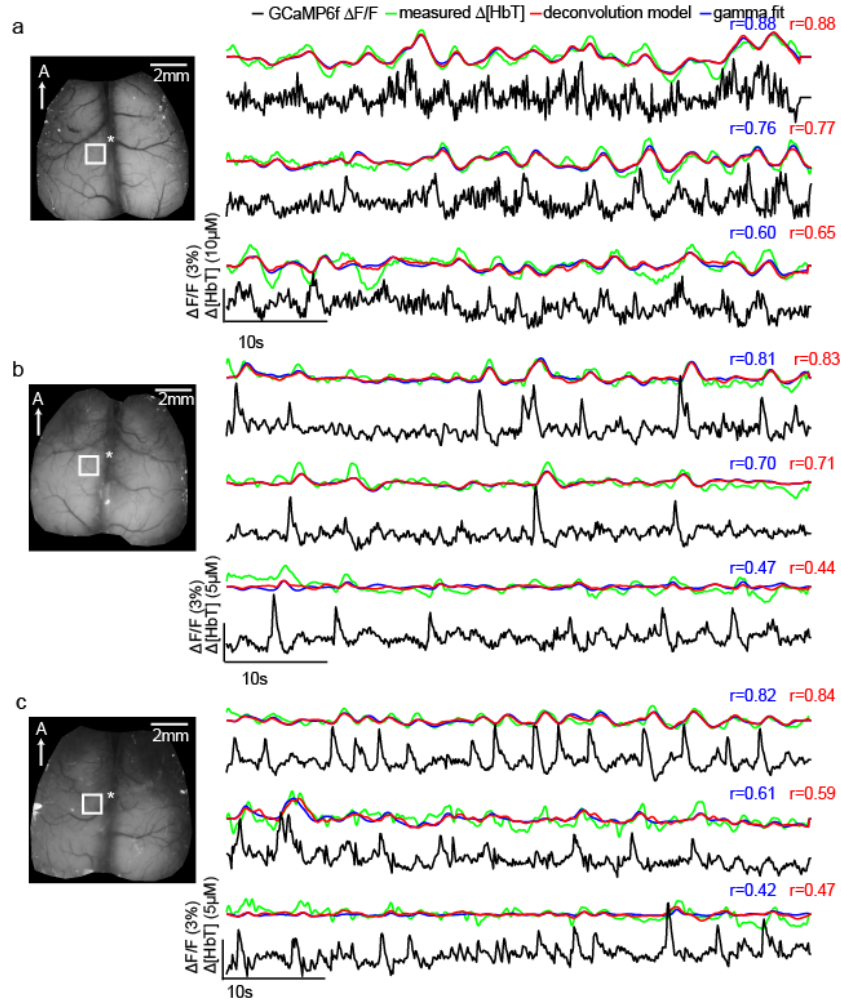


Figure 4. 10 Examples of model-based fitting of neural activity to resting state hemodynamics in awake Thy1-GCaMP6f mice: Same region, different trials. Three representative trials in the same imaging session are shown with good, mediocre and poor fitting results from three different animals. All animals were awake and resting throughout all trials. Time courses shown were all chosen from somatosensory area as marked by white boxes. Thy1-GCaMP6f $\Delta F/F$ traces are shown after hemodynamic correction. All time-courses were temporally band-pass filtered between 0.02 – 2 Hz prior to fitting, although GCaMP data is plotted here with only 0.02 Hz high pass filtering. Red and blue traces show the result of convolving the corrected Thy1-GCaMP6f fluorescence signal with hemodynamic response functions (HRFs) derived via deconvolution or gamma-variate fitting respectively. The Pearson's correlation coefficients used to evaluate the goodness of fit are color-coded similarly. The performances of the two methods are comparable on the same trials. In all cases, the general trends of $\Delta[HbT]$ data are reproduced in the convolved fits. Correlation

coefficients are degraded by effects such as slow drifts (visible in the 3rd example in b) and by higher frequency fluctuations in $\Delta[\text{HbT}]$ which may be attributable to motion artifacts, especially from breathing (2nd and 3rd examples in c).

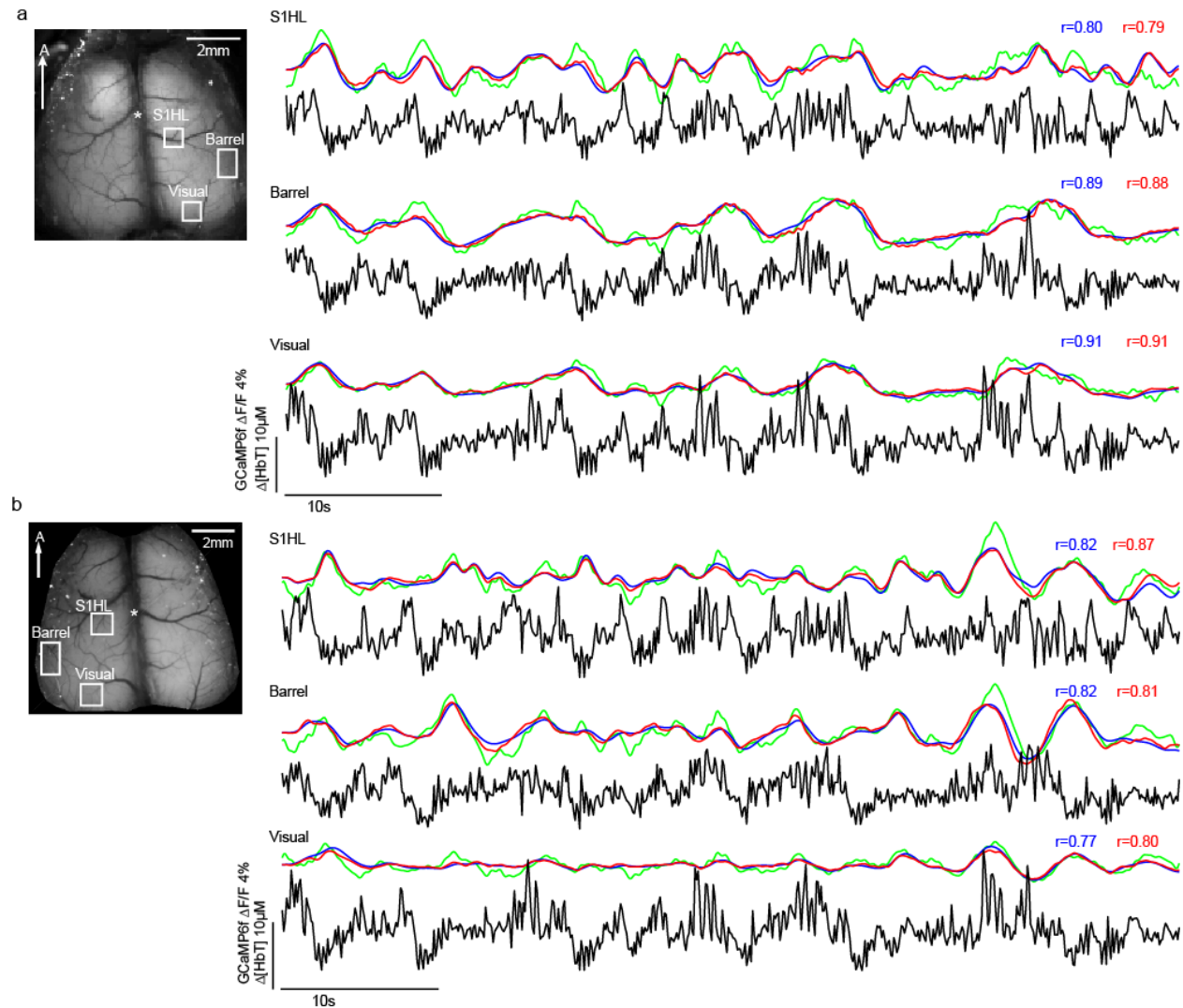


Figure 4. 11 Examples of model-based fitting of neural activity to resting state hemodynamics in awake Thy1-GCaMP6f mice: Same trial, different regions, two imaging sessions. Time courses of corrected GCaMP6f fluorescence, $\Delta[\text{HbT}]$ and its prediction from gamma fit and deconvolution models, extracted from approximate hind-limb, barrel cortex and visual cortex regions within the same imaging trial for two different imaging sessions (a and b). The animals were awake and resting throughout the trials shown. The corrected neural and hemodynamic signals were temporally band pass filtered between 0.02-2 Hz, although GCaMP

data is plotted here with only 0.02 Hz high pass filtering. The gamma-variate fit is shown in blue, while the deconvolution model is shown in red. The goodness of fit is consistent across the different functional regions, while neural activity differs between each region.

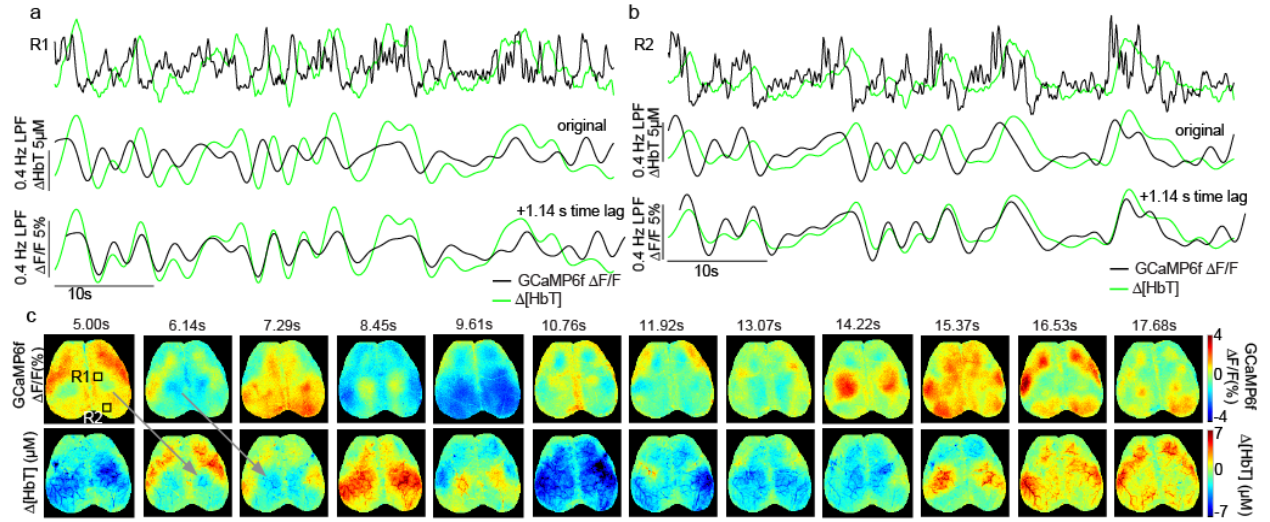


Figure 4. 12 The correspondence between neural activity and hemodynamics at <0.4 Hz in awake mouse brain.

Time courses from regions R1 (a) and R2 in (b) are the same region as shown in Figure 4. 2a. Changes in corrected Thy1-GCaMP6f fluorescence and $\Delta[\text{HbT}]$ are plotted as unfiltered (top row), 0.4 Hz low-pass filtered (middle row) and 0.4 Hz low-pass filtered and temporally shifted by 1.14s (bottom row). (c) The corresponding time-series of images from 5 to 17.5s of neural activity and hemodynamic after < 0.4 Hz filtering (shown in 1.14s steps, corresponding to the phase lag found between neural and hemodynamics of this trial). Patterns of integrated neural activity closely match subsequent patterns of hemodynamics seen in the following panel. The <0.4 Hz frequency band was chosen based on frequency-dependent cross-correlation analysis shown in Figure 4. 3. This result demonstrates that independent of linear model-based fitting, the low frequency enveloping of neural activity shows strong spatiotemporal correlations with hemodynamics at low frequencies. The clear temporal delay between neural and hemodynamic signals rules out the possibility that this effect results from hemodynamic cross-talk.

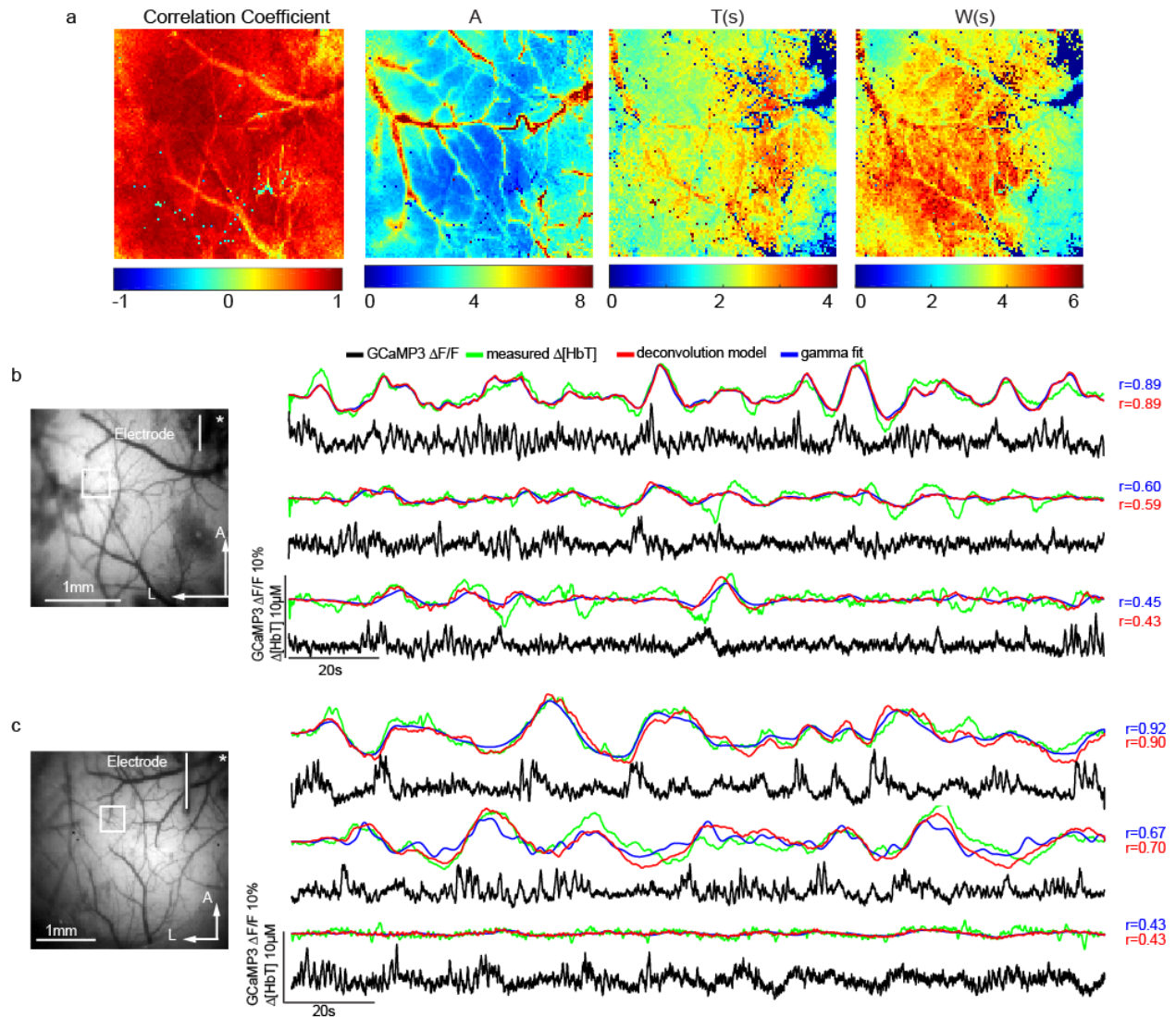


Figure 4. 13 Examples of model-based fitting of neural activity to resting state hemodynamics in urethane-anesthetized Thy1-GCaMP3 mice: Same region, different trials. (a) Spatial maps of the Pearson's correlation coefficients, amplitude (A), time to peak (T) and width at half maximum (W) of gamma-variate pixel-wise HRF estimation for a zoomed-in unilateral field of view (same trial as in Figure 4. 5c, including 0.04-2Hz temporal filtering). (b) Three representative trials for the same animal (lasting 180s) with good, mediocre and poor correlation coefficients (equivalent for a second animal are shown in c). Red and blue traces show the results of convolving corrected Thy1-GCaMP3 fluorescence signals from within the white boxes shown with HRFs derived via deconvolution or gamma-variate fitting respectively (Pearson's correlation coefficients are similarly color-coded). Slow trends were removed in all cases by temporally band-pass

filtering both corrected $\Delta F/F$ and hemodynamic signals between 0.04-2 Hz before fitting, although $\Delta F/F$ time-courses are plotted with only 0.04 Hz high pass filtering to show high frequency components. As with awake animals, the general trends of [HbT] changes are reproduced in all fits. Correlation coefficients are degraded by higher frequency fluctuations on [HbT] traces that in some cases can be attributed to motion such as breathing that cannot be reproduced by convolution with a best-fit HRF. Although such artifacts could be removed through low pass filtering of [HbT], these higher frequencies were retained to enable higher frequency components of the HRF (such as its fast initial rise) to be maintained in frequency space.

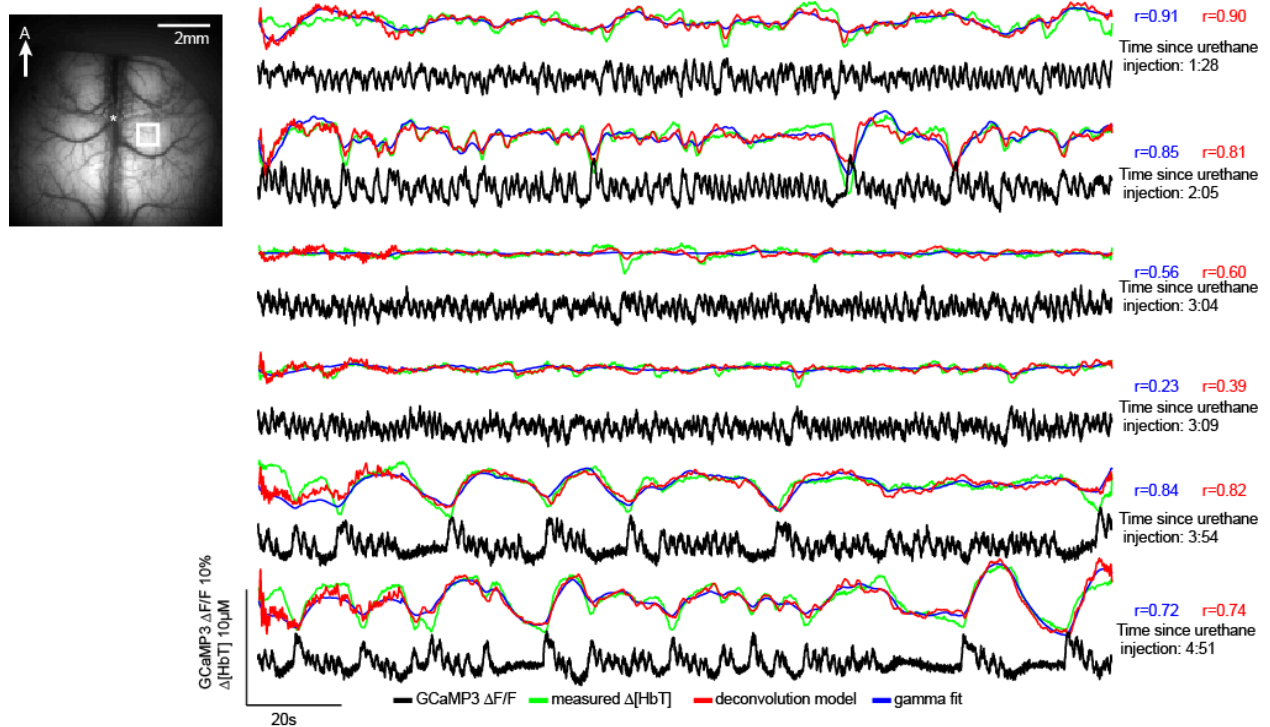


Figure 4. 14 Comparison of model-based fitting of neural activity to resting state hemodynamics during different neural states in a urethane-anesthetized Thy1-GCaMP3 mouse. During a 5 hour acute experiment, resting state trials captured different types of neural activity within the same mouse. Plots show time-courses from the same somatosensory region ordered chronologically (time since urethane anesthesia induction is indicated on the right). Corrected Thy1-GCaMP3 fluorescence and the hemodynamic signals were temporally band pass filtered from 0.04-2 Hz prior to fitting in all cases, although $\Delta F/F$ time-courses

are plotted with only 0.04 Hz high pass filtering. Deconvolution and gamma-variate fitting results are shown in red and blue respectively. Despite clear changes in the type of spontaneous neural activity present in the brain, hemodynamics are well-predicted by both linear models. Of note, in the middle time-points, neural activity consists of dense firing events, which when convolved with an HRF result in an almost flat [HbT] prediction, which is consistent with the low variance seen in measured [HbT]. It is clear that this fit provides an accurate representation of cortical hemodynamics in this state, although the (amplitude-independent) Pearson's correlation coefficient for this fit is degraded by the presence of small fluctuations in measured [HbT] likely caused by motion artifacts.

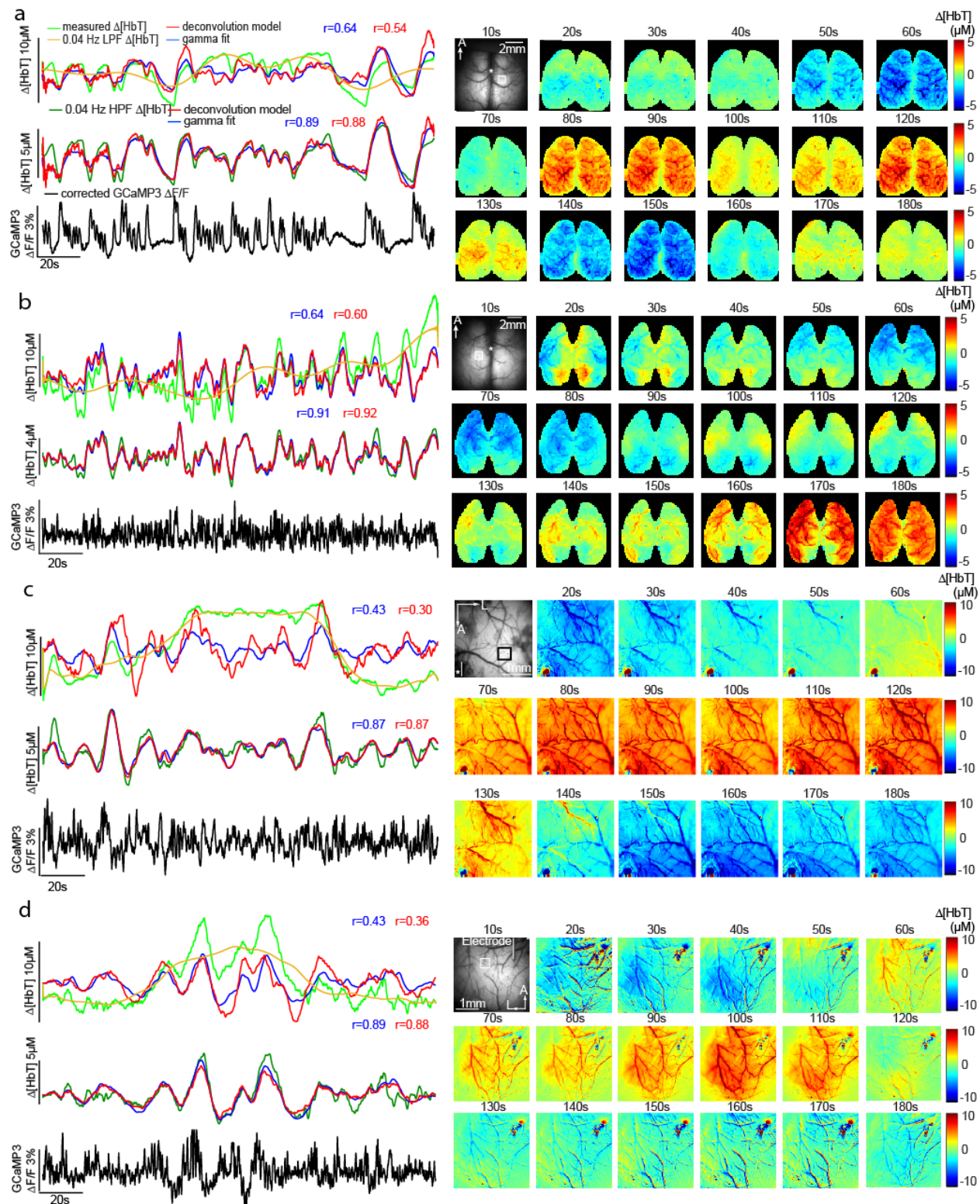


Figure 4. 15 Demonstration of the spatial representation of slow hemodynamic trends in multiple urethane anesthetized Thy1-GCaMP3 mice. Examples equivalent to Figure 4. 5(b-d) are shown for 4 additional mice.

In each example, time courses of unfiltered $\Delta[\text{HbT}]$ (green), its $<0.04\text{Hz}$ slow trend (yellow) and the corresponding fit from deconvolution (red) and gamma-variate (blue) models (top) are compared with fits after removal of slow trends via 0.04Hz high pass filtering (below). All data was low pass filtered at 2 Hz . Hemodynamics-corrected GCaMP also high-pass filtered at 0.04Hz $\Delta F/F$ is shown in each case. In all cases, Pearson's correlation coefficients are significantly improved when data is first high pass filtered at 0.04 Hz to remove slow hemodynamic trends. Image sequences on the right show the slow hemodynamic trend (temporally low-pass filtered at 0.04Hz) over the entire duration of the trials on the left. (a) and (b) with bilateral thinned-skull windows show bilateral symmetry of this slow 0.04Hz slow trend. (c) and (d) with the zoomed-in fields of view show that slow trends involve constriction and dilation of pial arteries.

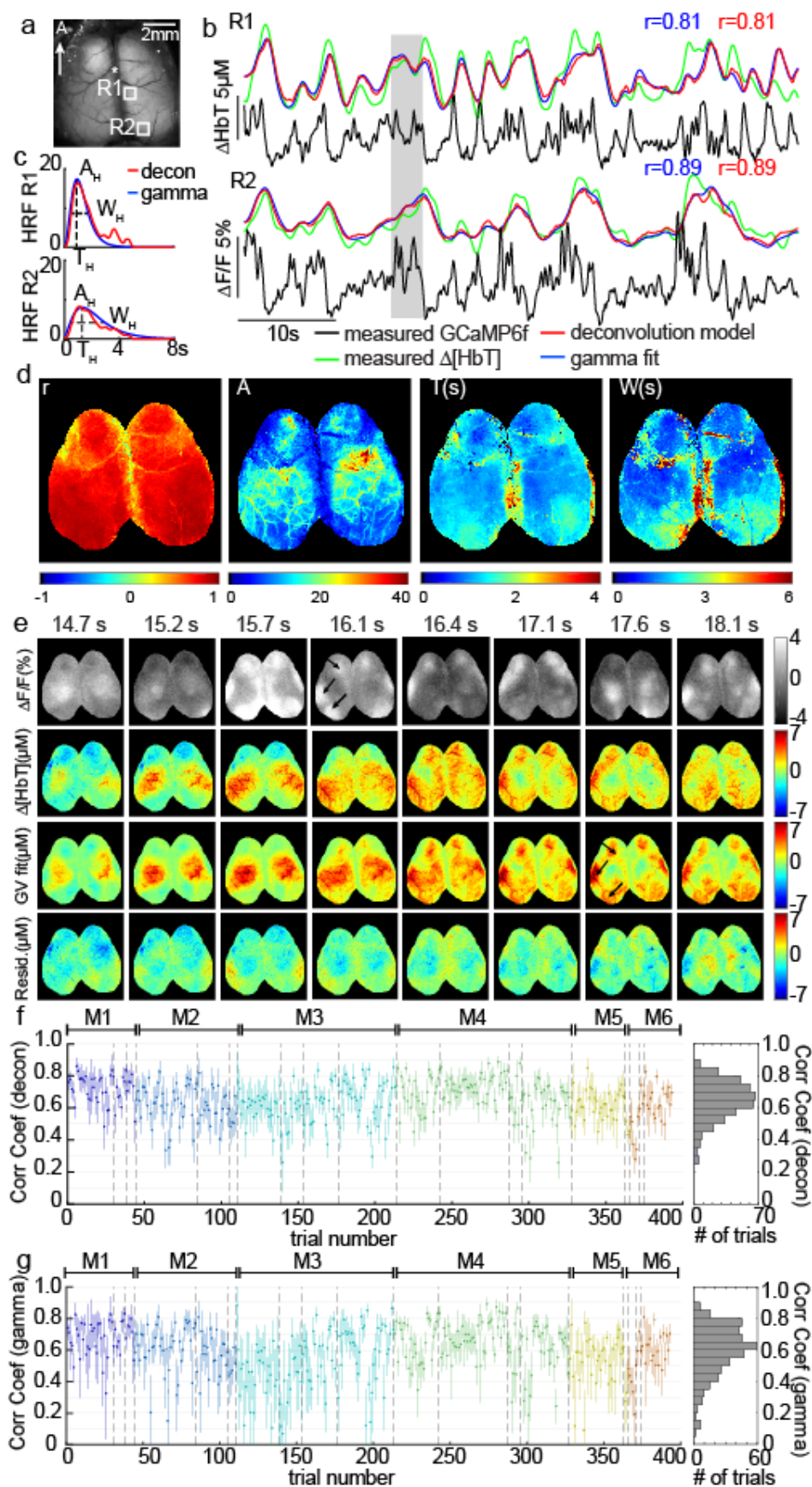


Figure 4. 16 Results of awake resting-state neurovascular coupling analysis including high-pass filtering at 0.04Hz to reduce slow trends. (Equivalent to Figure 4. 2) (a) Awake mouse field of view under blue illumination, (b) 60s examples of awake, resting-state Thy1-GCaMP6f $\Delta F/F$ time-courses (after hemodynamic correction) with simultaneously recorded $\Delta[HbT]$ from the regions indicated in (a). Red and blue traces show the results of convolving the corrected fluorescence signal with HRFs derived via deconvolution or gamma-variate fitting respectively (c) Deconvolved HRFs and best-fit gamma-variate HRFs for the 2 regions shown in (a and b) illustrating the amplitude A_H , time of peak as T_H and width at half-maximum as W_H gamma-fit parameters. (d) Left: spatially-resolved map of the gamma fit Pearson's correlation coefficients (r) per pixel and Right: Gamma-variate HRF parameters (A_H , T_H and W_H) yielding the best fitting $\Delta[HbT]$ to GCaMP fluorescence at each pixel, for the trial shown in (b). (e) Example of fitting for the same trial. Top row shows corrected GCaMP $\Delta F/F$, while the second row shows measured $\Delta[HbT]$. The 3rd row shows the gamma-variate model fit to $\Delta[HbT]$ based on the GCaMP signal. The bottom row shows fit residuals. Arrows mark specific neural events that are mirrored in later hemodynamics. (f) Plot of mean average and standard deviation (over 16 x 16 pixels over S1) Pearson's correlation of (f) deconvolution model and (g) gamma-variate fit for every resting-state trial in every animal. Values are ordered chronologically with dotted lines indicating recordings on different days and colors indicating different mice. Histogram to right shows the distribution of average (over S1) Pearson's correlation coefficient across all resting-state epochs in all trials in all awake mice. No significant improvement in fitting is seen after 0.04 Hz high pass filtering compared to Figure 4. 2, indicating a reduced influence of slow hemodynamic trends in the awake condition.

Chapter 5

Locomotion-associated neural dynamics

In previous chapters, I have demonstrated that the wide-field optical mapping is a reliable way of recording simultaneous cortical neural and hemodynamic activity in awake mice. By quantitatively solving for the HRF or the impulse function of the neurovascular coupling system, I established a linear relationship between local neural and hemodynamic changes at resting state. As described in the previous chapter, this analysis was applied to the epochs where the animal remained unmoved for at least 20s. When the animal was running, however, we observed repetitive patterns of enormous increases in the neural activity of the primary somatosensory region, overpowering the spontaneous events. In this chapter, I will explore of the spatiotemporal neural activation pattern associated with spontaneous locomotion at a mesoscopic level. Firstly, a descriptive method based on the running-triggered average was used to summarize the general trend of neural patterns preceding and during the running. However, changes in some regions are subtle, and it is challenging to form a statistically sound conclusion. I therefore explored another route of quantifying the contribution of each functional region by mathematically fitting the fluorescence WFOM data to linear regression models.

5.1 Introduction

Simple behaviors in animals are usually accompanied by dynamic activations across several functional regions. Running is known to strongly modulate ongoing neural activity across the cortex. In addition to the recruitment of the somatosensory region and barrel cortex (Huo et al., 2014; Welshblatt et al., 2016), locomotion has been proven to regulate the spatial integration of visual cortex (Ayaz et al., 2013; Saleem et al., 2013) and the gain of visual inputs (Niell and Stryker, 2010). Most studies of motor control and motor preparation were done by recording multi-unit activity electrophysiologically or two-photon microscopic imaging, both of which depict local neural activity at the cellular level. With the accessibility of a single neuron's activity, studies revealed that neurons in a small field of view can have diverse selectivity towards the moving parameters. For example, during the preparatory stage of licking behavior in mice, neurons in anterior lateral motor cortex (ALM) have varied preference for object location, licking direction and different phases of the task (Chen et al., 2017). This result, along with many other studies, stresses the central role of motor cortex in integrating the information from sensory, visual and motor region (Cisek and Kalaska, 2010; Miller and Buschman, 2013).

To further investigate coordinated interactions among the cortical regions, multi-site electrophysiological recordings and cortex-wide functional imaging were adopted to visualize the information flow across the cortex (Ferezou et al., 2007; Siegel et al., 2015). More recent studies combined wide-field fluorescence imaging with a targeted calcium sensor expressed on various types of neurons, and surveyed the dynamic changes across cell-type specific networks in awake and behaving mice (Allen et al., 2017). However, the details of cortex-wide neural information flow associated with locomotion and locomotion planning remains unclear.

The aim of this study is to pinpoint the spatiotemporal neural patterns at the whole cortex level preceding and during voluntary locomotion. Dynamic activity of cortical layers II/III and V excitatory neurons were visualized by fluorescence WFOM system in awake mice.

5.2 Materials and Methods

4 adult (age) Thy1-GCaMP6f mice (Jackson Laboratory, C57BL/6J-Tg (Thy1-GCaMP6f) GP5.17Dkim/J) were used in this study. The surgical preparation and data acquisition process is similar to the awake imaging procedure described before.

Specifically, after the chronic window implantation, each animal was imaged for multiple imaging sessions at least 3 days apart. Simultaneous GCaMP6f fluorescence and intrinsic hemodynamic signals were recorded at framerate of 10.41 Hz and 5ms exposure time. Each imaging session lasted up to two hours and trials with and without stimulations were intermingled at random order during imaging session.

While the animal's head was fixed by customary head-plate, the height of the tread mill was adjusted so that the animals could comfortably stand, walk or run at their will. Another camera (Sony PlayStation Eye Camera) monitoring animal's behavior during imaging was placed underneath the transparent wheel and configured to synchronize with the brain imaging system. To prevent the flashing illumination of strobing LEDs contaminating behavioral analysis, a 690nm long-pass filter was mounted in front of the webcam, while an infrared LED illuminates the experimental setup through the transparent wheel. The animals' behavior were recorded at 30 Hz with 640x480 resolution and then motion detection algorithm was applied by thresholding moving

standard deviation (window size: 1s) of changes between frames. The running label was then interpolated to the same framerate as brain imaging dataset.

Previous analysis has shown that the raw GCaMP images under blue illumination have strong vessel artifacts and low-frequency trends resembling changes in hemodynamics. Therefore, after initial down-sampling from 512x512 to 64x64 by averaging 8x8 blocks, the single-wavelength correction method was applied pixel-wise to the raw $\Delta F/F$ GCaMP signal to illuminate hemodynamic confound. An automatic algorithm was developed to determine whether a pixel is a brain region. Specifically, a standard deviation map of the blue channel was calculated, and showed that brain regions tend to have higher values due to the frequent GCaMP activity while the background tends to be invariant. The distribution histogram of the standard deviation was plotted and the valley between two local maximums was set to be the brain mask threshold. The pixels that had higher variance than the threshold were kept for further analysis.

To remove the global photo-bleaching trend in the GCaMP signal, the time courses from each pixel were detrended by subtracting the moving average with a window length of 90s. Within one imaging session, the relative position of the head restraint and camera was kept unchanged, and therefore trials with no stimulation were concatenated without registration. The total length for the dataset from one imaging session ranges from 27min to 50min, during which the animal may be at rest or running voluntarily. The animal's moving state captured by behavioral camera was then aligned with brain images. Running segments were isolated according to the movement detected by the behavioral camera.

5.3 Neural pattern revealed by running-triggered average

With no stimulation and constraint given during the imaging session, the animals were able to run at their will. In order to quantitatively investigate the neural activation pattern leading the movement, we applied running-triggered average analysis, which is a method adapted from the concept of event-related potential (ERP) commonly used in electrophysiological analysis. By aligning and averaging the event of interest, this method evens out the random brain activity while preserving the general trend of relevant response.

As described in the method, the animal's behavior during the awake imaging session was recorded by another camera placed underneath the transparent tread mill. By calculating the temporal variance of the monitoring images, the motion of the animal can be reliably detected. The running epochs were defined as continuous motion for a least 0.5s. The GCaMP activity ranging from 10s before to 10s after the motion onset were segmented and aligned at the onset ($t = 0s$) and zeroed at the 10th second before the onset. Figure 5. 1b illustrates the development of neural activity before and during locomotion revealed averaging 29 spontaneous moving epochs with at least 2s running and at least 10s resting before the onset from the same imaging session. When the running started at 0s, the retrosplenial region on the median side of the cortex was activated the first, followed by huge increase in the primary somatosensory cortex (labeled as S1 in figure). The elevation in somatosensory region sustained for the duration of running, while the visual cortex (V1) and the motor cortex (M1) peaked at the onset of the running and went back to baseline soon after wards. Contrary to the activity in primary somatosensory region, the secondary sensory cortex (S2) on the lateral side of the brain and the secondary motor cortex (lateral to the M1) exhibit decreased activation. Note the color scale for the running duration is not symmetrical and the decrease in the S2 region had a much smaller amplitude than the increase in S1.

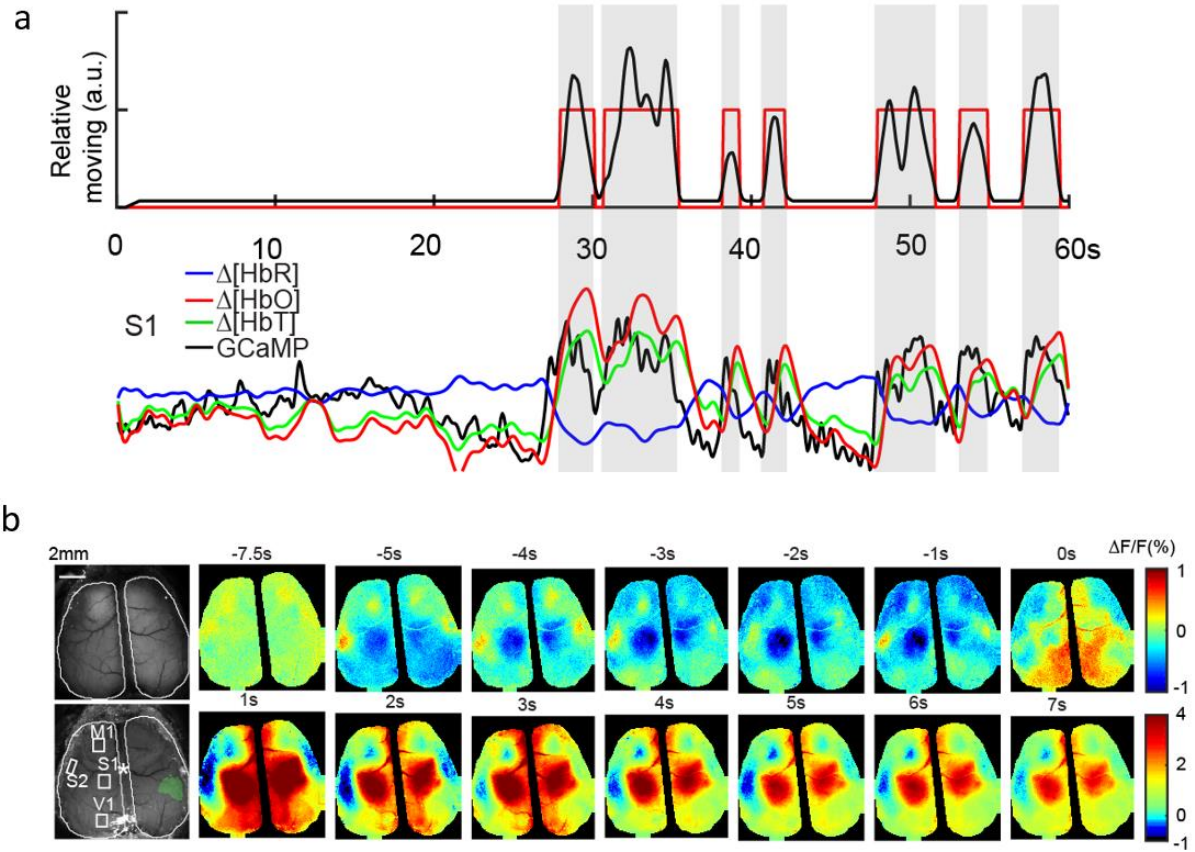


Figure 5. 1 Spatial neural pattern during locomotion. (a) Animal's motion on the tread mill with concurrent GCaMP fluorescence signal and hemodynamics from primary somatosensory region. The shaded regions represent the duration of running. (b) Neural activation pattern before and during locomotion revealed by running-triggered average. 29 running epochs with at least 10s resting before and lasted at least 2s from the same animal were aligned at the onset of the running.

Interestingly, the anti-correlation between S1 and S2 regions appears not only for the duration of locomotion, but also during the preparatory stage before movement started. During the running preparatory stage, the S2 region had an above-average activation while the S1 region displayed a lower level of activity comparing to baseline. Starting around 3s before the running onset, barrel cortex and the secondary motor cortex displayed the activation dynamic opposite to the running as well. The only region that displayed an increase in signal both during preparation and running

stages was the visual cortex, which had a slight activation compared to the time point before starting around 3s before the running onset. Most of the changes in neural signal started around 5s ahead of the running onset, and the neural pattern remained stationary from -10s to -5s.

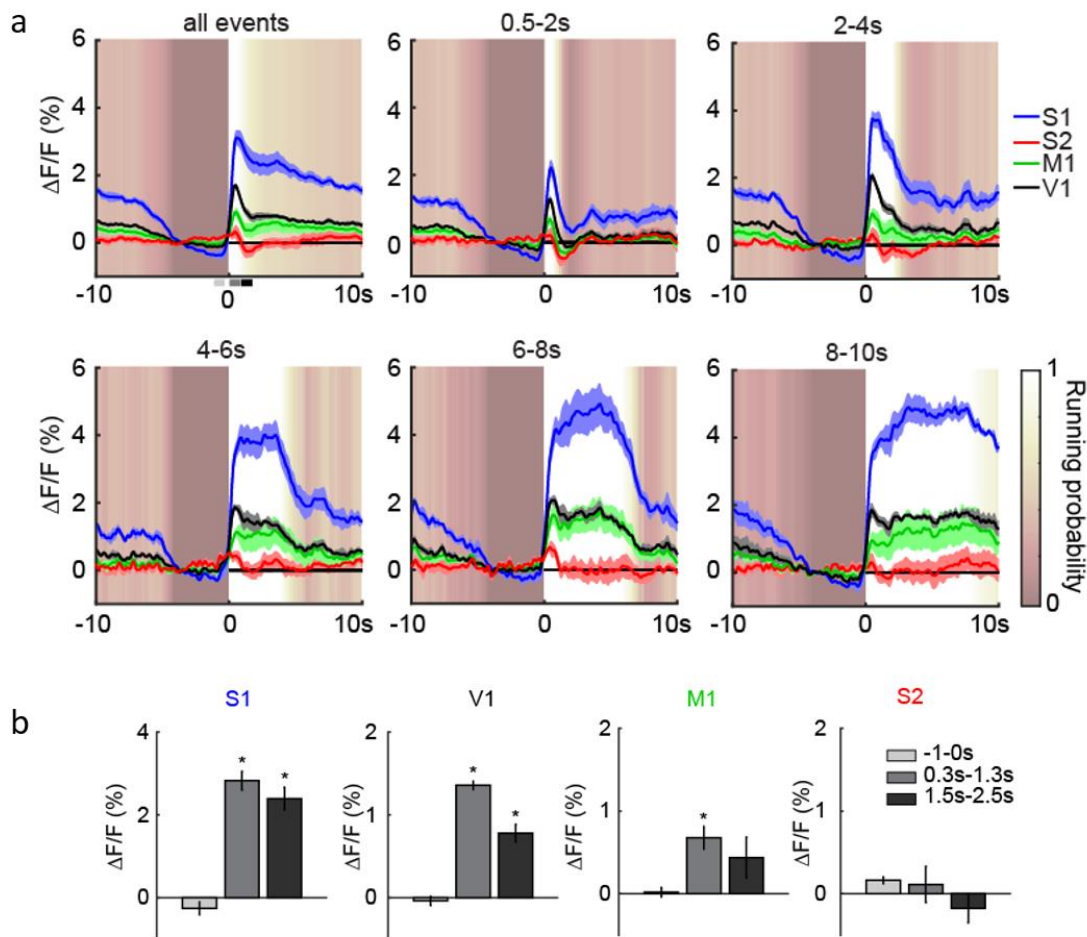


Figure 5. 2 Time courses of neural activity in S1, V1, M1 and S2 before and during locomotion. (a) Averaged time courses of GCaMP fluorescence in S1 (blue), V1 (black), M1 (green) and S2 (red) over 4 animals' weighted running-triggered averaged results. The shaded color represents running probability. The average was also grouped based on running duration and the shaded boundary over timecourses represent weighted standard deviation. Error bounds are weighted standard deviation calculated by bootstrapping with 200 time resampling. (b) Statistical comparison of neural activity before and during locomotion in different regions.

In order to visualize the dynamic changes in each functional brain, time courses of the GCaMP fluorescence in S1, V1, M1 and S2 (ROIs manually selected based on the mouse brain atlas) were averaged across 4 animals, weighted according to the number of identified events (143, 57, 224, and 60 trials respectively). The average across animals and their weighted standard deviation across animals (calculated by bootstrapping technique with 200 times resampling) were plotted 10s before and 10s after locomotion onset (Figure 5. 2 top left). The running epochs from all 4 animals were aligned at the onset of the running and only the trials with the animal being still for 4s prior to the onset were all included. The baseline for each trial was set to be from -4s to -3s, where the animals remained still. The pink color gradient suggests running probability, with -4s to 0s being 0% possibility represented by the darkest shade and 0s to 0.5s being 100% running represented by white background.

The time courses suggest that S1 had the most intense activation in response to locomotion onset and sustained for the duration of running. Both V1 and M1 exhibited a peak at the onset of the running but quickly went back to baseline. The activity in S2 displayed slight activation before the onset and inhibition after the peak associated with the onset. The averaged time courses were also grouped according to the running duration, (0.5-2s, 2-4s, 4-6s, 6-8s and 8-10s) and the features remained very similar regardless of the running duration.

Statistical analysis (Figure 5. 2b) comparing neural signal changes before onset (-1 – 0s), during onset (0.3 – 1.3s) and right after the onset (1.5 – 2.5s) to the baseline were performed on the averaged time courses. With the changes in S1, V1 and M1 during the locomotion onset being statistically significant, signals from S2 have much smaller changes and no significance was found for any changes in this region.

5.4 Regression analysis

The running-triggered average analysis is a good way to summarize the prominent changes during locomotion despite the difference of other influencing factors such as running durations and variability in the movement and signal. However, subtle changes with low amplitude or large variability, such as the activation in S2 region will be canceled out by the averaging process and are more challenging to identify using this method. Further improvements such as aligning regions among animals with standardized brain map registration and evaluating more functional regions across the cortex, are needed to draw a more reliable and robust conclusion. To address these problems, k-means clustering was applied to the spontaneous fluorescence WFOM data to identify functional regions across the cortex and reduce dimensionality. The processed neural data was then fitted to the behavioral state by linear regression models to evaluate the spatiotemporal neural patterns associating with locomotion.

5.4.1 Dimensionality reduction with K-means

After a series of preprocessing steps including down-sampling, GCaMP correction, detrending and brain masking (described in the methods), k-means clustering was applied to the concatenated dataset to further reduce the dimensionality. The 3-dimensional dataset was firstly reshaped into a two-dimensional matrix by disregarding the spatial connections and treating each pixel as an independent observation. The aim of k-means clustering is to reassemble those pixels into several groups based on the similarity among the time courses. Based on the concept of functionally connected networks, each group will be treated as a functional network. The similarity metric used here was Pearson's correlation instead of the traditionally used Euclidian distance so that the differences in scale were standardized. 10 clusters ($K = 10$) were used throughout this analysis and

the initial centroid positions were manually chosen to correspond to 10 functional regions based on mouse atlas (Allen Institute). These 10 regions include primary motor, secondary motor, cingulate, retrosplenial, primary somatosensory for limbs, primary somatosensory for other parts, secondary somatosensory, barrel, primary visual and secondary visual (Figure 5. 3). The numbering of clusters were arranged according to their location from anterior to posterior of the head and the correspondence among sessions and animals were manually adjusted if needed.

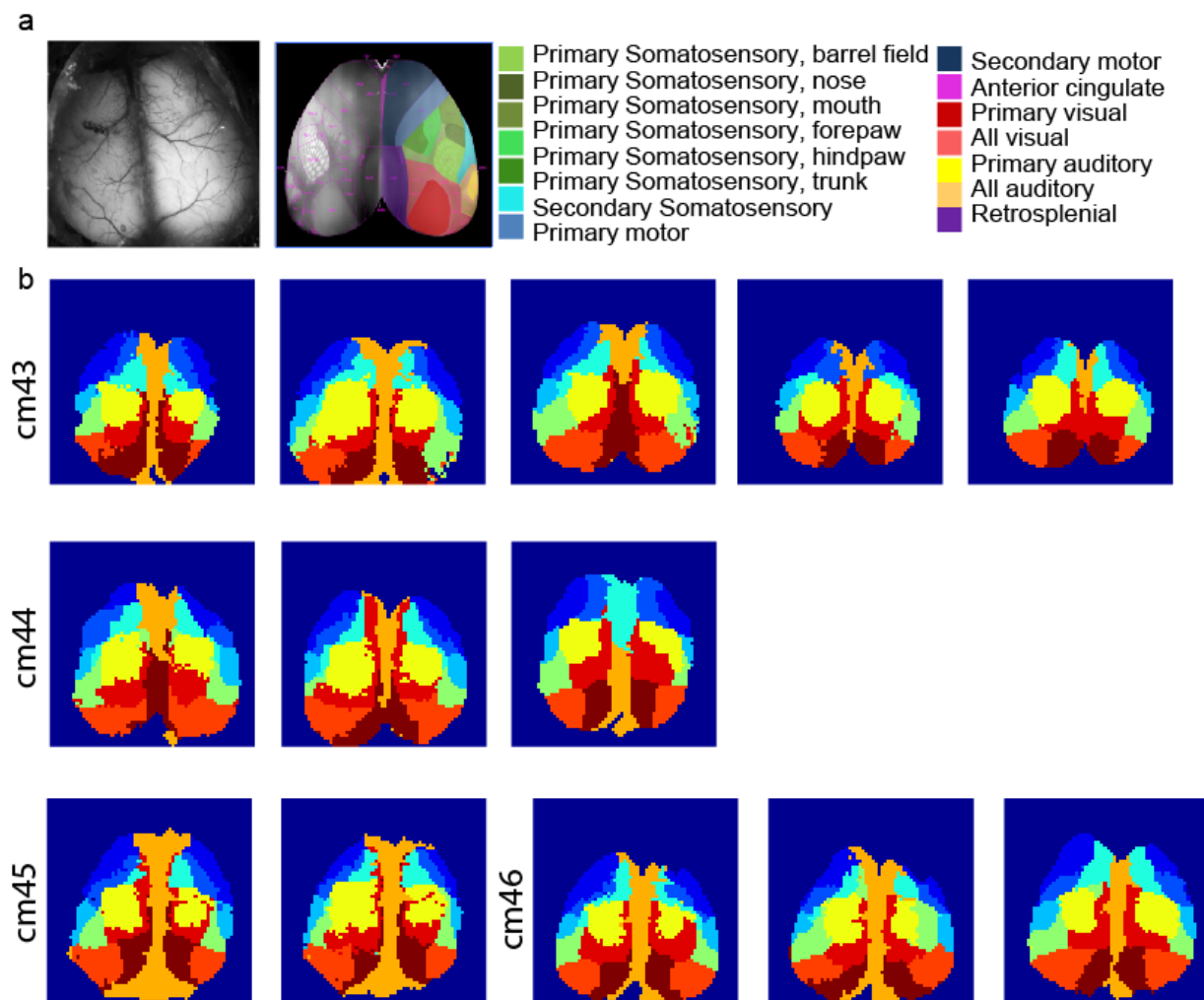


Figure 5. 3 Longitudinal functional maps derived by k-means clustering with $k = 10$. (a) The gray scale image of GCaMP fluorescence image and the standard mouse brain atlas derived from Allen Institute. (b) Logitudinal k-means clustering maps from 4 animals across 13 imaging sessions. $K = 10$ were used for the analysis

The k-means clustering maps on wide-field GCaMP activity from 4 animals and 13 imaging sessions are displayed in Figure 5. 3. The pixels classified into the same group were located in close proximity even though no spatial constrain was applied to k-means, which agrees with our assumption of high synchrony within functional regions. The spatial distribution of the groups also matches the observation we had in previous resting-state studies that the wide-field GCaMP activity is symmetrical across hemispheres. The patterns generated by k-means clustering also demonstrated longitudinal stability and consistency both across imaging sessions and among different animals. Therefore, k-means clustering can reliably identify the functional networks and reduce the dimensionality from 64x64 pixels to 10 features. This analysis also solves the problem of registration among animals by concatenating the centroid of the ordered features across multiple imaging sessions and animals

5.4.2 Prediction of ongoing running

After the pre-processing of k-means clustering, the spatiotemporal GCaMP neural activity was reduced to 10 temporal features and the numbering of clusters were kept consistent according to the location. The first step or the low hanging fruit is to predict the animal's running state based on the current neural activity, since we have observed clear neural activation patterns during running in our previous analysis.

Trials containing resting and spontaneous running from 13 imaging sessions and 4 animals were used and the total length of the dataset lasted 8 hours. Several linear models were applied here to associate behavior with the neural activity. The models were designed to find the interpretable neural patterns and quantify the association between functional regions and movement despite the variability across imaging sessions and animals and noises.

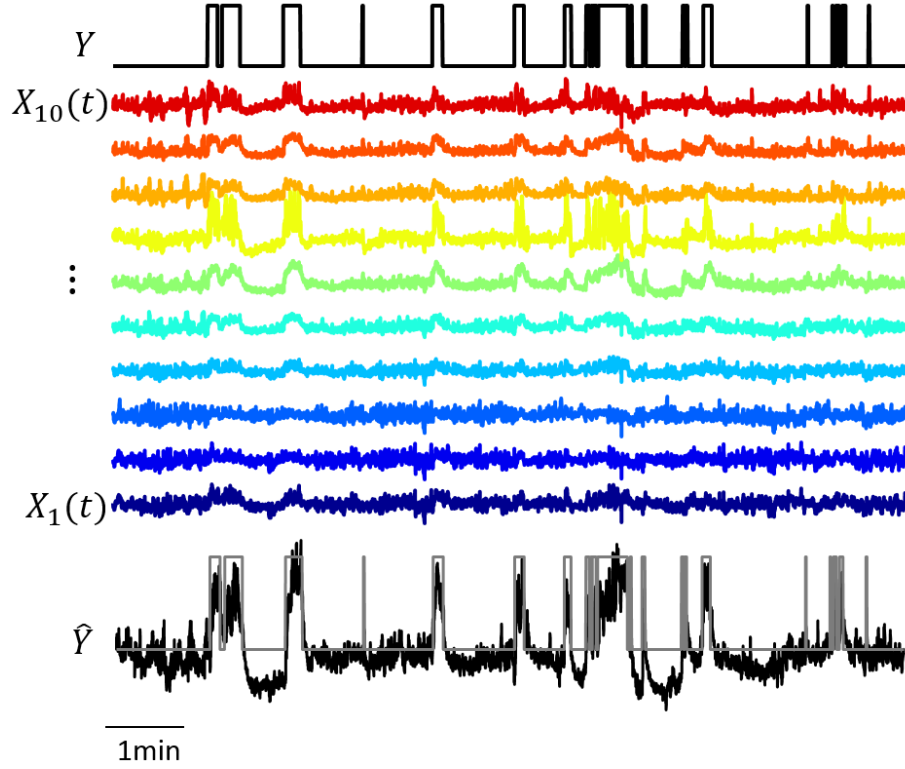


Figure 5. 4 Linear regression model for ongoing behavior prediction. From top to bottom the dependent variable (Y), regressors (X) and the prediction (\hat{Y}) within a 10 min period is illustrated. Running period is labeled as 1 in the dependent variable. The colors of regressors are corresponding to functional regions in k-means map shown in Figure 5. 3. The prediction from simple linear regression is plotted at the bottom accompanied by the observation in gray.

To set up the regression model, each feature from k-means clustering serves as a regressor (X_1, X_2, \dots, X_{10}) and the dependent variable Y is binarized with 1 corresponding to running and 0 corresponding to resting (Figure 5. 4). The predicted value of Y is denoted as \hat{Y} . Therefore, the multinomial linear regression model can be written as:

$$Y(t) = \beta_0 + \beta_1 \cdot X_1(t) + \beta_2 \cdot X_2(t) + \dots + \beta_{10} \cdot X_{10}(t) + e(t)$$

Equation 5. 1

where β is the regression coefficient, t represents the time point and e is the stochastic error term.

The dataset was randomly separated into a training set containing 80% of the data and a test set containing the rest. The model was fitted on the training set with linear regression, logistic regression (with L2 penalty) and ridge regression. Hyper-parameters were determined via 10-fold cross validation. Because the dataset is imbalanced (13.29% of $Y = 1$), the area under the Receiver Operating Characteristic (AUC of ROC) curve was used to evaluate the models. The results calculated from the testing set were shown in Figure 5. 5 and the area under the ROC curve of the three linear models are all around 0.90. The R-squared values of the test set are all around 0.41. Figure 5. 4 also gives an example of the quality of the prediction by showing predicted probability of running (\hat{Y}) accompanied by the measurement (Y). Obvious elevation in the predicted probability of running was observed during the actual running period. The scores from AUC of ROC are all far from the random classifier at 0.5 and these results suggest that the linear model is sufficient to predict the locomotion with neural activity and regularization is not necessary since there's little difference between simple linear regression and regularized linear regression.

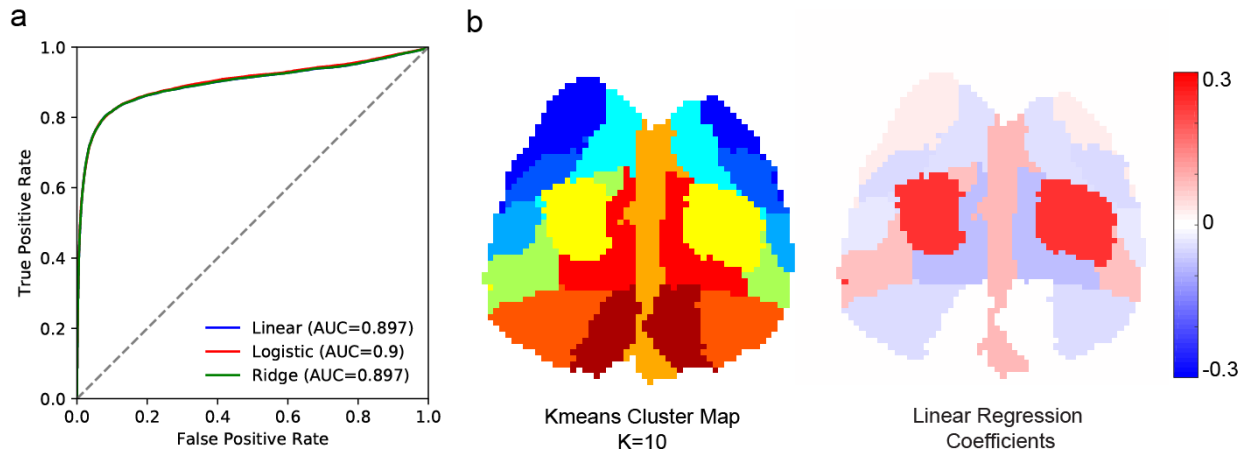


Figure 5. 5 General Linear regression results and weights. (a) The area under the ROC curve from simple linear regression, logistic regression and ridge regression evaluated on the test data set. (b) The regression coefficients from simple linear regression plotted on the functional maps generated by k-means.

Through the regression, each functional region was assigned a β -weight (standardized regression coefficient) which can be both positive and negative and indicates how strongly that region contributes to the locomotion. The coefficients were mapped back to the functional regions and plotted in Figure 5. 5b. Agreeing with previous finding with running-triggered average, the primary somatosensory region (yellow color in k-means map) has the highest coefficient value and positively relates to the locomotion. Even though the coefficients from other regions have smaller amplitudes, the directions generally agree with the running-triggered average maps during locomotion shown in Figure 5. 1b.

In summary, animal's movement can be reliably predicted by the current neural activity taken by WFOM with a linear regression model. The contribution of each functional region towards locomotion is reflected by the value of the regression coefficient.

5.4.3 Prediction of future behavior

Since the previous result confirms that the association between spontaneous movement and regional activation of the cortex can be quantified by the weights of the regression model, we next sought to adapt the mathematical model to explore the spatiotemporal dynamic of neural activity during the preparatory stage preceding the movement.

To extract features during the preparatory stage, the dependent variable (Y) was set to one for 10s before the locomotion onset. This window was intentionally set to be relatively long because the duration of preparation is undetermined for each event since locomotion activity is spontaneous in our setup.

To clean up the information feeding into the model, locomotion events that are shorter than 2s were excluded to eliminate events that might not be intentional. Locomotion events that happened within less than 10s since the last event ended were also excluded in order to maintain sufficient time to observe changes.

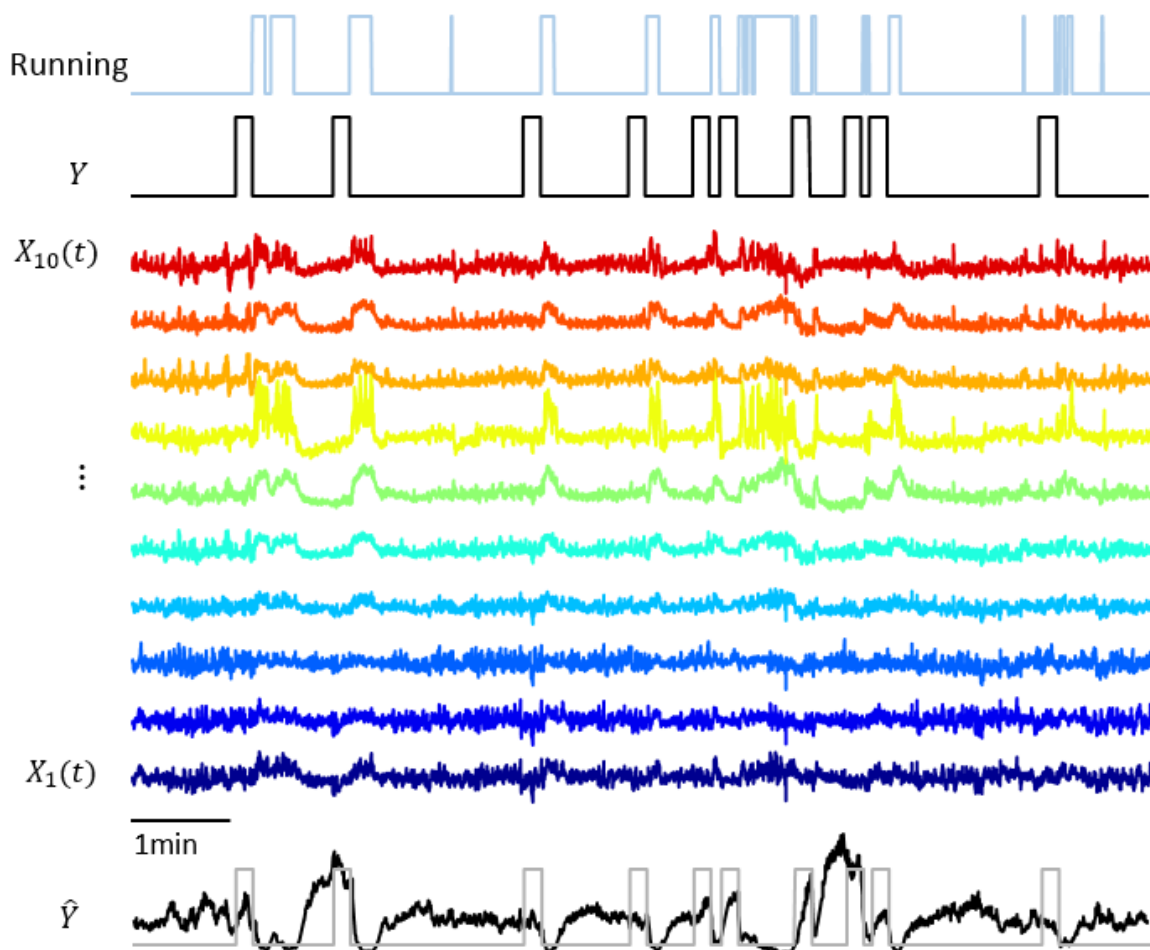


Figure 5. 6 Linear regression model setup for moving preparation. From top to bottom displayed the running state, the dependent variable (Y) featuring the preparatory stage before running onset, regressors (X) and the predicted probability (\hat{Y}) within a 10 min period. The colors of regressors coorespond to functional regions in the k-means map shown in Figure 5. 3. The prediction from simple linear regression is plotted at the bottom accompanied by the observation in gray.

The preparation stage is assumed to have a temporally evolving profile across functional regions across the cortex and the regressors are modified accordingly. Specifically, for a dependent variable at a certain time point $Y(t)$, T frames from all 10 functional regions were all included as regressors. The regression model can be written as:

$$\begin{aligned}
Y(t) = & \beta_0 + \beta_{1,1} \cdot X_1(t-1) + \beta_{1,2} \cdot X_1(t-2) + \dots + \beta_{1,T} \cdot X_1(t-T) \\
& + \beta_{2,1} \cdot X_2(t-1) + \beta_{2,2} \cdot X_2(t-2) + \dots + \beta_{2,T} \cdot X_2(t-T) \\
& \dots \\
& + \beta_{10,1} \cdot X_{10}(t-1) + \beta_{10,2} \cdot X_{10}(t-2) + \dots + \beta_{10,T} \cdot X_{10}(t-T) + e(t)
\end{aligned}$$

Equation 5. 2

This equation can be generalized and simplified as:

$$Y(t) = \beta_0 + \sum_{k=1:K} \sum_{\tau=1:T} \beta_{k,\tau} \cdot X_k(t-\tau) + e(t)$$

Equation 5. 3

The number of regression coefficients (β) will be the product of K and T . According to the observation from the running-triggered average, we used $K = 10$ (number of functional regions) and $T = 50$ (equivalent to 5s, 10 Hz frame rate) and therefore 500 weights were estimated by fitting the data to this model. Note that the neural signals at the current time ($X(t)$) were not included in the model to avoid replicating the pattern observed in the prediction of ongoing movement. Similar to previous model, the dataset was randomly separated into a training set containing 80% of the data and a test set containing the rest. Because of the excessive amount of regressors, lasso regression with L1 penalization of the sparsity is used to facilitate the feature selection. The AUC of ROC of the lasso regression model on the test set is 0.728. Figure 5. 6

included the predicted probability of the preparatory stage accompanied with the 10s window prior to the running onset on the bottom. It's clear that the predicted the preparatory stage (\hat{Y}) and the allotted window for preparatory activity have a good correspondence at some running events and at the other events the neural patterns prior to the running onset cannot be recognized by the model.

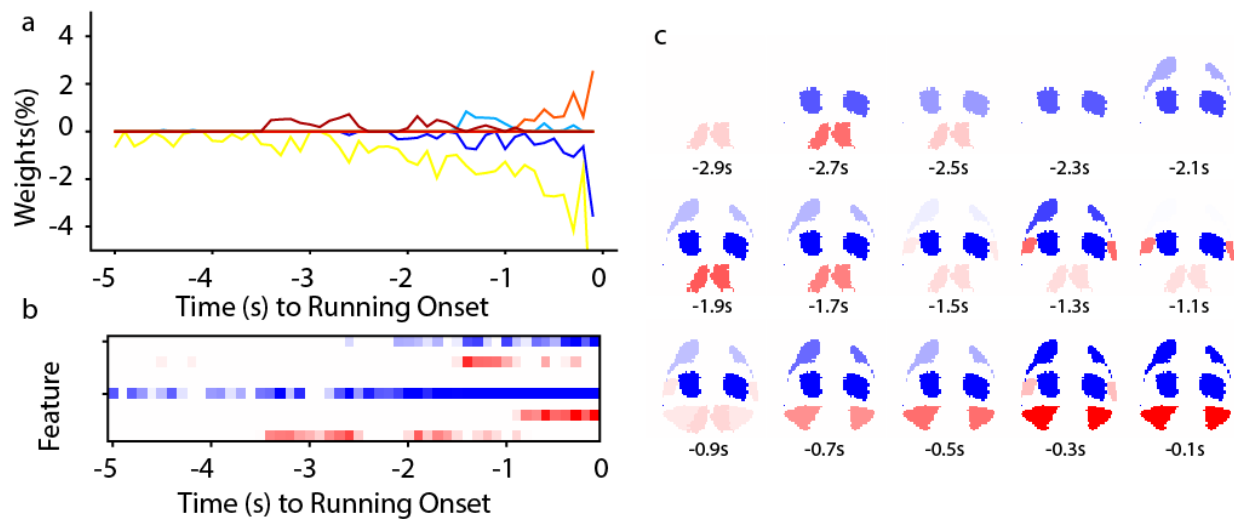


Figure 5. 7 Spatiotemporal pattern of regional neural activity leading towards spontaneous locomotion. (a) The weights of functional regions fitted by ridge regression progress towards the running onset. The coloring of each trace corresponds to the functional region coloring in Figure 5. 3. (b) The weights of functional regions fitted by ridge regression are shown in matrix format. Each row corresponds to one feature clustered by k-means and the order is the same as in Figure 5. 5 and Figure 5. 6. (c) The spatiotemporal progression of the ridge fitted weights.

Another informative aspect of the regression result is to examine and interpret the weights of the spatiotemporal regressors. Figure 5. 7 illustrated the weights generated by the training dataset in several ways. Figure 5. 7a and Figure 5. 7b demonstrate that the weight progression as the time approaching the locomotion onset ($t = 0$). The functional region (feature) that has the most prominent influence to the prediction is the primary somatosensory region is, marked as yellow in Figure 5. 7a and in the fifth feature in Figure 5. 7b. This region consistently displayed negative

weights towards the prediction which corresponds to our previous finding that the S1 was inhibited during the preparatory stage. Besides the deactivation in S1, a series of neural activation pattern was observed across several other functional regions. The start of the information flow started around 3s ahead of the onset in the retrosplenial region with a positive increase. Then at around 2s ahead, the primary motor cortex become involved with an inhibition till the locomotion onset. From -1.5s to -1s, the secondary somatosensory cortex was activated briefly. When the S2 switched off, the visual cortex was the last stop of the preparatory flow and remained active during the last second before the running starts. This flow of information is also displayed spatially in Figure 5. 7c by assigned the weight values back to the functional maps.

Captured by linear regression model with L1 penalty, the flow of information during the preparatory stage before spontaneous locomotion displayed a complex spatiotemporal dynamic involving several functional regions across the cortex. This analysis confirmed the involvement of the functional regions and quantified their spatiotemporal contribution to the moving preparation, despite the fact that activity changes were small as featured by the previous running-triggered average analysis.

5.5 Discussion

In this chapter, I explored the spatiotemporal neural patterns during and preceding the spontaneous locomotion by regression analysis on the fluorescence WFOM data. Our results demonstrated that the animal's current running state can be predicted by a simple linear regression model fitted with the time courses from 10 functional regions on the cortex parcellated by k-means clustering. The contribution of each functional region was captured by the weight coefficient in the model. Additionally, by fitting the temporally extended neural data to the preparatory stage preceding the

locomotion, a spatiotemporal information flow across several brain regions leading towards the spontaneous running was identified. Our results also suggest that spontaneous locomotion recruits organized activations in various brain regions across the entire brain.

In this study, we have chosen the locomotion events happened at the animals' will to be the targeted event. In fact, a set of different behaviors was captured by the monitoring camera from the awake, but head-restrained mouse during the imaging sessions. So far we have quantified the neural patterns associating with animal's running and resting, neural patterns of other behavioral paradigms, such as grooming, whiskering, licking and even falling asleep is already a part of the awake mouse data captured by the powerful WFOM system. In addition to our existing WFOM system, our lab has recently implemented a pupilometer which measures the diameter of the pupil and reflects the attention, alertness and general brain state of the animal. Incorporating this additional information to the cortical neural activity and concurrent behavior, a lot more information can be extracted from this data set.

Another approach of studying behavioral-related neural pattern is to train the animal to perform a set of task under a set of regulation and guidance. For example, delayed response tasks are commonly adopted in studies of decision making and movement planning in rodent models (Erich et al., 2015; Chen et al., 2017). After the initial cue, the animal was trained to perform the task with several seconds delay between the cue and the response. This setup allotted a determined temporal window to observe and intervene the motor preparation stage. Moreover, goal-directed behaviors are thought to allow task-related information (such as expectation, decisions and goals) modulating local computations to shape the interactions among different cortical regions. Specifically, the feedback signals projected from associated cortical regions back to the motor cortex have been proposed to control the flow of information in a flexible manner, and this process

of focusing volitionally driven by the task demand is called “top-down” control (Miller and Cohen, 2001; Buschman and Miller, 2007). Our fluorescence WFOM system is an ideal tool to observe the subtle changes of the complex spatiotemporal patterns modulated by “top-down” signal.

Another application of establishing predictive models of animal’s behavior with neural activity is brain-machine interface (BCI). This technology has been one of the hottest topic in neuroscience for the past decade and traditionally it utilizes electrophysiological recordings to convert brain signals into outputs that communicate a user’s intent (McFarland and Wolpaw, 2011). Researchers were able to realize motor BCIs in rodents, such as controlling robotic arms or prosthetics by deciphering current neural activity in motor cortex (Moritz et al., 2008; Zhou et al., 2010). A lot of studies have devoted to develop robust algorithms to extract useful information from electrophysiological signals. This task is particular challenging because information from single electrode can be highly noisy and variable. Even with the implementation of large scale multi-electrode array, the recording site is limited. The wide-field optical mapping provides recordings of the entire dorsal surface of the cortex and can potentially serve as a good platform of the BCI application in rodent. Our predictive model used in this analysis prioritized in interpretability of weights of regressors. More reliable prediction can be achieved by applying more advanced machine learning techniques, such as Artificial Neural Networks.

Our results reveals the cascade of information across motor, sensory and visual cortex preceding the spontaneous locomotion, however, the regression modeling approach does not imply causality between neural events and locomotion. To test whether the inputs from multiple cortical regions are necessary for the locomotion, experiments with selected regional inhibition induced pharmacologically or optogenetically should be done to each individual functional regions. Recent study by Allen et al. (Allen et al., 2017) tried to address this issue and found that direct inhibition

of frontal cortex prevented the mice from performing the task, which wasn't observed by inhibiting any other functional regions. More detailed analysis identifying the modification of neural dynamics and moving patterns (such as moving precision and response time) should be performed on mice with restricted sensory and visual inputs.

On the other hand, the predicted probability of the preparatory stage shown in Figure 5. 6 also suggest that some locomotion events do not possess the detected spatiotemporal pattern preceding the onset. There are several explanations for this mismatch. Firstly, the events that failed to be predicted by the regression model could be ill-planned or unintentionally triggered by ambient noise or flashing of light during experiment. The spatiotemporal dynamics of neural pattern triggered by salient stimuli are known as “bottom-up” signals and have a completely different representation than the “top-down” signals. Secondly, the small amplitude of the changes in the related regions can be buried by motion artifacts or other noise in an individual event, which leads to a failed detection. Cortical regions responsible for information and integration local computing (such as motor cortex and secondary sensory cortex) usually tend to be composed of neurons with highly variable preference. In the example of delayed response tasks, researchers have identified several groups of neurons depending on their preferences of different phases of the task (Chen et al., 2017). Imaging the neural fluorescence in wide-field integrates the signal from each individual neurons within a region and the sparse firing due to the selectivity of task-specific parameters leads to small fluorescence changes readout. For the same reason, it is also challenging to use fluorescence WFOM to identify behavioral associated features that are located at the same cortical region but originated from different group of cells. Even though the fluorescence WFOM system doesn't have cellular resolution, it can simultaneously survey the dynamics across the entire cortical surface and identify functional regions that are related or of interest, directing a more

targeted and zoomed-in imaging at the individual cell level. In our result, one region of particular interest is the secondary somatosensory region, which activity hasn't been closely studied in terms of motor planning and control. Unlike the awareness of the visual input towards the locomotion preparation, the transient activation in S2 preceding the visual involvement is under appreciated and requires further investigation in terms of its connection and modulating effects towards motor and primary somatosensory region.

Chapter 6

Discussion and Future Work

This thesis investigates and establishes the qualitative relationship between resting-state neural activity and cortical hemodynamics recorded simultaneously using wide-field optical mapping technology combined with the Thy1-GCaMP transgenic mouse line. Beyond observing the spatiotemporal properties of neurovascular coupling in awake animals, the neural activation patterns of the entire bilateral dorsal surface of the mouse cortex can be visualized with the WFOM system. The patterns of bilaterally-symmetric spontaneous neural activity delineate the functional connectivity networks revealed by resting-state fMRI and this resemblance reconfirms the neural basis of functional connectivity. In addition, the thesis also explores the neural pattern from the entire dorsal cortical surface preceding and during locomotion. The following chapter will discuss the observed characteristics of spontaneous neural patterns and several methods for identifying their functional networks. Current findings are provided alongside several recommended directions for further work.

6.1 Identifying the cortical functional networks

From the spontaneous Thy1-GCaMP6f fluorescence data shown previously, several distinct features of the excitatory neuron firing patterns can be observed during resting state: (1) neurons

within a local region behave in a highly synchronized fashion, (2) all the regions that are synchronized are referred to as a functional network and functional networks are bilaterally symmetric, and (3) correlations between networks were frequently observed. Based on these properties, k-means clustering was used to identify functionally connected regions and achieve dimensionality reduction by representing each cluster with their centroids.

Besides k-means clustering, other mathematical approaches have been used for functional connectivity mapping such as seed-based correlation analysis, principal/independent component analysis (PCA and ICA) and non-negative matrix factorization (NMF). These methods have their own merits and limitations when applied to the WFOM fluorescence data. For example, PCA and ICA need minimum input from the user and will not have divergent results on the same dataset due to their different convergence path. Although NMF requires initialization to ensure proper convergence, it allows for overlapping of different functional regions, which harmonizes with the inherent functional organization of the brain (Haueis, 2012). K-means clustering doesn't allow for shared pixels between clusters, but the metric used to measure the similarity between observations can be defined by the users. In the case of detecting functional connectivity Pearson's correlation coefficient was adopted. Regardless of which algorithm was used for identifying functional networks, one common step of this analysis is to check the residual of the reconstructed spatiotemporal dynamics to ensure no critical information is lost during the process.

Using these mathematical methods, functionally connected networks can be derived from both hemodynamic- and neural-based spatiotemporal dynamics. Comparing these networks originating from different sources at various physiological states is essential to the interpretation of resting-state fMRI. One distinction of the GCaMP correlation maps from hemodynamic-based correlation maps is that the range of GCaMP correlation rarely goes negative whereas anti-correlation between

hemodynamic-based functional regions can be more frequently observed (White et al., 2011). This is due to the all-or-nothing property of action potentials, and the dimming of fluorescence caused by inhibition and hyperpolarization won't be reflected as deflection in the same scale as activation. Common preprocessing techniques used in fMRI or hemodynamic-based signal analysis, such as linear regression, global trend removal and filtering at ultra-slow frequencies are likely to produce artifacts if not properly applied to the fluorescence neural data. Care also needs to be taken when comparing the correlation strength of hemodynamic- and neural-based functional correlations. A standardization or normalization process may be necessary to make comparisons.

Identifying functional regions is the first step towards understanding the complicated spatiotemporal neural dynamics in the resting brain. By assuming the activity within each functional region is homogeneous and can be represented by one feature, the seemingly complex spatiotemporal dynamics across the entire cortex can be reconstructed with only a few features. This process not only achieves dimensionality reduction for further analysis, but also reveals the physical organization of brain's functions. Our study of the neural pattern preceding the spontaneous locomotion captured a series of activations across the motor, sensory and visual cortex with a unique temporal sequence. This patterns of spatiotemporal dynamics leading toward running not only demonstrates that even when the animal is not moving, there's an enormous amount of neural activity going on in the brain, but also sets up a good example of the spatiotemporal motifs comprising the spontaneous neural dynamics. Advanced mathematical techniques should be developed to capture and apprehend the neural motifs in the resting brain. The organization and interaction among the motifs will help us interpret the meaning of resting-state neural activity as well as understand their modulatory effects on brain state and behavior.

6.2 Neural activity as a wave

WFOM enables bilateral access to the dorsal surface cortex. As result, interesting dynamics of neural activation, which have been challenging to obtain by electrophysiological recordings, have been visualized. For example, unlike the localized neural pattern found in awake animals, the neural activity under ketamine/xylazine anesthesia are fast and appear as highly regular waves traveling from anterior to posterior at 1Hz. To understand the wave-like activity in the cortex, phase-aligned spectral filtering (PASf), designed by Meng and Zheng for extracting waves that propagated across a field of view, was applied to wide-field GCaMP fluorescence data in both awake and under anesthesia (Meng and Zheng, 2016).

After removing the waves captured by the PASf's first component, the remaining neural activity appears to be more like the localized patterns observed in the awake mouse. Figure 6. 1 illustrates one cycle of the wave moving from anterior to posterior. NMF decomposition was then applied to the residual signal after wave removal to visualize the recovery of individual functional regions that had been masked by the dominating waves. Time courses of the raw data and the wave extracted by PASf from the primary somatosensory region were plotted together to visualize the regularity of the repeated waves across the cortex.

To further investigate the wave representation in hemodynamics and in awake animals, PASf was applied to the ΔHbT and GCaMP fluorescence changes simultaneously acquired from resting and awake animal. The PASf was designed to decompose a 3-dimensional signal into continuous waves traveling across the image with various frequencies. Though the first component PASf isolated from 0.4Hz low-pass filtered GCaMP signals in awake animals (Figure 6. 2) were not as fast or regular as those in anesthetized animals, the direction of propagation from anterior to

posterior remained the same. The same wave was able to be identified by PASF's first component from ΔHbT .

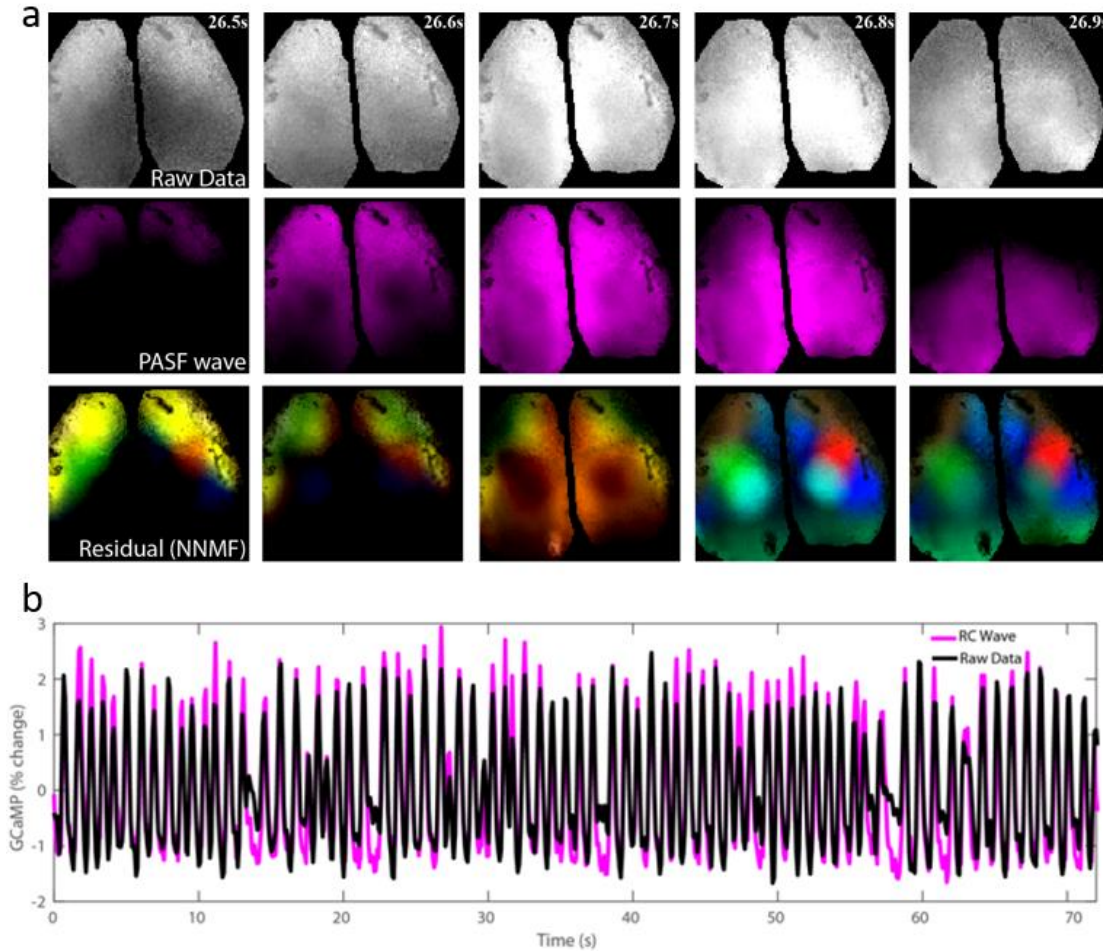
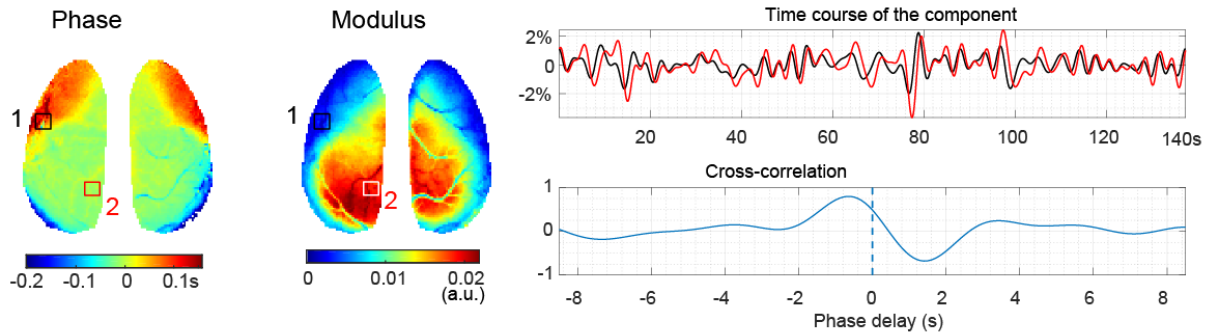


Figure 6. 1 Phase-aligned spectral filtering (PASF) detected waves in GCaMP fluorescence activity acquired under Ketamine anesthesia. (a) From top to bottom are the raw data, the wave detected by PASF's first component and their difference. The residual of the signal was decomposed and reconstructed by NMF, showcasing the recovery of the underlying functional networks. (b) Time course of the raw GCaMP data accompanied with the wave extracted by the PASF in the primary somatosensory region.

Even though the neural activation pattern in awake animals was previously characterized as independent localized regions, this exploration approximating neural activity as a wave-like propagation using PASF does not necessarily contradict the initial observations and assumptions.

In fact, the waves detected by PASF suggest that there exists an internal sequence which organizes different brain regions to activate in turn rather than to fire at random. This sequencing hierarchy might have various modulation effects and representations at different physiological state. It has been primarily observed and reported during sleep or under anesthesia (Nir et al., 2011; Hahn et al., 2012) because the propagation of waves from anterior to posterior is most stable and dominant in those states. These results beget further of questions about where this sequence of activation is formed. Current opinions on this topic have been largely controversial: some studies have implicated thalamic inputs as the governing source of cortical waves (Sheroziya and Timofeev, 2014; Mitra et al., 2018), while others have suggested that UP states are generated in layer 5

(a) GCaMP lowpass at 0.4Hz, 1st component of PASF



(b) Δ HbT, 1st component of PASF

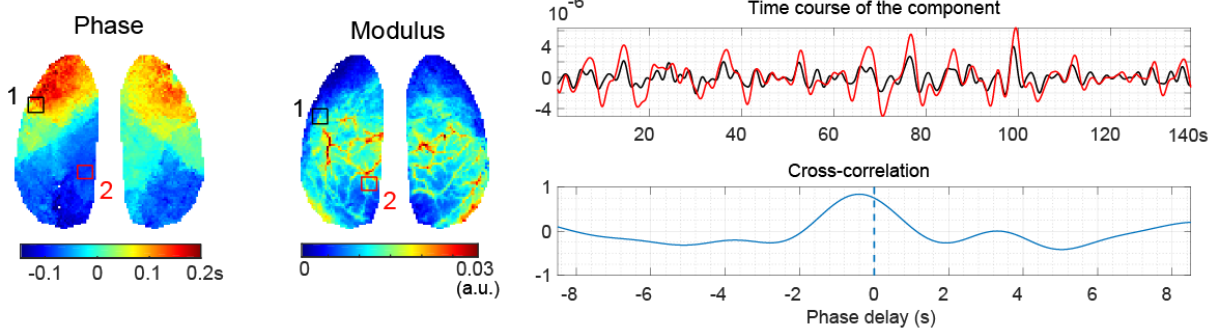


Figure 6. 2 PASF applied to (a) neural and (b) hemodynamic data acquired from an awake animal. The phase and modulus distribution of the first component are illustrated on the left. Time courses of the component from two regions of interest (1-black, 2-red) and their cross-correlation spectrum are plotted on the right.

neurons (Chauvette et al., 2010; Lorincz et al., 2015) and propagate through local neural circuitry (Mohajerani et al., 2010; Stroh et al., 2013; Townsend et al., 2015). The physiological impact of the propagating waves is not well understood as well. The waves have been associated with memory consolidation (Destexhe and Contreras, 2006), and shaping responses to incoming stimulation (Petersen et al., 2003). To address these questions, further studies utilizing PASF and the whole cortex accessibility provided by WFOM are needed to qualitatively assess and compare the cortical wave propagation under various conditions, and to evaluate its impact on physiology and behavior.

6.3 State-dependent pattern

Previously, we have established methods to evaluate the correlation between neural and hemodynamics under both awake and anesthetized states. Even though the correlation is generally high, variance in the degree of the correlation between neural and hemodynamic activity was identified across trials within one imaging session. One example of this phenomenon is illustrated in Figure 6. 3, where trials from the same acute experiment were plotted chronologically according to the time since anesthesia induction. The time courses clearly illustrate that the density and frequency of neural activity varied over time. In the middle time points, the neural firing events were dense and regular, leading to a flat HbT prediction after convolving with an HRF. While this prediction reflected an accurate representation of the cortical hemodynamics, the correlation measurement underestimated the coupling due to the presence of motion artifacts that overwhelmed the small fluctuations in HbT. Towards the end of the experiments, the neural activity transitioned into a state with alternating grouped neural firing and total quiescence, which is known as burst suppression or Up/Down state. Even though the hemodynamics still truthfully

represented the underlying neural activity, during the Up/Down state the global synchronization of the neural activity changes the appearance of functional connectivity (Liu et al., 2011).

Shifting of brain state is not only induced by anesthesia, but has also been found in awake and behaving animals (Gentet et al., 2010; Mohajerani et al., 2010). Continued investigation on inferring brain state in awake animals and evaluating its interactions with brain networks and behavior patterns has already started in my lab.

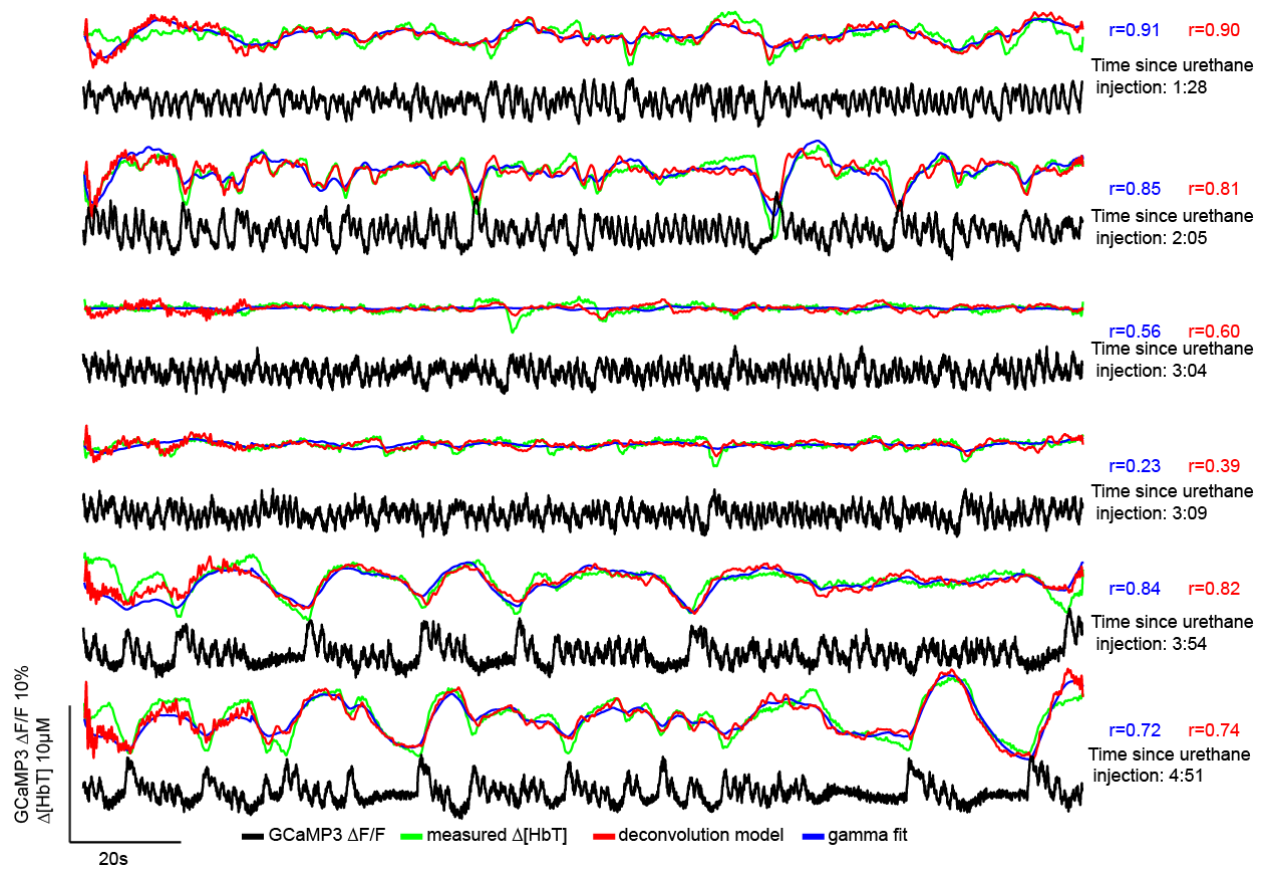


Figure 6. 3 State-dependent neural activity and neurovascular coupling in urethane-anesthetized Thy1-

GCaMP3 mice. Trials were captured within a 5-hour acute experiment of the same animal. Plots show time courses of GCaMP fluorescence, measured $\Delta[\text{HbT}]$ and its predictions from the same somatosensory region ordered chronologically. Convolution and gamma-variate fitting traces and correlation values are shown in red and blue respectively.

6.4 Frequency dependence of functional connectivity

In the earlier chapters, we have established that the neural signal from GCaMP6f and hemodynamics have different frequency representations and their correspondence occurs at low frequency $<0.4\text{Hz}$. Identifying this frequency band is essential to the interpretation of fMRI results, which only associate with neural activation at low frequency. However, we also observed significant amount of variation in GCaMP neural activity beyond 0.4Hz (Figure 6. 4b). In order to investigate the information contained in the higher frequencies of the GCaMP signal, a correlation analysis was done on raw, low-pass filtered and high-pass filtered data (Figure 6. 4).

Correlation analysis was performed on each pair of pixels across the brain region within the field of view and the results were illustrated as the correlation matrix. To better visualize the functional regions and symmetry across hemispheres, the pixels were sorted according to the order of k-means clustered functional regions with left and right side respectively. In the correlation matrix of the unfiltered GCaMP fluorescence signal, the diagonals of the top right and bottom left quadrants have values close to one which indicates good bilateral symmetry. After low-pass filtering, the correlation matrix of the remaining signal, which represents the information that can be picked up by fMRI, has similar structure within and across functional regions as that of the full spectrum. This is consistent with our previous findings that the spontaneous fluctuations in hemodynamics is driven by local neural activity. However, the useful information contained in the GCaMP fluorescence signal extends beyond 0.4Hz . After removing the low frequency component in the GCaMP signal, the bilateral symmetry and functional connectivity remain in the correlation matrix.

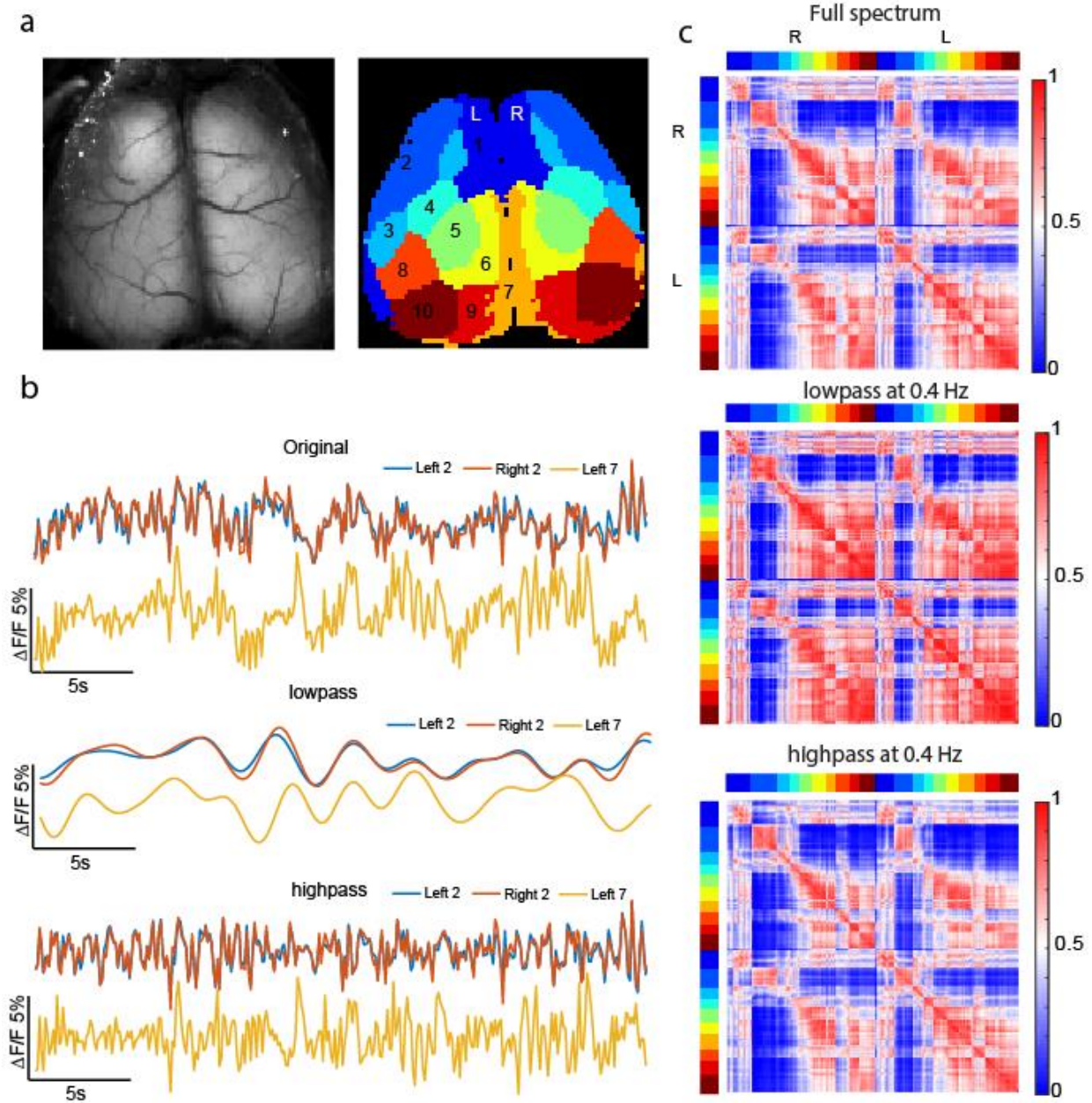


Figure 6. 4 Neural correlation analysis at different frequency band. (a) Shows the gray scale image of GCaMP fluorescence image and k-means clustering map with $k = 10$. (b) Time courses of the raw, 0.4Hz lowpass filtered and 0.4Hz highpass filtered signal from region 2 and 7. (c) Pearson's correlation maxtrix with all the pixels at various frequency band. The pixels were sorted according to the numbering of k-means clustering and pixels from right and left hemispheres were ordered separately.

Further study is needed to interpret the physiological meaning of the high frequency component in the GCaMP fluorescence signal and to explore potential neural patterns and features that not reflected by fMRI. However, care should be taken when filtering the GCaMP fluorescence signal at different frequency bands. Unlike EEG and ECoG which sums over electrical signals from a variety of neural processes, GCaMP fluorescence only reports the intracellular calcium dynamics of the excitatory neurons, which is essentially equivalent to spatiotemporally integrated multiunit activity convolved with single cell calcium kinetics. This leads to a different power distribution across frequencies, and directly applying traditional frequency separation strategies, such as delta band at 1-4Hz, will not be as meaningful and effective as in EEG analysis.

References

- Akerboom J et al. (2013) Genetically encoded calcium indicators for multi-color neural activity imaging and combination with optogenetics. *Frontiers in Molecular Neuroscience* 6.
- Allen WE, Kauvar IV, Chen MZ, Richman EB, Yang SJ, Chan K, Gradinaru V, Deverman BE, Luo L, Deisseroth K (2017) Global Representations of Goal-Directed Behavior in Distinct Cell Types of Mouse Neocortex. *Neuron* 94:891-907 e896.
- Anand A, Li Y, Wang Y, Wu J, Gao S, Bukhari L, Mathews VP, Kalnin A, Lowe MJ (2005) Activity and connectivity of brain mood regulating circuit in depression: a functional magnetic resonance study. *Biological psychiatry* 57:1079-1088.
- Anenberg E, Chan AW, Xie Y, LeDue JM, Murphy TH (2015) Optogenetic Stimulation of GABA Neurons can Decrease Local Neuronal Activity While Increasing Cortical Blood Flow. *Journal of Cerebral Blood Flow & Metabolism* 35:1579-1586.
- Ayaz A, Saleem AB, Scholvinck ML, Carandini M (2013) Locomotion controls spatial integration in mouse visual cortex. *Curr Biol* 23:890-894.
- Beckmann CF, DeLuca M, Devlin JT, Smith SM (2005) Investigations into resting-state connectivity using independent component analysis. *Philos Trans R Soc Lond B Biol Sci* 360:1001-1013.
- Bekar LK, Wei HS, Nedergaard M (2012) The locus coeruleus-norepinephrine network optimizes coupling of cerebral blood volume with oxygen demand. *J Cereb Blood Flow Metab* 32:2135-2145.
- Berens P, Keliris GA, Ecker AS, Logothetis NK, Tolias AS (2008) Feature selectivity of the gamma-band of the local field potential in primate primary visual cortex. *Front Neurosci* 2:199-207.
- Berwick J, Johnston D, Jones M, Martindale J, Martin C, Kennerley AJ, Redgrave P, Mayhew JE (2008) Fine detail of neurovascular coupling revealed by spatiotemporal analysis of the hemodynamic response to single whisker stimulation in rat barrel cortex. *Journal of neurophysiology* 99:787-798.
- Bevilacqua F, Berger AJ, Cerussi AE, Jakubowski D, Tromberg BJ (2000) Broadband absorption spectroscopy in turbid media by combined frequency-domain and steady-state methods. *Applied optics* 39:6498-6507.
- Biswal B, Yetkin FZ, Haughton VM, Hyde JS (1995) Functional connectivity in the motor cortex of resting human brain using echo-planar MRI. *Magn Reson Med* 34:537-541.
- Boorman L, Harris S, Bruyns-Haylett M, Kennerley A, Zheng Y, Martin C, Jones M, Redgrave P, Berwick J (2015) Long-latency reductions in gamma power predict hemodynamic changes that underlie the negative BOLD signal. *J Neurosci* 35:4641-4656.
- Bouchard MB, Chen BR, Burgess SA, Hillman EM (2009) Ultra-fast multispectral optical imaging of cortical oxygenation, blood flow, and intracellular calcium dynamics. *Optics express* 17:15670-15678.

- Boynton GM, Engel SA, Glover GH, Heeger DJ (1996) Linear Systems Analysis of Functional Magnetic Resonance Imaging in Human V1. *The Journal of Neuroscience* 16:4207-4221.
- Brookes MJ, Woolrich M, Luckhoo H, Price D, Hale JR, Stephenson MC, Barnes GR, Smith SM, Morris PG (2011) Investigating the electrophysiological basis of resting state networks using magnetoencephalography. *Proc Natl Acad Sci U S A* 108:16783-16788.
- Brown RE, Basheer R, McKenna JT, Strecker RE, McCarley RW (2012) Control of sleep and wakefulness. *Physiol Rev* 92:1087-1187.
- Bruyns-Haylett M, Harris S, Boorman L, Zheng Y, Berwick J, Jones M (2013) The resting-state neurovascular coupling relationship: rapid changes in spontaneous neural activity in the somatosensory cortex are associated with haemodynamic fluctuations that resemble stimulus-evoked haemodynamics. *Eur J Neurosci* 38:2902-2916.
- Buckner RL, Krienen FM, Yeo BT (2013) Opportunities and limitations of intrinsic functional connectivity MRI. *Nat Neurosci* 16:832-837.
- Buschman TJ, Miller EK (2007) Top-down versus bottom-up control of attention in the prefrontal and posterior parietal cortices. *Science* 315:1860-1862.
- Carandini M, Shimaoka D, Rossi LF, Sato TK, Benucci A, Knopfel T (2015) Imaging the awake visual cortex with a genetically encoded voltage indicator. *J Neurosci* 35:53-63.
- Cardoso MM, Sirotin YB, Lima B, Glushenkova E, Das A (2012) The neuroimaging signal is a linear sum of neurally distinct stimulus- and task-related components. *Nat Neurosci* 15:1298-1306.
- Cauli B, Tong XK, Rancillac A, Serluca N, Lambolez B, Rossier J, Hamel E (2004) Cortical GABA interneurons in neurovascular coupling: relays for subcortical vasoactive pathways. *J Neurosci* 24:8940-8949.
- Chalfie M, Tu Y, Euskirchen G, Ward WW, Prasher DC (1994) Green Fluorescent Protein as a Marker for Gene-Expression. *Science* 263:802-805.
- Chauvette S, Volgushev M, Timofeev I (2010) Origin of active states in local neocortical networks during slow sleep oscillation. *Cereb Cortex* 20:2660-2674.
- Chen BR, Kozberg MG, Bouchard MB, Shaik MA, Hillman EM (2014) A critical role for the vascular endothelium in functional neurovascular coupling in the brain. *J Am Heart Assoc* 3:e000787.
- Chen Q, Cichon J, Wang W, Qiu L, Lee SJ, Campbell NR, Destefino N, Goard MJ, Fu Z, Yasuda R, Looger LL, Arenkiel BR, Gan WB, Feng G (2012) Imaging neural activity using Thy1-GCaMP transgenic mice. *Neuron* 76:297-308.
- Chen TW, Li N, Daie K, Svoboda K (2017) A Map of Anticipatory Activity in Mouse Motor Cortex. *Neuron* 94:866-879 e864.
- Chen TW, Wardill TJ, Sun Y, Pulver SR, Renninger SL, Baohan A, Schreiter ER, Kerr RA, Orger MB, Jayaraman V, Looger LL, Svoboda K, Kim DS (2013) Ultrasensitive fluorescent proteins for imaging neuronal activity. *Nature* 499:295-300.
- Cisek P, Kalaska JF (2010) Neural mechanisms for interacting with a world full of action choices. *Annu Rev Neurosci* 33:269-298.

- Danquah M (2017) Review of Handbook of Porphyrin Science with Application to Chemistry, Physics, Materials Science, Engineering, Biology and Medicine. Volume 40: Nanoorganization of Porphyrinoids Handbook of Porphyrin Science with Application to Chemistry, Physics, Materials Science, Engineering, Biology and Medicine. Volume 40: Nanoorganization of Porphyrinoids . Edited by Karl. M. Kadish, Kevin M. Smith, and Roger Guilard . World Scientific Publishing Co. , Singapore . 2016 . Hardcover, 304 pp. \$1850.00 (set). ISBN 978-981-3140-76-9 (set). J Nat Prod 80:1232.
- De Luca M, Beckmann CF, De Stefano N, Matthews PM, Smith SM (2006) fMRI resting state networks define distinct modes of long-distance interactions in the human brain. *Neuroimage* 29:1359-1367.
- Destexhe A, Contreras D (2006) Neuronal computations with stochastic network states. *Science* 314:85-90.
- Destexhe A, Contreras D, Steriade M (1999) Spatiotemporal analysis of local field potentials and unit discharges in cat cerebral cortex during natural wake and sleep states. *J Neurosci* 19:4595-4608.
- Devor A, Dunn AK, Andermann ML, Ulbert I, Boas DA, Dale AM (2003) Coupling of total hemoglobin concentration, oxygenation, and neural activity in rat somatosensory cortex. *Neuron* 39:353-359.
- Devor A, Tian P, Nishimura N, Teng IC, Hillman EMC, Narayanan SN, Ulbert I, Boas DA, Kleinfeld D, Dale AM (2007) Suppressed neuronal activity and concurrent arteriolar vasoconstriction may explain negative BOLD. *J Neurosci* 27:4452-4459.
- Dombeck DA, Khabbaz AN, Collman F, Adelman TL, Tank DW (2007) Imaging large-scale neural activity with cellular resolution in awake, mobile mice. *Neuron* 56:43-57.
- Drew PJ, Shih AY, Kleinfeld D (2011) Fluctuating and sensory-induced vasodynamics in rodent cortex extend arteriole capacity. *Proc Natl Acad Sci U S A* 108:8473-8478.
- Drew PJ, Shih AY, Driscoll JD, Knutsen PM, Blinder P, Davalos D, Akassoglou K, Tsai PS, Kleinfeld D (2010) Chronic optical access through a polished and reinforced thinned skull. *Nat Methods* 7:981-984.
- Eichling JO, Raichle ME, Grubb RL, Jr., Larson KB, Ter-Pogossian MM (1975) In vivo determination of cerebral blood volume with radioactive oxygen-15 in the monkey. *Circ Res* 37:707-714.
- Ekstrom A (2010) How and when the fMRI BOLD signal relates to underlying neural activity: the danger in dissociation. *Brain Res Rev* 62:233-244.
- Erlich JC, Brunton BW, Duan CA, Hanks TD, Brody CD (2015) Distinct effects of prefrontal and parietal cortex inactivations on an accumulation of evidence task in the rat. *Elife* 4.
- Ferezou I, Haiss F, Gentet LJ, Aronoff R, Weber B, Petersen CC (2007) Spatiotemporal dynamics of cortical sensorimotor integration in behaving mice. *Neuron* 56:907-923.
- Fox MD, Raichle ME (2007) Spontaneous fluctuations in brain activity observed with functional magnetic resonance imaging. *Nat Rev Neurosci* 8:700-711.

- Fox MD, Snyder AZ, Vincent JL, Corbetta M, Van Essen DC, Raichle ME (2005) The human brain is intrinsically organized into dynamic, anticorrelated functional networks. *Proc Natl Acad Sci U S A* 102:9673-9678.
- Gentet LJ, Avermann M, Matyas F, Staiger JF, Petersen CC (2010) Membrane potential dynamics of GABAergic neurons in the barrel cortex of behaving mice. *Neuron* 65:422-435.
- Gong Y, Huang C, Li JZ, Grewe BF, Zhang Y, Eismann S, Schnitzer MJ (2015) High-speed recording of neural spikes in awake mice and flies with a fluorescent voltage sensor. *Science* 350:1361-1366.
- Grandjean J, Schroeter A, Batata I, Rudin M (2014) Optimization of anesthesia protocol for resting-state fMRI in mice based on differential effects of anesthetics on functional connectivity patterns. *Neuroimage* 102 Pt 2:838-847.
- Hahn TT, McFarland JM, Berberich S, Sakmann B, Mehta MR (2012) Spontaneous persistent activity in entorhinal cortex modulates cortico-hippocampal interaction in vivo. *Nat Neurosci* 15:1531-1538.
- Hamalainen M, Hari R, Ilmoniemi RJ, Knuutila J, Lounasmaa OV (1993) Magnetoencephalography - Theory, Instrumentation, and Applications to Noninvasive Studies of the Working Human Brain. *Rev Mod Phys* 65:413-497.
- Handwerker DA, Ollinger JM, D'Esposito M (2004) Variation of BOLD hemodynamic responses across subjects and brain regions and their effects on statistical analyses. *Neuroimage* 21:1639-1651.
- Haueis P (2012) The fuzzy brain. Vagueness and mapping connectivity of the human cerebral cortex. *Front Neuroanat* 6:37.
- Heeger DJ, Ress D (2002) What does fMRI tell us about neuronal activity? *Nat Rev Neurosci* 3:142-151.
- Heim N, Garaschuk O, Friedrich MW, Mank M, Milos RI, Kovalchuk Y, Konnerth A, Griesbeck O (2007) Improved calcium imaging in transgenic mice expressing a troponin C-based biosensor. *Nat Methods* 4:127-129.
- Hewson-Stoate N, Jones M, Martindale J, Berwick J, Mayhew J (2005) Further nonlinearities in neurovascular coupling in rodent barrel cortex. *Neuroimage* 24:565-574.
- Hillman EM (2007) Optical brain imaging in vivo: techniques and applications from animal to man. *Journal of biomedical optics* 12:051402.
- Hillman EM (2014) Coupling mechanism and significance of the BOLD signal: a status report. *Annu Rev Neurosci* 37:161-181.
- Hillman EM, Devor A, Bouchard MB, Dunn AK, Krauss GW, Skoch J, Bacsikai BJ, Dale AM, Boas DA (2007) Depth-resolved optical imaging and microscopy of vascular compartment dynamics during somatosensory stimulation. *Neuroimage* 35:89-104.
- Huo BX, Smith JB, Drew PJ (2014) Neurovascular coupling and decoupling in the cortex during voluntary locomotion. *J Neurosci* 34:10975-10981.
- Issa JB, Haeffele BD, Agarwal A, Bergles DE, Young ED, Yue DT (2014) Multiscale optical Ca²⁺ imaging of tonal organization in mouse auditory cortex. *Neuron* 83:944-959.

- Jones M, Hewson-Stoate N, Martindale J, Redgrave P, Mayhew J (2004) Nonlinear coupling of neural activity and CBF in rodent barrel cortex. *Neuroimage* 22:956-965.
- Khakh BS, Sofroniew MV (2015) Diversity of astrocyte functions and phenotypes in neural circuits. *Nat Neurosci* 18:942-952.
- Kozberg MG, Ma Y, Shaik MA, Kim SH, Hillman EM (2016) Rapid Postnatal Expansion of Neural Networks Occurs in an Environment of Altered Neurovascular and Neurometabolic Coupling. *J Neurosci* 36:6704-6717.
- Kyathanahally SP, Jia H, Pustovyy OM, Waggoner P, Beyers R, Schumacher J, Barrett J, Morrison EE, Salibi N, Denney TS, Vodyanoy VJ, Deshpande G (2014) Anterior-posterior dissociation of the default mode network in dogs. *Brain structure & function*.
- Li JM, Bentley WJ, Snyder LH (2015) Functional connectivity arises from a slow rhythmic mechanism. *Proceedings of the National Academy of Sciences* 112:E2527-E2535.
- Lima B, Cardoso MM, Sirotin YB, Das A (2014) Stimulus-related neuroimaging in task-engaged subjects is best predicted by concurrent spiking. *J Neurosci* 34:13878-13891.
- Liu X, Zhu XH, Zhang Y, Chen W (2011) Neural origin of spontaneous hemodynamic fluctuations in rats under burst-suppression anesthesia condition. *Cereb Cortex* 21:374-384.
- Liu X, Zhu XH, Zhang Y, Chen W (2013) The change of functional connectivity specificity in rats under various anesthesia levels and its neural origin. *Brain Topogr* 26:363-377.
- Logothetis NK (2008) What we can do and what we cannot do with fMRI. *Nature* 453:869-878.
- Logothetis NK, Murayama Y, Augath M, Steffen T, Werner J, Oeltermann A (2009) How not to study spontaneous activity. *Neuroimage* 45:1080-1089.
- Lorincz ML, Gunner D, Bao Y, Connelly WM, Isaac JT, Hughes SW, Crunelli V (2015) A distinct class of slow (~0.2-2 Hz) intrinsically bursting layer 5 pyramidal neurons determines UP/DOWN state dynamics in the neocortex. *J Neurosci* 35:5442-5458.
- Ma H, Harris S, Rahmani R, Lacefield CO, Zhao M, Daniel AG, Zhou Z, Bruno RM, Berwick J, Schwartz TH (2014) Wide-field in vivo neocortical calcium dye imaging using a convection-enhanced loading technique combined with simultaneous multiwavelength imaging of voltage-sensitive dyes and hemodynamic signals. *Neurophotonics* 1:015003.
- Ma Y, Shaik MA, Kozberg MG, Kim SH, Portes JP, Timerman D, Hillman EM (2016a) Resting-state hemodynamics are spatiotemporally coupled to synchronized and symmetric neural activity in excitatory neurons. *Proc Natl Acad Sci U S A* 113:E8463-E8471.
- Ma Y, Shaik MA, Kim SH, Kozberg MG, Thibodeaux DN, Zhao HT, Yu H, Hillman EM (2016b) Wide-field optical mapping of neural activity and brain haemodynamics: considerations and novel approaches. *Philos Trans R Soc Lond B Biol Sci* 371.
- Madsen MT (1992) A Simplified Formulation of the Gamma Variate Function. *Phys Med Biol* 37:1597-1600.
- Magri C, Schridde U, Murayama Y, Panzeri S, Logothetis NK (2012) The amplitude and timing of the BOLD signal reflects the relationship between local field potential power at different frequencies. *J Neurosci* 32:1395-1407.

- Malonek D, Grinvald A (1996) Interactions between electrical activity and cortical microcirculation revealed by imaging spectroscopy: implications for functional brain mapping. *Science* 272:551-554.
- Martin C, Martindale J, Berwick J, Mayhew J (2006) Investigating neural-hemodynamic coupling and the hemodynamic response function in the awake rat. *Neuroimage* 32:33-48.
- Mason MG, Nicholls P, Cooper CE (2014) Re-evaluation of the near infrared spectra of mitochondrial cytochrome c oxidase: Implications for non invasive in vivo monitoring of tissues. *Biochimica et biophysica acta* 1837:1882-1891.
- Mateo C, Knutsen PM, Tsai PS, Shih AY, Kleinfeld D (2017) Entrainment of Arteriole Vasomotor Fluctuations by Neural Activity Is a Basis of Blood-Oxygenation-Level-Dependent "Resting-State" Connectivity. *Neuron* 96:936-948 e933.
- Mayevsky A, Chance B (1982) Intracellular oxidation-reduction state measured in situ by a multichannel fiber-optic surface fluorometer. *Science* 217:537-540.
- McFarland DJ, Wolpaw JR (2011) Brain-Computer Interfaces for Communication and Control. *Commun ACM* 54:60-66.
- Meng L, Zheng T (2016) Phase-Aligned Spectral Filtering for Decomposing Spatiotemporal Dynamics. *arXiv* 1604.
- Miller EK, Cohen JD (2001) An integrative theory of prefrontal cortex function. *Annu Rev Neurosci* 24:167-202.
- Miller EK, Buschman TJ (2013) Cortical circuits for the control of attention. *Curr Opin Neurobiol* 23:216-222.
- Mitra A, Kraft A, Wright P, Acland B, Snyder AZ, Rosenthal Z, Czerniewski L, Bauer A, Snyder L, Culver J, Lee JM, Raichle ME (2018) Spontaneous Infra-slow Brain Activity Has Unique Spatiotemporal Dynamics and Laminar Structure. *Neuron* 98:297-305 e296.
- Mohajerani MH, McVea DA, Fingas M, Murphy TH (2010) Mirrored bilateral slow-wave cortical activity within local circuits revealed by fast bihemispheric voltage-sensitive dye imaging in anesthetized and awake mice. *J Neurosci* 30:3745-3751.
- Moritz CT, Perlmuter SI, Fetz EE (2008) Direct control of paralysed muscles by cortical neurons. *Nature* 456:639-642.
- Murayama Y, Biessmann F, Meinecke FC, Muller KR, Augath M, Oeltermann A, Logothetis NK (2010) Relationship between neural and hemodynamic signals during spontaneous activity studied with temporal kernel CCA. *Magnetic resonance imaging* 28:1095-1103.
- Ngai AC, Winn HR (2002) Pial arteriole dilation during somatosensory stimulation is not mediated by an increase in CSF metabolites. *Am J Physiol Heart Circ Physiol* 282:H902-907.
- Niell CM, Stryker MP (2010) Modulation of visual responses by behavioral state in mouse visual cortex. *Neuron* 65:472-479.
- Nir Y, Staba RJ, Andrillon T, Vyazovskiy VV, Cirelli C, Fried I, Tononi G (2011) Regional slow waves and spindles in human sleep. *Neuron* 70:153-169.
- Nir Y, Mukamel R, Dinstein I, Privman E, Harel M, Fisch L, Gelbard-Sagiv H, Kipervasser S, Andelman F, Neufeld MY, Kramer U, Arieli A, Fried I, Malach R (2008) Interhemispheric

- correlations of slow spontaneous neuronal fluctuations revealed in human sensory cortex. *Nat Neurosci* 11:1100-1108.
- Ogawa S, Menon RS, Tank DW, Kim SG, Merkle H, Ellermann JM, Ugurbil K (1993) Functional brain mapping by blood oxygenation level-dependent contrast magnetic resonance imaging. A comparison of signal characteristics with a biophysical model. *Biophys J* 64:803-812.
- Orbach HS, Cohen LB, Grinvald A (1985) Optical mapping of electrical activity in rat somatosensory and visual cortex. *J Neurosci* 5:1886-1895.
- Pagliardini S, Funk GD, Dickson CT (2013) Breathing and brain state: urethane anesthesia as a model for natural sleep. *Respir Physiol Neurobiol* 188:324-332.
- Pan WJ, Thompson G, Magnuson M, Majeed W, Jaeger D, Keilholz S (2011) Broadband local field potentials correlate with spontaneous fluctuations in functional magnetic resonance imaging signals in the rat somatosensory cortex under isoflurane anesthesia. *Brain Connect* 1:119-131.
- Petersen CC, Hahn TT, Mehta M, Grinvald A, Sakmann B (2003) Interaction of sensory responses with spontaneous depolarization in layer 2/3 barrel cortex. *Proc Natl Acad Sci U S A* 100:13638-13643.
- Pisauro MA, Benucci A, Carandini M (2016) Local and global contributions to hemodynamic activity in mouse cortex. *Journal of neurophysiology:jn* 00125 02016.
- Raichle ME (1998) Behind the scenes of functional brain imaging: a historical and physiological perspective. *Proc Natl Acad Sci U S A* 95:765-772.
- Raichle ME, Martin WR, Herscovitch P, Mintun MA, Markham J (1983) Brain blood flow measured with intravenous H₂(15)O. II. Implementation and validation. *J Nucl Med* 24:790-798.
- Raichle ME, MacLeod AM, Snyder AZ, Powers WJ, Gusnard DA, Shulman GL (2001) A default mode of brain function. *Proc Natl Acad Sci U S A* 98:676-682.
- Reivich M, Kuhl D, Wolf A, Greenberg J, Phelps M, Ido T, Casella V, Fowler J, Hoffman E, Alavi A, Som P, Sokoloff L (1979) The [18F]fluorodeoxyglucose method for the measurement of local cerebral glucose utilization in man. *Circ Res* 44:127-137.
- Rosazza C, Minati L, Ghielmetti F, Mandelli ML, Bruzzone MG (2012) Functional connectivity during resting-state functional MR imaging: study of the correspondence between independent component analysis and region-of-interest-based methods. *AJNR Am J Neuroradiol* 33:180-187.
- Ruiz-Mejias M, Ciria-Suarez L, Mattia M, Sanchez-Vives MV (2011) Slow and fast rhythms generated in the cerebral cortex of the anesthetized mouse. *Journal of neurophysiology* 106:2910-2921.
- Saleem AB, Ayaz A, Jeffery KJ, Harris KD, Carandini M (2013) Integration of visual motion and locomotion in mouse visual cortex. *Nat Neurosci* 16:1864-1869.
- Salzwedel AP, Grewen KM, Vachet C, Gerig G, Lin W, Gao W (2015) Prenatal drug exposure affects neonatal brain functional connectivity. *J Neurosci* 35:5860-5869.

- Scholvinck ML, Maier A, Ye FQ, Duyn JH, Leopold DA (2010) Neural basis of global resting-state fMRI activity. *Proc Natl Acad Sci U S A* 107:10238-10243.
- Sheroziya M, Timofeev I (2014) Global intracellular slow-wave dynamics of the thalamocortical system. *J Neurosci* 34:8875-8893.
- Shibuki K, Hishida R, Murakami H, Kudoh M, Kawaguchi T, Watanabe M, Watanabe S, Kouuchi T, Tanaka R (2003) Dynamic imaging of somatosensory cortical activity in the rat visualized by flavoprotein autofluorescence. *The Journal of physiology* 549:919-927.
- Shmuel A, Leopold DA (2008) Neuronal correlates of spontaneous fluctuations in fMRI signals in monkey visual cortex: Implications for functional connectivity at rest. *Hum Brain Mapp* 29:751-761.
- Shoham D, Glaser DE, Arieli A, Kenet T, Wijnbergen C, Toledo Y, Hildesheim R, Grinvald A (1999) Imaging cortical dynamics at high spatial and temporal resolution with novel blue voltage-sensitive dyes. *Neuron* 24:791-802.
- Siegel M, Buschman TJ, Miller EK (2015) Cortical information flow during flexible sensorimotor decisions. *Science* 348:1352-1355.
- Simpson JR, Jr., Snyder AZ, Gusnard DA, Raichle ME (2001) Emotion-induced changes in human medial prefrontal cortex: I. During cognitive task performance. *Proc Natl Acad Sci U S A* 98:683-687.
- Sirotin YB, Das A (2009) Anticipatory haemodynamic signals in sensory cortex not predicted by local neuronal activity. *Nature* 457:475-479.
- Smyser CD, Neil JJ (2015) Use of resting-state functional MRI to study brain development and injury in neonates. *Seminars in perinatology* 39:130-140.
- Spira ME, Hai A (2013) Multi-electrode array technologies for neuroscience and cardiology. *Nat Nanotechnol* 8:83-94.
- St-Pierre F, Marshall JD, Yang Y, Gong Y, Schnitzer MJ, Lin MZ (2014) High-fidelity optical reporting of neuronal electrical activity with an ultrafast fluorescent voltage sensor. *Nat Neurosci* 17:884-889.
- Stroh A, Adelsberger H, Groh A, Ruhlmann C, Fischer S, Schierloh A, Deisseroth K, Konnerth A (2013) Making waves: initiation and propagation of corticothalamic Ca²⁺ waves in vivo. *Neuron* 77:1136-1150.
- Sun R, Bouchard MB, Hillman EMC (2010) SPLASSH: Open source software for camera-based high-speed, multispectral in-vivo optical image acquisition. *Biomed Opt Expr* 1:385-397.
- Takata N, Nagai T, Ozawa K, Oe Y, Mikoshiba K, Hirase H (2013) Cerebral blood flow modulation by Basal forebrain or whisker stimulation can occur independently of large cytosolic Ca²⁺ signaling in astrocytes. *PloS one* 8:e66525.
- Tatum WO (2014) Ellen R. Grass Lecture: extraordinary EEG. *Neurodiagn J* 54:3-21.
- Tian L, Hires SA, Mao T, Huber D, Chiappe ME, Chalasani SH, Petreanu L, Akerboom J, McKinney SA, Schreier ER, Bargmann CI, Jayaraman V, Svoboda K, Looger LL (2009) Imaging neural activity in worms, flies and mice with improved GCaMP calcium indicators. *Nat Methods* 6:875-881.

- Tomasi D, Volkow ND (2012) Resting functional connectivity of language networks: characterization and reproducibility. *Mol Psychiatry* 17:841-854.
- Townsend RG, Solomon SS, Chen SC, Pietersen AN, Martin PR, Solomon SG, Gong P (2015) Emergence of complex wave patterns in primate cerebral cortex. *J Neurosci* 35:4657-4662.
- Tyszka JM, Kennedy DP, Adolphs R, Paul LK (2011) Intact bilateral resting-state networks in the absence of the corpus callosum. *J Neurosci* 31:15154-15162.
- Uhlirova H et al. (2016) Cell type specificity of neurovascular coupling in cerebral cortex. *Elife* 5.
- van der Veldt AA, Smit EF, Lammertsma AA (2013) Positron Emission Tomography as a Method for Measuring Drug Delivery to Tumors in vivo: The Example of [(11)C]docetaxel. *Front Oncol* 3:208.
- Vanni MP, Murphy TH (2014) Mesoscale transcranial spontaneous activity mapping in GCaMP3 transgenic mice reveals extensive reciprocal connections between areas of somatomotor cortex. *J Neurosci* 34:15931-15946.
- Vanzetta I, Hildesheim R, Grinvald A (2005) Compartment-resolved imaging of activity-dependent dynamics of cortical blood volume and oximetry. *J Neurosci* 25:2233-2244.
- Vincent JL, Patel GH, Fox MD, Snyder AZ, Baker JT, Van Essen DC, Zempel JM, Snyder LH, Corbetta M, Raichle ME (2007) Intrinsic functional architecture in the anaesthetized monkey brain. *Nature* 447:83-86.
- Vyazovskiy VV, Harris KD (2013) Sleep and the single neuron: the role of global slow oscillations in individual cell rest. *Nat Rev Neurosci* 14:443-451.
- Wekselblatt JB, Flister ED, Piscopo DM, Niell CM (2016) Large-scale imaging of cortical dynamics during sensory perception and behavior. *Journal of neurophysiology* 115:2852-2866.
- White BR, Bauer AQ, Snyder AZ, Schlaggar BL, Lee JM, Culver JP (2011) Imaging of functional connectivity in the mouse brain. *PloS one* 6:e16322.
- Xu HP, Burbridge TJ, Chen MG, Ge X, Zhang Y, Zhou ZJ, Crair MC (2015) Spatial pattern of spontaneous retinal waves instructs retinotopic map refinement more than activity frequency. *Developmental neurobiology* 75:621-640.
- Yesilyurt B, Ugurbil K, Uludag K (2008) Dynamics and nonlinearities of the BOLD response at very short stimulus durations. *Magnetic resonance imaging* 26:853-862.
- Zhou F, Liu J, Yu Y, Tian X, Liu H, Hao Y, Zhang S, Chen W, Dai J, Zheng X (2010) Field-programmable gate array implementation of a probabilistic neural network for motor cortical decoding in rats. *J Neurosci Methods* 185:299-306.
- Zhou Y, Liang M, Tian L, Wang K, Hao Y, Liu H, Liu Z, Jiang T (2007) Functional disintegration in paranoid schizophrenia using resting-state fMRI. *Schizophrenia research* 97:194-205.

Appendix: Publications and presentations related to this thesis

Peer reviewed publications

Ma Y, Shaik MA, Kozberg MG, Kim SH, Portes JP, Timerman D, Hillman EM. “Resting-state hemodynamics are spatiotemporally coupled to synchronized and symmetric neural activity in excitatory neurons.” *Proc Natl Acad Sci USA* 113:E8463-E8471.

Ma Y, Shaik MA, Kim SH, Kozberg MG, Thibodeaux DN, Zhao HT, Yu H, Hillman EM. “Wide-field optical mapping of neural activity and brain haemodynamics: considerations and novel approaches.” *Philos Trans R Soc Lond B Biol Sci* 371.

Kozberg, MG, **Ma Y**, Shaik MA, Kim SH and Hillman EM(2016). "Rapid Postnatal Expansion of Neural Networks Occurs in an Environment of Altered Neurovascular and Neurometabolic Coupling." *J Neurosci* 36(25): 6704-6717.

Manuscripts in preparation

Shaik MA, **Ma Y**, Ported J, Kim SH, Thibodeaux DN, Voleti V, Kozbeg M, Hillman EM. Selective perturbation of neurovascular coupling reveals dual endothelial mechanisms. Pending Submission.

Dynamic poster

The neural basis of resting state functional connectivity mapping resolved using simultaneous hemodynamic and wide-field GCaMP imaging

Y. Ma, S. H. Kim, M. A. Shaik, E. M. Hillman
Society for Neuroscience Annual Meeting
Chicago, Nov. 2015

Conference presentations

Spatiotemporal modeling of resting state neuronal activity in the awake mouse brain

S. H. Kim, M. A. Shaik, **Y. Ma**, H. T. Zhao, D. N. Thibodeaux, M. Khabbazian, T. Zheng, E. M. Hillman
Society for Neuroscience Annual Meeting
Washington D.C., Nov. 2017

Hemodynamic and neural resting state functional connectivity mapping in the awake mouse brain
S. Kim, M.A. Shaik, **Y. Ma**, H.T. Zhao, M.G. Kozberg, V. Voleti, E.M.C. Hillman
Brain Conference of the International Society for Cerebral Blood Flow and Metabolism
Washington D.C., Jun. 2017

Wide-field optical mapping of neural activity in awake mice and the importance of hemodynamic correction
Y. Ma, D. N. Thibodeaux, M. A. Shaik, S. H. Kim, E. M. Hillman
Optics and the Brain by Optical Society of America
San Diego, Apr. 2017

Investigating the effect of nonselective COX-inhibition on neuronal and vascular dynamics in the awake mouse cortex
M. A. Shaik, S. H. Kim, **Y. Ma**, E. M. Hillman
Gordon Research Conference – Glial Biology: Functional Interactions Among Glia and Neurons
Ventura, Mar. 2017

Wide-field optical mapping of neural activity and cortical hemodynamics imaging during locomotion
Y. Ma, S. H. Kim, M. A. Shaik, H. T. Zhao, E. M. Hillman
Society for Neuroscience Annual Meeting
San Diego, Nov. 2016

Comparing stimulus-evoked and resting-state neurovascular coupling with simultaneous electrophysiology, wide-field neural GCaMP and hemodynamic imaging
Y. Ma, M. G. Kozberg, S. H. Kim, E. M. Hillman
XXVIIth International Symposium on Cerebral Blood Flow, Metabolism and Function and XIIth International Conference on Quantification of Brain Function with PET
Vancouver, June 2015

Postnatal development of neurovascular coupling
M. G. Kozberg, **Y. Ma**, M. A. Shaik, S. H. Kim, E. M. Hillman
XXVIIth International Symposium on Cerebral Blood Flow, Metabolism and Function and XIIth International Conference on Quantification of Brain Function with PET
Vancouver, June 2015

Hemodynamic and neuronal resting state functional connectivity mapping in the awake mouse brain
S. H. Kim, M. A. Shaik, **Y. Ma**, H. T. Zhao, M. G. Kozberg, V. Voleti, E. M. Hillman
XXVIIth International Symposium on Cerebral Blood Flow, Metabolism and Function and XIIth International Conference on Quantification of Brain Function with PET
Vancouver, June 2015

Assessing cortical neurovascular coupling in the presence and absence of stimulation
Y. Ma, M. G. Kozberg, S. H. Kim, E. M. Hillman

Society for Neuroscience Annual Meeting
Washington D.C., Nov. 2014

Mechanisms of neurovascular maturation in the developing brain
M. G. Kozberg, Y. Ma, M. A. Shaik, C. A. Lunardi, A. J. Gomes, E. Tfouni, E. M. Hillman
Society for Neuroscience Annual Meeting
Washington D.C., Nov. 2014

Comparison of neuronal and hemodynamic resting state functional connectivity mapping in awake mouse brain
S. H. Kim, **Y. Ma**, M. A. Shaik, M. G. Kozberg, V. Voleti, K. Yang, E. M. Hillman
Society for Neuroscience Annual Meeting
Washington D.C., Nov. 2014

Are resting state and stimulus-evoked neurovascular coupling different?
Y. Ma, A. Rayshubskiy, S. H. Kim, D. Timereman, M. G. Kozberg, E. M. Hillman
Society for Neuroscience Annual Meeting
San Diego, Nov. 2013

Longitudinal assessment of resting state functional connectivity variance in the rat brain
S. H. Kim, V. Voleti, **Y. Ma**, E. Ramires, M. G. Kozberg, M. B. Bouchard, B. R. Chen, A. Rayshubskiy, E.M. Hillman
Society for Neuroscience Annual Meeting
San Diego, Nov. 2013